Sediment transport in the Firth of Thames mangrove forest, New Zealand

A thesis submitted in partial fulfilment

of the requirements for the degree

of

Masters of Science

In Earth Sciences

at

The University of Waikato

by

Nicola Jane Lovett

THE UNIVERSITY OF
WAIKATO
Te Whare Wānanga o Waikato

2017

Abstract

Mangroves provide a unique habitat for many species. In addition to being biologically significant ecosystems, mangroves help protect coastal areas through the dissipation of tidal currents and wave energy. However, mangroves are unpopular with some communities in New Zealand and removal of them is often considered in management strategies. In order to effectively manage these vegetated coastal areas and predict growth and/or decline of mangrove systems, it is necessary to have a detailed understanding of how the hydrodynamic processes within forests influence sediment transport and deposition.

A 6-day long experiment was conducted in the Firth of Thames mangrove forest to examine hydrodynamic processes that influence sediment transport from the intertidal mudflat across the fringing region of the mangrove forest into the forest itself. A unique deployment system was utilised to minimise environmental disturbance during the data collection process at 5 sites. Site 1 was located on the mudflat and site 2 was in the fringe area (i.e. the boundary between flat and forest). Sites 3 to 5 were located at increasing distances inside the forest. Results indicate wave activity causes a net offshore flux of sediment at site 1 (approximately 850 kg/m over the duration of the experiment), contrary to expectations. However, at all other sites, there was a net onshore flux of sediment from the fringe into the forest (maximum at site 4 of 113.3 kg/m). Minimal scour in the experiment area indicates that sediment is primarily supplied by advection from other regions of the system.

Flocculation is a key process in cohesive sediment transport. One of the aims of the study was to understand the controls on flocculation within this vegetated system. Despite difficulties inherent in measuring flocs, floc images were successfully collected from some sites. An initial qualitative analysis performed on images from 2 sites (1 and 3) over 2 tides revealed a greater quantity of large flocs on the mudflat than in the forest and that in general, flocs were larger on the ebb tide. These results imply that settling velocities on the mudflat are larger than within the forest and settling velocities are larger during ebb than flood tides.

Acknowledgements

First and foremost, I would like to thank my supervisors, Dr Julia Mullarney (University of Waikato) and Dr Iain MacDonald (NIWA), for all their invaluable help and guidance, both were very patient and generous with their time and I could not have asked for better supervisors.

I am also very grateful to the following organisations for much appreciated funding for my research: American Chemical Society, Department of Conservation, University of Waikato, Waikato Regional Council. I received two memorial scholarships for my master's research; Dr Stella Frances Memorial Scholarship and Tess Embling Memorial Scholarship for which, I am very grateful. I would also like to thank NIWA for allowing me to have Iain as a supervisor and for the use of equipment and instruments.

A big thank you to Dr Erik Horstman for providing elevation data and providing invaluable help, particularly during the calibration stage of the laboratory work.

The Firth of Thames is a particularly challenging environment in which to work, so I would like to say a big thank you to the following people who helped in the field: Julia and Iain, Matt Davies, Bérengère Dejeans, Chris Eager, Dr Erik Horstman, Ben Norris, Warwick Powrie, Dean Sandwell and the NIWA boat drivers.

The following people were invaluable to my ability to carry out laboratory work, so thank you to: Dr Erik Horstman, Lee Laboyrie, Annette Rodgers, Janine Ryburn and Dean Sandwell.

A big thank you to Cheryl Ward for being such an awesome Librarian! I am very grateful for your help.

I would also like to thank my friends in the Coastal Marine Group and those from the Intercoast programme for all their encouragement and kindness. Last but not least, I would like to thank Noel Bates, Bérengère Dejeans, James McHardy and Jonno Rau for their unending support!

Table of contents

Abstract i
Acknowledgements ii
Table of contents iii
List of figures v
List of tables x
Chapter 1: Introduction 1
1.1 Background 1
1.2 Hydrodynamics in vegetated regions 2
1.3 Sediment transport 4
1.4 Knowledge gaps and study aims 6
1.4.1 The study site: background 7
1.4.2 Hypotheses 8
1.4.3 Thesis layout 8
Chapter 2: Field and laboratory measurements 9
2.1 Introduction 9
2.2 Study site 9
2.3 Experimental design and measurements 11
2.4 Data quality control and processing 14
2.4.1 OBS calibration 15
2.4.2 Wave statistic calculations 17
2.4.3 Sediment flux calculations 17
Chapter 3: Results 19
3.1 Introduction 19
3.2 Environmental conditions 19
3.3 Waves 22
3.4 Current velocities 26
3.4.1 Hydrodynamics during calm periods 26
3.4.2 Hydrodynamics during windy periods 26
3.5 Suspended Sediment Concentration 37
3.5.1 SSC during calm periods 40
3.5.2 SSC during windy periods 43
3.6 Bed sediment grain size 46
3.7 Sediment transport 46

3.8 Flocculation 59
3.9 Summary 63
Chapter 4: Discussion 66
4.1 Summary of findings 76
4.2 Further work 78
References 79
Appendix: SSC plotted against other variable 84

List of figures

Figure 1.1: Velocity profiles for two depth ratios, *H/h* where *H* is water depth and *h* is canopy height, and dP/dx is the pressure gradient which is comparable to the turbulent stresses in figure b whereas in a, dP/dx is smaller than the turbulent stresses. From Nepf and Vivoni (2000)... 3

Figure 1.2: Mangrove coverage in the Firth of Thames, showing multiple seedling recruitment events. From Swales *et al.* (2007). 8

Figure 2.1: Field site location. a) New Zealand with the Firth of Thames highlighted in red, b) The Firth of Thames with the field site and weather station locations. 10

Figure 2.2: Elevation profiles of the Firth of Thames field site, showing distance from the mudflat in the forest along the x-axis and elevation (m+MSL) on the y-axis. a) is the topography of the entire mangrove forest, b) shows the elevation profile of the 5 measurements site. Data provided by Dr Erik Horstman (University of Waikato)..... 10

Figure 2.3: Google Earth Image from 20/01/2017 showing sites 1 to 5. Arrows indicate components of velocity discussed in the text, with E-W representing the u-velocities and N-S, the y-velocities. South and west are negative and north and east are positive. 11

Figure 2.4: a) Cantilevered bridge extended from the boardwalk with frame and attached instruments being set-up at site 1 on the intertidal mudflat, b) Programming floc cameras at site 1, without disturbing the sediment. 13

Figure 2.5: Frame with attached equipment: a) front view (site 3), note minimal disturbance by footprint of the frame b) side view (site 2). 14

Figure 2.6: Tank and set-up used to calibrate OBS sensors..... 16

Figure 2.7: Example calibration result from a Campbell Scientific OBS3+ sensor (site 4, sensor attached to Nortek Vector ADV). 16

Figure 3.1: Wind rose created using hourly wind data from a NIWA weather station at Firth of Thames (-37.21522, 175.4503) a) during the experimental period, 12/12/2016-19/12/2016, b) over the period: 10/11/2010-27/07/2017. Colours indicate wind speeds, bars indicate direction from and the length of the bars indicates the frequency of occurrence of the wind conditions. 20

Figure 3.2: Measured conditions at the Firth of Thames study site (12th December 2016 – 19th December 2016). (a) water depths, (b) wind speeds, (c) wind directions (direction from), (d) temperature and (e) salinities. Numbers above refer to tide number, referenced in the text. Red numbers = no wave conditions, black numbers = wave conditions. 21

Figure 3.3: Hourly rainfall (mm) from NIWA weather station at Firth of Thames Ews (-37.21522, 175.4503), 10/11/2010-27/07/2017. 22

Figure 3.4: Wave statistics from all sites shown with wind conditions (b, c), (a) water depth *h* (m), (d) significant wave height *Hs* (m), (e) significant orbital velocity at the bed, U_{sigbed} (m/s) and (f) mean wave period T_m (s). Numbers above refer to tide number, referenced in the text. Red numbers = no wave conditions, black numbers = wave conditions. 24

Figure 3.5: Example pressure data from tide 6 (15th December) from site 1. a) shows a short 2-min time series of pressure data. b) is the corresponding wave power spectral density from the full 10-min burst. The grey shading are the 95 % confidence intervals and the spectrum has 32 degrees of freedom. 25

Figure 3.6: Water depths (a) and velocities (m/s) at site 1, Firth of Thames, b) u (E/W) c) v (N/S) d) w-direction (vertical). Numbers above refer to tide number, referenced in the text. Red numbers = no wave conditions, black numbers = wave conditions. 29

Figure 3.7: Water depths (a) and velocities (m/s) at site 2, Firth of Thames, b) u (E/W) c) v (N/S) d) w-direction (vertical). Numbers above refer to tide number, referenced in the text. Red numbers = no wave conditions, black numbers = wave conditions. 30

Figure 3.8: Water depths (a) and velocities (m/s) at site 3, Firth of Thames, b) u (E/W) c) v (N/S) d) w-direction (vertical). Numbers above refer to tide number, referenced in the text. Red numbers = no wave conditions, black numbers = wave conditions. 31

Figure 3.9: Water depths (a) and velocities (m/s) at site 4, Firth of Thames, b) u (E/W) c) v (N/S) d) w-direction (vertical). Numbers above refer to tide number, referenced in the text. Red numbers = no wave conditions, black numbers = wave conditions. 32

Figure 3.10: Water depths (a) and velocities (m/s) at site 5, Firth of Thames, b) u (E/W) c) v (N/S) d) w-direction (vertical). Numbers above refer to tide number, referenced in the text. Red numbers = no wave conditions, black numbers = wave conditions. 33

Figure 3.11: Burst-averaged N/S velocities from downward-facing Aquadopps at the point nearest the height above the bed of the Vectors (averaged over profile length, red lines) and Vectors (single point measurements, black lines) velocities (m/s) for sites 1 to 5 (a to e, respectively). Numbers above refer to tide number, referenced in the text. Red numbers = no wave conditions, black numbers = wave conditions. 34

Figure 3.12: Tidal stage graphs showing N/S component of velocities at site 1 for a) tide 4 (waves) and b) tide 10 (no waves). Negative values correspond to flood dominant (southward) velocities and positive values correspond to (northward) or ebb dominant velocities. 35

Figure 3.13: Water depths (a) and horizontal flow velocities (m/s) for sites 1 to 5 (b to f, respectively). Note different axes values. Numbers above refer to tide number, referenced in the text. Red numbers = no wave conditions, black numbers = wave conditions. 36

Figure 3.14. (a) Water depths and SSC (mg/l) from all sites (b-f correspond to sites 1 -5). In b-f, near-bed SSC are shown in black, and SSCs higher up in the water column are shown in red. Heights of measurements are given in Table 3.3. Numbers above refer to tide number, referenced in the text. Red numbers = no wave conditions, black numbers = wave conditions. 39

Figure 3.15: SSC (~30 cm above the bed) over days with less wave energy (*Hs* = 0.0445 m at site 1 for tides 2 and 9-11). Lines are coloured by the significant orbital velocities at the bed..... 40

Figure 3.16: SSC (~30 cm above the bed) over days with less wave energy (*Hs* = 0.0243 m at site 2 for tides 2 and 9-11). Lines are coloured by the significant orbital velocities at the bed..... 41

Figure 3.17: SSC (~30 cm above the bed) over days with less wave energy (*Hs* = 0.0226 m at site 3 for tides 2 and 9-11). Lines are coloured by the significant orbital velocities at the bed..... 41

Figure 3.18: SSC (~30 cm above the bed) over days with less wave energy (*Hs* = 0.0159 m at site 4 for tides 2 and 9-11). Lines are coloured by the significant orbital velocities at the bed..... 42

Figure 3.19: SSC (~30 cm above the bed) over days with less wave energy (*Hs* = 0.0079 m at site 5 for tides 2 and 9-11). Lines are coloured by the significant orbital velocities at the bed..... 42

Figure 3.20: SSC (~30 cm above the bed) over days with greater wave energy (mean *Hs* = 0.1139 m at site 1 for tides 1 and 3-8 and 12). Lines are coloured by the significant orbital velocities at the bed..... 43

Figure 3.21: SSC (~30 cm above the bed) over days with greater wave energy (*Hs* = 0.0720 m at site 2 for tides 1 and 3-8 and 12). Lines are coloured by the significant orbital velocities at the bed..... 44

Figure 3.22: SSC (~30 cm above the bed) over days with greater wave energy (*Hs* = 0.0549 m at site 3 for tides 1 and 3-8 and 12). Lines are coloured by the significant orbital velocities at the bed..... 44

Figure 3.23: SSC (~30 cm above the bed) over days with greater wave energy (*Hs* = 0.0320 m at site 4 for tides 1 and 3-8 and 12). Lines are coloured by the significant orbital velocities at the bed..... 45

Figure 3.24: SSC (~30 cm above the bed) over days with greater wave energy (*Hs* = 0.0150 m at site 5 for tides 1 and 3-8 and 12). Lines are coloured by the significant orbital velocities at the bed..... 45

Figure 3.25: d50 (μm) of bed-sediment grain size at each measurement site in the Firth of Thames, a) sub-sample 1, b) sub-sample 2 46

Figure 3.26: Burst-averaged profiles of (a) v velocity, (b) SSC and (c) *v*C* profiles for site 1. Data was taken from mid-flood tide during tide 4 which was characterised by northerly-directed v velocities throughout the tidal cycle. Colours indicate the four models used to fit the SSC data. SSC measurement heights were 0.27 m and 0.03 m (and are shown by the intersection of the four model fits in panel b).. 48

Figure 3.27: Burst-averaged profiles of (a) v velocity, (b) SSC and (c) *v*C* for site 1. Data was taken from mid-ebb tide during tide 4 which was characterised by northerly-directed v velocities throughout the tidal cycle. Colours indicate the four models used to fit the SSC data. SSC measurement heights were 0.27m and 0.03 m (and are shown by the intersection of the four model fits in panel b). 49

Figure 3.28: Burst-averaged profiles of (a) v velocity, (b) SSC and (c) *v*C* profiles for site 1. Data was taken from mid-flood tide during tide 10 which was characterised by northerly-directed v velocities throughout the tidal cycle. Colours indicate the four models used to fit the SSC data. SSC measurement heights were 0.27 m and 0.03 m (and are shown by the intersection of the four model fits in panel b).. 50

Figure 3.29: Burst-averaged profiles of (a) v velocity, (b) SSC and (c) *v*C* profiles for site 1. Data was taken from mid-ebb tide during tide 10 which was characterised by northerly-directed v velocities throughout the tidal cycle. Colours indicate the four models used to fit the SSC data. SSC measurement heights were 0.27 m and 0.03 m (and are shown by the intersection of the four model fits in panel b).. 51

Figure 3.30: *v*C* profiles for all sites at selected times during two different tides: tide 4 characterised by larger wave energy and tide 10 characterised by smaller wave energy. a) Mid-flood of tide 4, b) mid-ebb of tide 4, c) mid-flood of tide 10, d) mid-ebb of tide 10..... 53

Figure 3.31: Time series of (a) water depths, (b) N-S velocities and (c) sediment fluxes ($kg/m^2/s$) at site 1. Dashed lines show 0 values. Numbers above refer to tide number, referenced in the text. Red numbers = no wave conditions, black numbers = wave conditions..... 54

Figure 3.32: Time series of (a) water depths, (b) N-S velocities and (c) sediment fluxes ($kg/m^2/s$) at site 2. Dashed lines show 0 values. Numbers above refer to tide number, referenced in the text. Red numbers = no wave conditions, black numbers = wave conditions..... 55

Figure 3.33: Time series of (a) water depths, (b) N-S velocities and (c) sediment fluxes ($kg/m^2/s$) at site 3. Dashed lines show 0 values. Numbers above refer to tide number, referenced in the text. Red numbers = no wave conditions, black numbers = wave conditions..... 56

Figure 3.34: Time series of (a) water depths, (b) N-S velocities and (c) sediment fluxes ($kg/m^2/s$) at site 4. Dashed lines show 0 values. Numbers above refer to tide number, referenced in the text. Red numbers = no wave conditions, black numbers = wave conditions..... 57

Figure 3.35: Time series of (a) water depths, (b) N-S velocities and (c) sediment fluxes (kg/m^2/s) at site 5. Dashed lines show 0 values. Numbers above refer to tide number, referenced in the text. Red numbers = no wave conditions, black numbers = wave conditions..... 58

Figure 3.36: Example of qualitative size classes for analysing flocs, based on a visual analysis of two tides (9 and 11) at two different sites (1 and 3). Large = ~350 µm, medium = ~150 µm and small = ~20 µm..... 60

Figure 3.37: Floc analysis using qualitative analysis for tide 9. a) water depths at sites 1 (blue) and 3 (green), b) bar graph showing the number of flocs of each size in each burst at site 1, c) shows the same data for site 3. Y-axis categories correspond to no flocs (0), few (1), some (2), many (3). See text for details..... 61

Figure 3.38: Floc analysis using qualitative analysis for tide 11. a) water depths at sites 1 (blue) and 3 (green), b) bar graph showing the number of flocs of each size in each burst at site 1, c) shows the same data for site 3. Y-axis categories correspond to no flocs (0), few (1), some (2), many (3). See text for details..... 62

Figure 3.39: Total sediment flux (kg/m^2) for each tide at all sites..... 64

Figure 3.40: Cumulative sediment fluxes (kg/m^2) over the experiment for all sites..... 65

Figure 4.1: The Firth of Thames situated in the Hauraki Gulf, New Zealand. From Google Maps (2017)..... 67

Figure 4.2: Model results for depth-averaged near steady state velocities from the Firth of Thames, New Zealand, for a north-west wind of 15 m/s. From Black *et al.* (2000). 68

Figure 4.3: Conceptual diagram showing sediment fluxes in and out of the mangrove forest. Arrows indicate sediment direction and the size of the arrow is indicative of the comparative amount of sediment moving in or out at each site, although arrows are not to scale. Potential areas of scour and deposition are labelled. Inset - Mudflat and mangrove elevation (m + MSL). Elevation profile data provided by Dr Erik Horstman (University of Waikato). 71

Figure 4.4: Photograph of runnels behind site 1, Firth of Thames, New Zealand 73

Figure 4.5: a) Scour around pneumatophores seaward of site 2 and b) Site 2 equipment deployment, showing scour around pneumatophores. 73

Figure 4.6: Site 3 instrument deployment, showing dense pneumatophores and no scour. Water in the photograph is in a runnel. Firth of Thames, New Zealand. 74

Figure 4.7: Advancement of the mangrove forest in the Firth of Thames, New Zealand from 2007-2017. Arrow indicates the same location and shows an advance in the forest area. The scale represents 100 m and north is upwards. From Horstman *et al.* (2017a). 75

List of tables

Table 2.1: Equipment details and variables measured at each site. SPB = Samples Per Burst, HAB = Height above the bed 12

Table 3.1: Maximum and mean wave statistics for each site..... 22

Table 3.2: Maximum horizontal flow velocities (m/s) for all sites over the period of the experiment 28

Table 3.3: Height above the bed of SSC measurements 37

Table 3.4: Maximum and mean SSC (mg/l) at sites 1-5 over the entire experimental duration..... 38

Chapter 1

Introduction

1.1 Background

Mangroves are halophytic trees or shrubs typically found in low energy coastal environments such as estuaries (Morrisey, 2007). Mangroves account for 75% of tropical and sub-tropical coastal forests, mainly existing between 25^{o} N and 25^{o} S (Yang *et al.*, 2013). New Zealand mangroves are at the southern-most limit of their growth at 38^{o} S (Yang *et al.*, 2013). These salt-tolerant trees are valuable ecosystems that supply numerous ecosystem services, such as providing a unique habitat for many species, including crabs, insects and reptiles, amphibians, birds and mammals, (Kathiresan & Bingham, 2001; Reef *et al.*, 2010). Moreover, these ecosystems also offer physical services by for example, the protection of coastal areas through the dissipation of tidal currents and wave energy (Furukawa *et al.*, 1997; Horstman *et al.*, 2014; Vo-Luong & Massel, 2008).

Mangroves have an aerial root system that enables respiration. One of the more common root types are pneumatophores (pencil roots), which, along with the trunks and the vegetation canopy, create the drag that attenuates currents and waves (Horstman *et al.*, 2017b). As a consequence of this removal of energy from the system, vegetation can often trap sediment within the mangrove system (Furukawa *et al.*, 1997; Wolanski, 1995). These processes enable the mangroves to advance when hydrodynamic conditions are suitable for seedling recruitment (Balke *et al.*, 2013). If sedimentation can keep pace with rising mean sea level, mangroves may help mitigate against future climatic changes (Alongi, 2008). The overarching aim of this thesis is to investigate how mangroves influence sediment transport.

New Zealand mangroves are monospecific, comprising *Avicennia marina subsp. Australasica (Morrisey, 2007).* Mangroves in New Zealand are expanding in contrast to the dominant global trend of a decline in mangrove coverage: at least 35% of the world's mangrove forests have been lost over the past two decades (Feller *et al.*, 2010). Expansion in New Zealand is thought to be because of land-use change, resulting in large inputs of terrestrial sediment and nutrients into the

waterways, and transportation to the coast, creating ideal conditions for mangroves to develop (Lovelock *et al.*, 2007; Stokes *et al.*, 2010). Despite their benefits, there is often a negative public perception of mangroves in New Zealand because they can alter habitats; decrease biodiversity and block views and waterways used for recreational activities (Harty, 2009).

Sediment input is a key stressor in New Zealand's estuaries because terrestrial sediments can affect the function of ecosystems through smothering of shellfish beds (Rodil *et al.*, 2011; Thrush *et al.*, 2004), altering the biogeochemistry of the seabed (Gilbert *et al.*, 2003; Tang & Kristensen, 2007), killing infauna (Woodin *et al.*, 2012) and reducing water clarity and subsequently phytoplankton productivity (Morrison *et al.*, 2009). However, mangroves are able to trap this sediment. In order to predict growth and/or decline of mangrove systems, it is necessary to have a detailed understanding of how the hydrodynamic processes within forests influence sediment transport and deposition. This thesis explores how hydrodynamic processes in the Firth of Thames mangrove swamp affect flocculation and sediment fluxes between the inter-tidal mud flat and the forest.

1.2 Hydrodynamics in vegetated regions

Flow in mangrove areas is mainly influenced by friction induced by the vegetation. Both mean and turbulent flows are altered by vegetation at different scales (from individual stems or blades to the canopy itself). Mean flow is reduced by the drag force from the plants and the presence of vegetation damps turbulence at canopy scales but induces turbulence at the stem scale (Nepf, 2012). Emergent canopies (Figure 1.1.a) occupy the entire water depth and vegetation protrudes above the water surface. In these cases, flow is driven by pressure gradients (Nepf & Vivoni, 2000). The shear layer is minimal in emergent systems and turbulence occurs in the wakes of individual roots, stems or trunks of the plants and is a function of canopy drag. The scales of eddies in vegetated areas where the plants are rigid, are dependent on the smallest stem diameter or the distance between the stems, whereas in unvegetated areas, the scale of eddies is dependent on water depth or larger-scale bathymetric features (Nepf, 2012). Relative to unvegetated areas, turbulent diffusivity is reduced because of the small length scale of the wake turbulence (Nepf & Vivoni, 2000). In general, within-canopy flow speeds decrease with vegetation

density. Turbulence initially increases with increasing canopy density; however, above a critical threshold of canopy density, turbulence decreases with increasing density. This change in turbulence is due to the opposing effects of reduction in flow speeds and the production of stem wake turbulence within the canopy. In submerged canopies (Figure 1.1b), processes depend on the depth of submergence in the water. If deeply submerged, within-canopy flow is dominated by the stress caused by turbulence at the top of the canopy. If shallowly submerged, flow is driven by both turbulent stress and potential gradients, shear is generated in the fluid layer above a submerged canopy and decays into the canopy itself (Nepf & Vivoni, 2000). Mangrove forests tend to be emergent but their associated pneumatophores can be submerged through periods of tidal inundation.

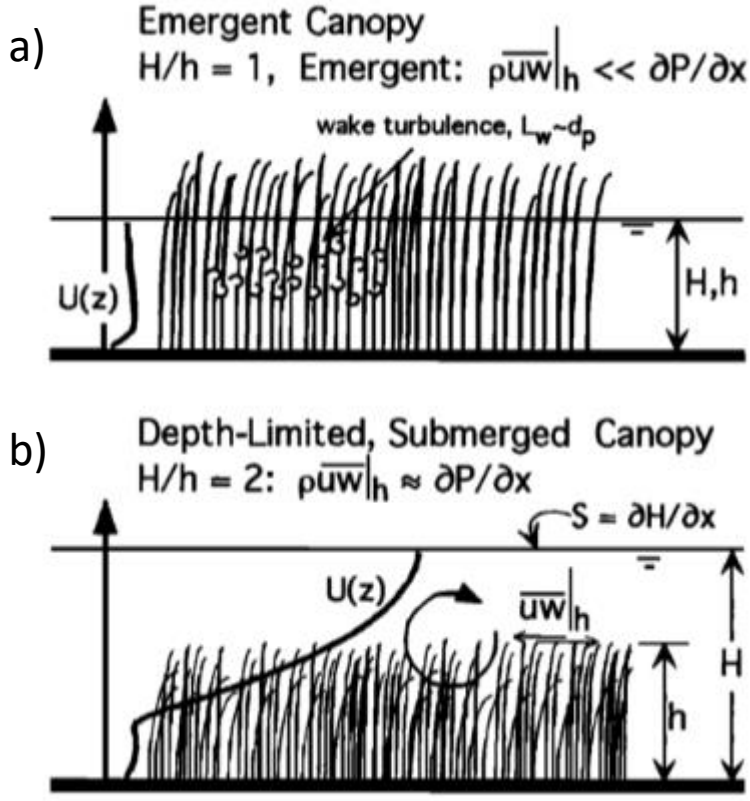

Figure 1.1: Velocity profiles for two depth ratios, *H/h* where *H* is water depth and *h* is canopy height, and dP/dx is the pressure gradient which is comparable to the turbulent stresses in figure b whereas in a, dP/dx is smaller than the turbulent stresses. From Nepf and Vivoni (2000).

Mangrove forests dissipate the energy of waves and currents. Significant mechanisms of wave attenuation are interactions of the tree trunks and roots with wave motion, and wave breaking (Vo-Luong & Massel, 2008). Vo-Luong and

Massel (2008) produced a numerical model validated against field data collected in Can Gio Mangrove Biosphere Reserve, South Vietnam. The model indicates that interaction between waves and vegetation is the primary means of attenuation in dense forests, whereas in sparse areas, wave breaking is more significant. The greater dissipation of energy is a result of wave-trunk interactions, which in denser forests, act to dampen wave height and therefore reduce wave breaking. The authors concluded that wave height and energy attenuate very quickly with distance from the mangrove front into the forest, as do mean vertical and horizontal velocities. A study across two transects of an estuary in the Southern Andaman region of Thailand by Horstman *et al.* (2014) found significant wave height decreased through the forest as a result of vegetation drag. However, the mean wave period increased slightly into the forest, which the authors attributed to longer period swell waves not losing much energy, whereas shorter period waves, are preferentially dissipated. Breaking waves were not often observed due to the wave heights being too small; however, shoaling was observed resulting in an increase in wave height. Conversely, a reduction in water depth enhances bottom friction effects, which reduces wave height. The rate at which attenuation occurs, depends primarily on the mangrove characteristics (for example, trunk diameter and type of root system), density of the forest, and the intertidal flat topography (Horstman *et al.*, 2014).

The direction of flow can change from the fringe to the mangrove forest. Horstman *et al.* (2013) showed that in sparsely vegetated areas such as the fringe area, flow direction and velocity are influenced by the prevailing flow outside of the vegetation. Whereas, in more densely vegetated areas at higher elevations (with respect to MSL), flows can become oriented perpendicular to the vegetation edge and flow speeds decrease significantly. Mullarney *et al.* (2017b) also observed this rotation of the flow in a study over two seasons in the Mekong Delta, Vietnam.

1.3 Sediment transport

Vegetation effects on flows will also have consequences for the transport and deposition of sediment. In vegetated regions a reduction in near-bed stresses in the zones of slow flow can result in sediment accumulating (Nepf & Vivoni, 2000). An investigation of sediment transport in the mangrove system of Middle Creek,

Cairns, Australia by Furukawa *et al.* (1997), supported the observation of Nepf and Vivoni (2000). In the field study at Middle Creek, measurements were taken across a transect from the creek through the forest to a salt marsh. Velocities, sediment accumulation and suspended sediment concentrations (hereafter, SSC) were all measured. A numerical model was also used to further analyse flows, including turbulence around the vegetation. Results indicated that approximately 80% of the sediment brought into the mangroves on a spring tide, remained trapped in the mangrove forest.

In general, mangroves facilitate a net transport of sediment into the forest system. Flood tides transport suspended sediment into the area and enhanced micro-scale turbulence around vegetation, maintains the sediment in suspension. Near slack tide, the suspended sediment starts to settle out and the ebb currents are too weak to re-suspend or transport the sediment back out into the estuary (Furukawa & Wolanski, 1996). There is therefore a build-up of sediment in the mangroves. An examination of trapping efficiency of two different mangrove forests in Palau, Micronesia was conducted by Victor *et al.* (2004). Mangroves covered a similar percentage of each catchment (about 3.8%), but one of the forests had a sparsely developed catchment with an input of sediment of 1.9 tons km^{-2} yr^{-1} whereas the other was highly developed with a sediment input of 150 tons km^{-2} yr^{-1}. It was found that both systems trapped a similar percentage of sediment, indicating that the sediment trapping efficiency is determined by changes in hydrodynamics rather than the SSC.

Observations of flows around different densities of vegetation illustrated that there are simple flows around trunks, which can produce large wakes when velocities are high enough. In high density root systems, there are complex flows, displaying eddies, jets and stagnation zones in which sediment can settle out. The reason that very fine particles are able to settle out of the water column so quickly (for example, Furukawa and Wolanski (1996) found settling occurred within 30 minutes) is that they flocculate (Furukawa & Wolanski, 1996).

Flocculation is a key process in cohesive sediment transport. Flocculation is a process whereby fine particles in suspension, aggregate to form a larger particle called a floc (Eisma, 1986). These flocs have a larger settling velocity than their

component particles, but a smaller settling velocity than an equivalent single particle (non-floc) of the same size. In general, the two main factors that control floc size are turbulence intensity and SSC (Dyer & Manning, 1999). However, there have been few studies examining flocculation within vegetated environments (Mullarney & Henderson, 2017a). One such study by Wolanski (1995) found that flocculation is strongly dependent upon the mangrove extent and characteristics, for example, a sparse mangrove site has a smaller effect on flocculation then a dense site. Secondary factors such as sediment composition also influence floc formation as silt produces weaker flocs that disaggregate easily, whereas clay particles form strong bonds. Wolanski (1995) also concluded that flocculation is significant, particularly the size of flocs because flocs have minimal light scattering effects and therefore effect primary production in areas of high flocculation and turbidity.

1.4 Knowledge gaps and study aims

Flow in vegetated areas such as seagrass beds and saltmarshes, has been well studied (Nepf, 2012; Nepf & Vivoni, 2000); however, the effects of flow on sediment transport in vegetated areas, are not so well understood. Many previous studies took a numerical modelling approach (Temmerman *et al.*, 2005; Wu *et al.*, 2001), or used vegetation analogues in a laboratory setting (Struve *et al.*, 2003). Although a number of field studies have taken place in mangroves, many of these were in systems incised by tidal creeks to determine exchange between the mangrove forest and the channel (Furukawa & Wolanski, 1996; Furukawa *et al.*, 1997; Mazda *et al.*, 1995). Horstman *et al.* (2015) suggest that more research is required in to how different environmental settings affect the routing of tidal flow and sediments through mangroves. The present study is focussed on a flat-fronted mangrove forest without large creeks (although small drainage channels exist). The aim of the study is to determine the dominant hydrodynamic processes controlling sediment transport in mangrove forests of this type. Specifically, the aim is to quantify changes in sediment fluxes in the different environments (mudflat, mangrove fringe and inside the forest) and with distance into the forest. To achieve the aim of this study we conducted a process-based field experiment in the mangrove forest located at the southern end of the Firth of Thames, New Zealand.

1.4.1 The study site: background

The mangrove forest located at the southern end of the Firth of Thames is approximately 11 km^2 and has colonised the intertidal flats since the 1950s. Early aerial photography from the mid-1940s shows that mangrove trees were only located in the delta deposits at the river mouths. From the 1950s, the mangrove forest developed in 'waves' as a result of 4 or 5 recruitment events (Figure 1.2). These events are likely to coincide with prolonged calm weather, as high rates of seedling mortality occur during periods of wave-driven erosion (Swales *et al.*, 2007). Sediment load into the Firth was substantially increased when land clearance began occurring in the mid-1800s with the beginnings of the timber-felling and gold mining industries in the area. It has been further exacerbated by extensive conversion of land to pastoral farming in the Hauraki Plains (Swales *et al.*, 2007). At present, the Piako and Waihou Rivers input approximately 190,000 t yr^{-1} of suspended sediment into the system (Swales *et al.*, 2015). The estuary is approximately 800 km^2, mesotidal, and experiences semi-diurnal tides with an average tide range of between 2.2 - 2.9 m (Swales *et al.*, 2015). The Firth shoals from 35 m deep at the northern inlet towards the south. Tidal currents on the intertidal flats are typically < 0.2 m s^{-1} but regional wind patterns can generate faster currents (Swales *et al.*, 2007). The prevailing southern and westerly winds produce an anti-clockwise large-scale circulation, whereas a clockwise residual rotation of currents is caused by northerly to easterly winds. In the central Firth (approximately 9.7 m deep), mean significant wave height (H_{sig}) is 0.41 m and the maximum average wave period (T_m) is 8.6 s (Swales *et al.*, 2007). The predominant directions of wave energy are from the NNW and the N (Swales *et al.*, 2007).

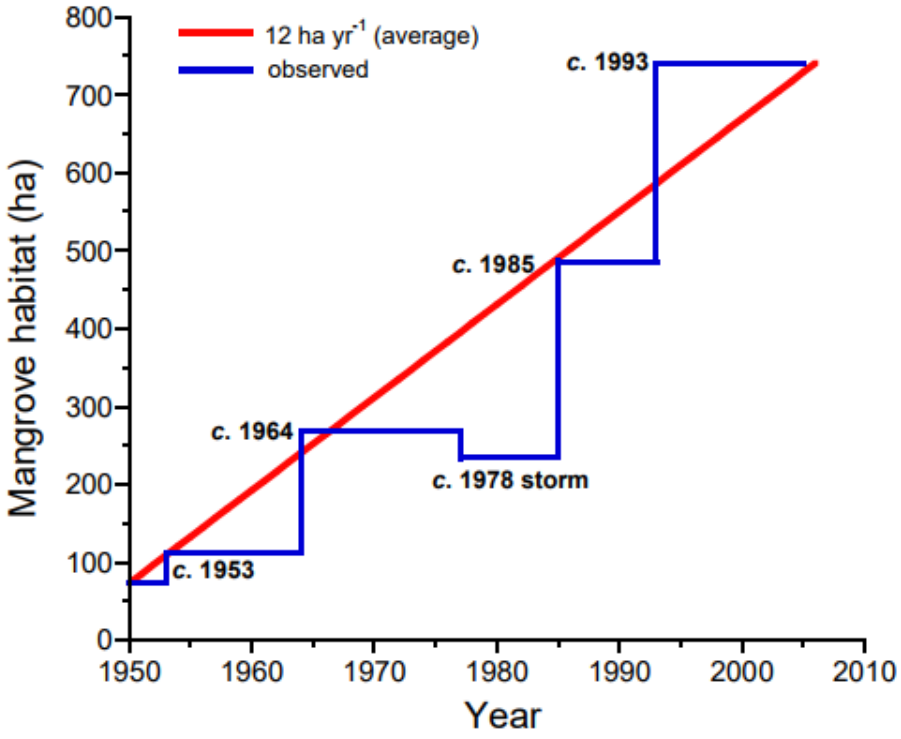

Figure 1.2: Mangrove coverage in the Firth of Thames, showing multiple seedling recruitment events. From Swales *et al.* (2007).

1.4.2 Hypotheses

The main hypothesis is that SSC and flow speeds will decrease into the mangroves and there will be a net flux of sediment into the forest. A secondary hypothesis is that flocculation will be enhanced at the fringe of the forest owing to turbulence at the scale of the pneumatophores, but flocculation will decrease further into the forest as flow speeds and turbulence intensities decrease.

1.4.3 Thesis layout

Chapter 2 details the study site and presents the methodology used in data collection and analysis phase of the study. Chapter 3 provides key results and observations from the field experiments. Chapter 4 presents a discussion of the hydrodynamic and sediment transport processes in the mangrove forest and summarises the key findings. Future research questions are posed at the end of Chapter 4.

Chapter 2

Field and laboratory measurements

2.1 Introduction

A field experiment was conducted to elucidate how vegetation induced changes in hydrodynamics, effect sediment transport in a mangrove forest. Field work was followed by laboratory analysis to calibrate instruments and to provide information on bed-sediment grain size.

2.2 Study site

Field observations were collected in the mangrove forest located at the southern end of the Firth of Thames (Figure 2.1). The mangrove forest is approximately 1 km wide and has a distinctive fringe area, grading into dense mangrove forest, set in an extremely muddy environment. A detailed description of the study site was given in section 1.4.1. Measurements were focussed around the transition zone from the intertidal mudflat, across the fringe region into the forest. We define a N-S transect with x = 0 m at the fringe indicating the boundary between mudflat and forest. There were 5 measurement sites with the outermost site (x=-50 m) located on the intertidal mudflat, one just inside the fringe at x=5 m and three extending into the forest (at x=35 m, x=65 m and x =115 m) (Figure 2.2-2.3). Site 5 experiences the least inundation due to elevation changes (Figure 2.2).

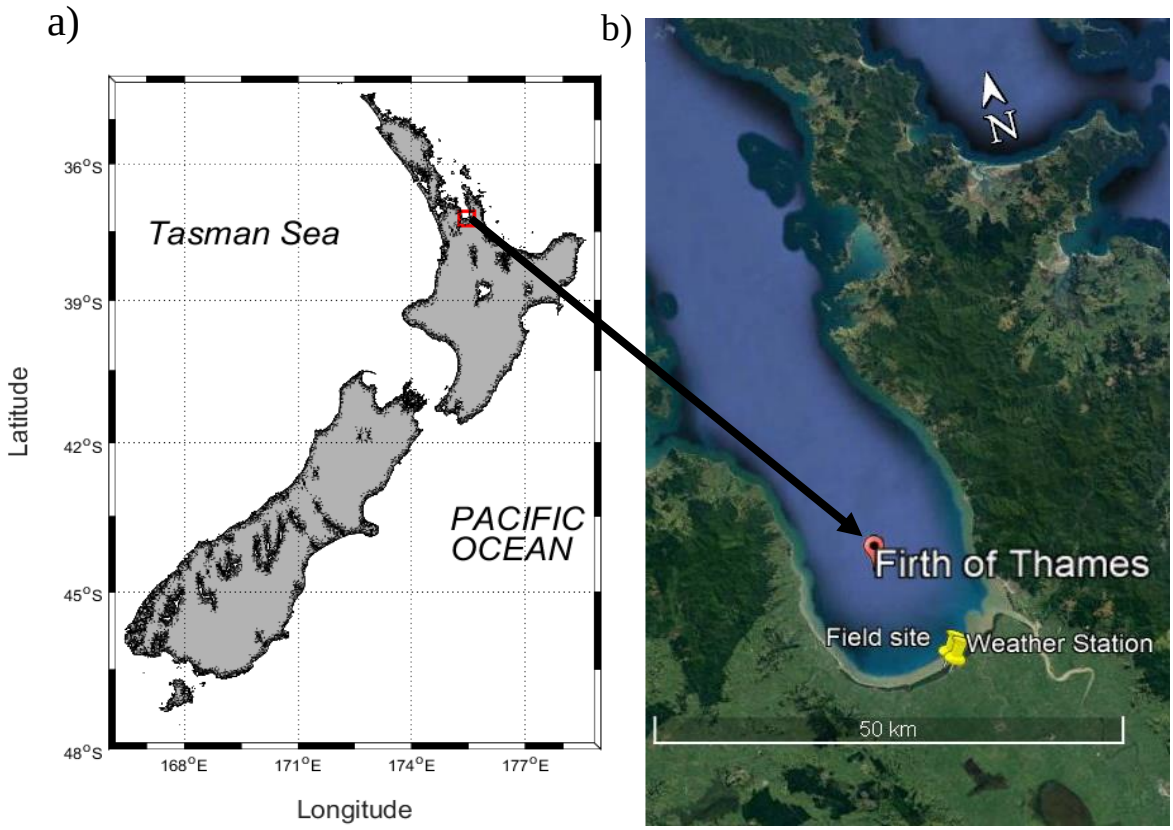

Figure 2.1: Field site location. a) New Zealand with the Firth of Thames highlighted in red, b) The Firth of Thames with the field site and weather station locations.

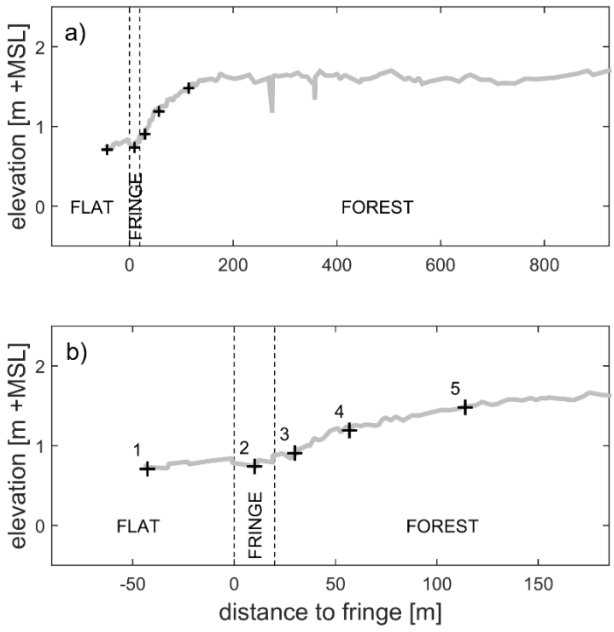

Figure 2.2: Elevation profiles of the Firth of Thames field site, showing distance from the mudflat in the forest along the x-axis and elevation (m+MSL) on the y-axis. a) is the topography of the entire mangrove forest, b) shows the elevation profile of the 5 measurements site. Data provided by Dr Erik Horstman (University of Waikato).

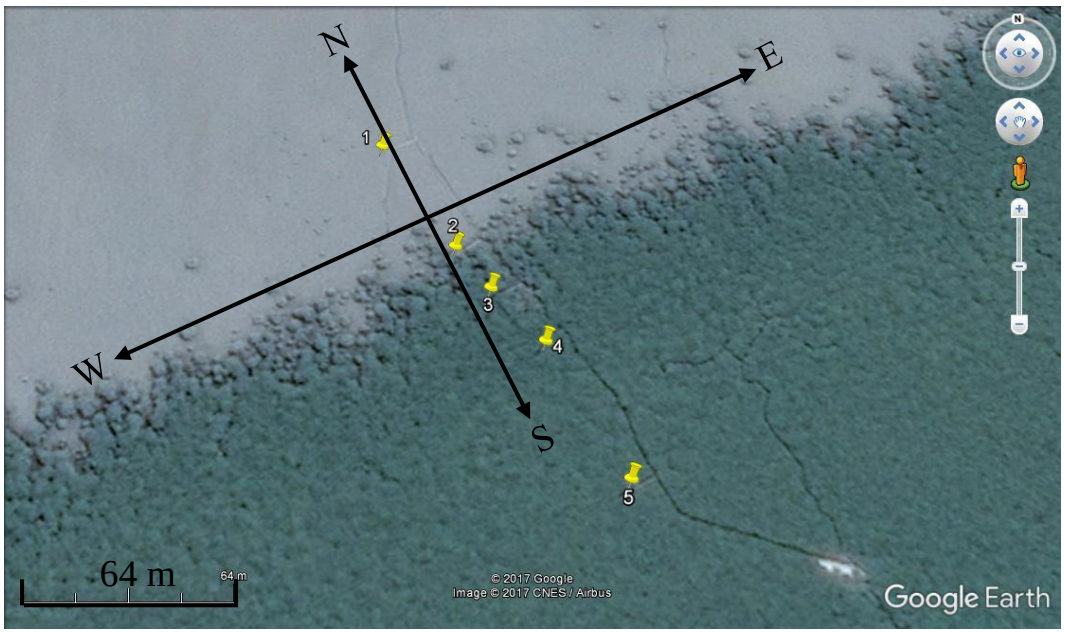

Figure 2.3: Google Earth Image from 20/01/2017 showing sites 1 to 5. Arrows indicate components of velocity discussed in the text, with E-W representing the u-velocities and N-S, the y-velocities. South and west are negative and north and east are positive.

2.3 Experimental design and measurements

The main field experiment took place over a 1-week period (12th December 2016 – 19th December 2016). The aim of the fieldwork was to collect hydrodynamic data, suspended sediment concentration data and images of flocs to ascertain in-situ particle size (Table 2.1). Due to the muddy substrate, it is extremely difficult to deploy frames and obtain measurements without significant disturbance of the seabed. To overcome this difficulty, a raised boardwalk was constructed to help facilitate the experiment. Building of the boardwalk took place in January 2016 and the experiment was carried out in December 2016, so the bed-sediment had sufficient time to return to an undisturbed state before the experiment took place. In addition to the main trunk line of the boardwalk, five side arms were also constructed at each of the measurement locations. Each side arm had a retractable cantilevered bridge, which was pushed out above the sediment (Figure 2.4), allowing the deployment of equipment away from the main structure and with minimal disturbance of the bed. Bridges are retracted when experiments were underway thus minimising any adverse effects the boardwalk may have on the flow, sediment dynamics and floc formation. Instruments were typically deployed 4-5 m away from the end of each side arm.

Table 2.1: Equipment details and variables measured at each site. SPB = Samples Per Burst, HAB = Height above the bed

Site	Variables measured	Equipment	Notes
1,2,3, 4	Flocs	Camera	2 Hz
	Current velocities (45 cm profile)	Nortek Aquadopp	8 Hz, 4096 SPB, 3 secs between bursts, vertical resolution = 25 cm HAB (cm) = 0.38, 0.29, 0.37, 0.44 sites 1 – 4 respectively.
	Current velocities (single-point)	Nortek Vector	16 Hz, continuous, 8192 SPB
	Conductivity, temperature and depth	RBR Concerto	6 Hz, continuous, 3600 SPB
	SSC (backscatter)	Campbell Scientific OBS3+s. Seapoint turbidity sensor	Input to Vector, HAB (cm) =3, 6, 20, 14 (sites 1-4 respectively) Input to Concerto, HAB (cm) =27, 26, 38, 39 (sites 1-4 respectively)
5	Flocs	Camera	2 Hz
	Current velocities (single-point)	Vector	16 Hz, continuous, 8192 SPB
	Current velocities (45 cm profile)	Nortek Aquadopp	16 Hz, continuous, 8192 SPB, 3 secs between bursts, vertical resolution = 25 cm HAB = 0.22 cm
	Conductivity, temperature and depth	RBR Concerto	6 Hz, continuous, 3600 SPB
	SSC (backscatter)	Campbell Scientific OBS3+s. Seapoint turbidity sensor	Input to Aquadopp, HAB (cm) =4 Input to Concerto, HAB (cm) =23

Figure 2.4: a) Cantilevered bridge extended from the boardwalk with frame and attached instruments being set-up at site 1 on the intertidal mudflat, b) Programming floc cameras at site 1, without disturbing the sediment.

At all sites Nortek Acoustic Doppler Velocimeters (ADVs) were used to measure the 3-dimensional velocity field. At sites 1-4 each ADV was integrated with the optical backscatter sensors (OBS), which was deployed near the bed. Also, at each site, a second OBS was integrated with an RBR Concerto to measure optical backscatter, the OBS on the concerto was deployed higher in the water column than the OBS interfaced to the ADV. Optical backscatter was used to estimate SSC. An OBS works by emitting infrared light and then measuring the backscattered light intensity (*I*) that has been reflected back from a suspension of particles. Since *I* is proportional to SCC a linear relationship can be used to convert *I* into estimates of SSC (MacDonald, 2009). In addition to the ADV velocity measurements, 2 MHz Nortek Aquadopps (Acoustic Doppler Current Profilers (ADCPs)), operating in pulse-to-pulse coherent mode, were used to measure the 3D velocity components over a short profile (~ 30 cm), with a vertical resolution of 2.5 cm. The Aquadopps were deployed above the bed and downward-facing to capture measurements very close to the bed. The Aquadopp at site 5 was integrated with a near-bed OBS sensor. Temperature and salinity were measured using the RBR Concerto CTDs (Conductivity Temperature Depth), where salinity values are derived from conductivity and temperature measurements.

Photographs of two of the frames and instrumentation are shown in (Figure 2.5). Additional information about the experiment setup and sampling strategy are provided in Figure 2.5.

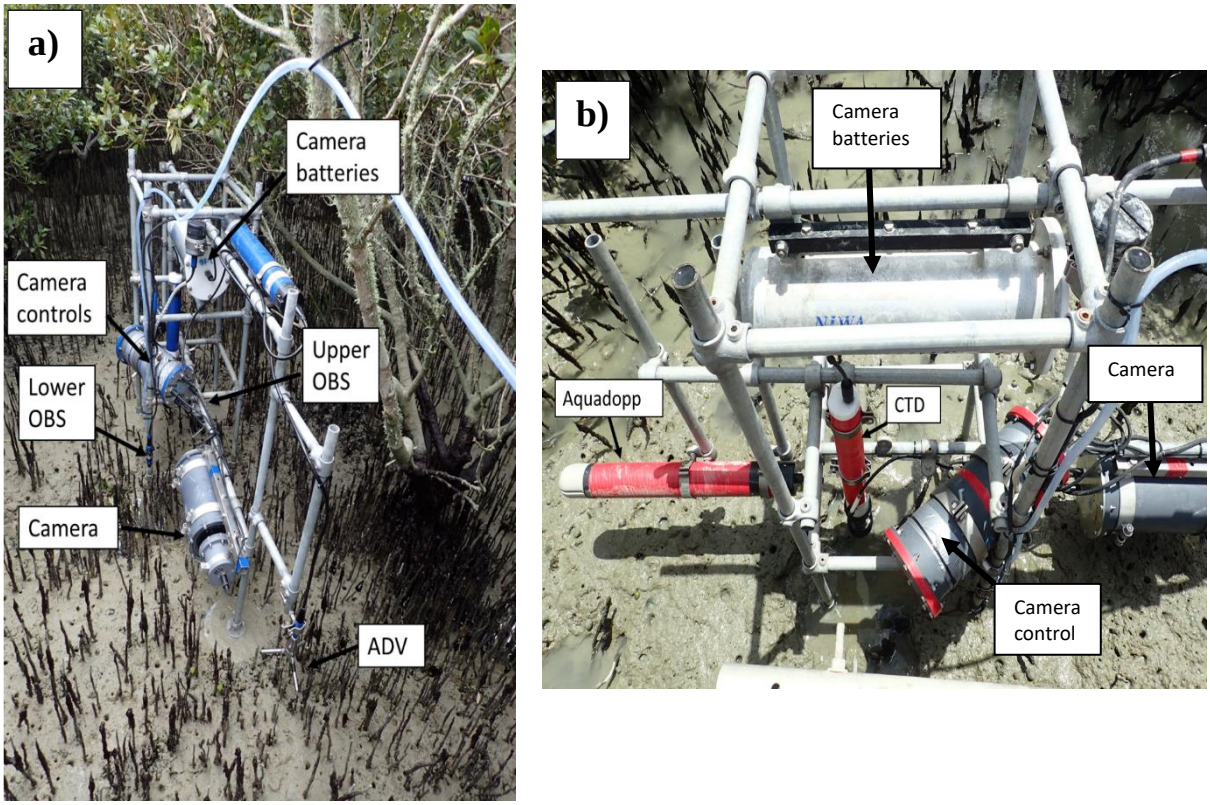

Figure 2.5: Frame with attached equipment: a) front view (site 3), note minimal disturbance by footprint of the frame b) side view (site 2).

Atmospheric pressure, rain-fall, wind speeds and direction were obtained from a weather station (Firth of Thames Ews), which is located at 1817420.0 E and 5878439.0 N (NZTM) (Figure 2.1). Wind speed and direction measurements were collected 10 m above the ground. Sediment samples were collected from the seabed at each site and analysed in the laboratory to provide estimates of the bed sediment grain size distribution.

2.4 Data quality control and processing

The data collected by the ADCPs, ADVs, OBSs and Concertos were processed using MATLAB. All velocity data was converted to ENU coordinates and was burst-averaged over 8.53 minutes with an interval between bursts of 10-minutes, furthermore, data were interpolated onto the same time interval for comparison. Data points that were recorded when the sensors were out of the water, were removed for all analyses. Additionally, low quality data was removed using a

correlation threshold of <70% (ADCPs) and <90% (ADVs), with gaps filled by linear interpolation. Aquadopp pressure data was also corrected for temperature dependence, and atmospheric fluctuations were removed. Data collected using Concertos were processed similarly. Data points that were recorded when the sensors were out of the water were removed and data were burst averaged with intervals between bursts of 10-minutes and interpolated on to the same time-scale as the velocities. Bed sediment surface grab samples from each site were sub-sampled for quality control. 20 ml of a 10% hydrogen peroxide solution was applied to each sample to remove organic material. Hydrogen peroxide was reapplied daily for approximately 3 weeks until the sediment sample stopped reacting to the chemical, indicating the organics had been removed. Calgon, a dispersal agent, was then added and a couple of hours later, the samples were sonicated for 30 minutes in order to disperse the particles. A Malvern laser particle sizer was used to analyse sediment size. Preliminary image analysis was carried out on the floc camera data using a qualitative approach.

2.4.1 OBS calibration

All instruments were calibrated in a laboratory using the same settings as in the field experiment. Calibrations were performed in a 50-l steel tank (Figure 2.6). Four pumps were mounted on the bottom to ensure that sediment in the tank was well-mixed and that sediment remained in suspension during the measurement period. Bed sediment samples from the five field sites were combined and sieved using a 62.5 μm mesh. Sediment was mixed into the water and added in quantities to obtain nominal NTU (Nephelometric Turbidity Units) values, targeting values over the range observed in the field. SSC was estimated from water samples collected at the start, halfway through and at the end of each calibration point. The water samples were filtered using Whatman glass microfiber filters (GF/C diameter 47 mm); which were weighed prior to washing and then dried for 24 hrs at 105^{o}C. Each sample was sub-sampled for quality control and filtered. The filters were then dried for 24 hours at 105 ^{o}C and weighed again. To remove organics and therefore to obtain an accurate estimate of the SSC, the filters were put in a muffle furnace for 4 hours at 550 ^{o}C. The filters were then weighed again. SSC was calculated as mass/volume (mg/l). Figure 2.7 shows a typical calibration curve for the ADV at site 4. The linear fits to calibration data were all of a high-standard, for the

Concerto-OBSs the mean r^2 value was 0.95544 (minimum = 0.9376), while for the Vector-OBSs the mean r^2 value was 0.9914 (minimum = 0.9826). For the OBS sensor attached to the Aquadopp at site 5 the r^2 value was 0.9938.

Figure 2.6: Tank and set-up used to calibrate OBS sensors.

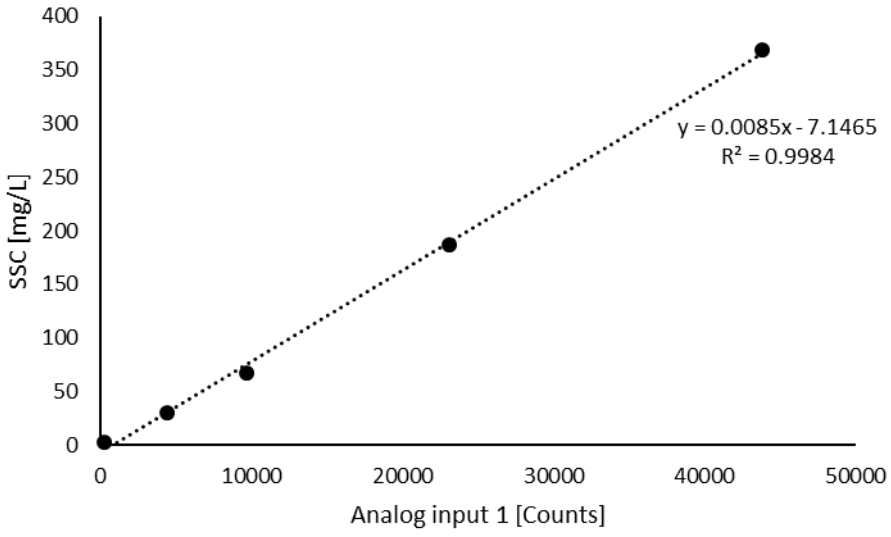

Figure 2.7: Example calibration result from a Campbell Scientific OBS3+ sensor (site 4, sensor attached to Nortek Vector ADV).

2.4.2 Wave statistic calculations

Wave statistics were calculated using linear wave theory following the method outlined in Green and Coco (2007). Mean spectral period (*T*) in s is given by:

$$T = m_0/m_1, \quad (2\text{-}1)$$

where m_n is the n^{th} moment of the power spectrum of the time-series of pressure recorded at the instrument, *h(t).* Significant wave height (H_{sig}) at the surface is obtained from the pressure time-series at depth, as

$$H_{sig} = 4h_{SD}\frac{\cosh(kh)}{\cosh[k(h-z^*)]}, \quad (2\text{-}2)$$

where h_{SD} is the standard deviation of *h(t)*, *k* is the wave number corresponding to period *T* and mean of *h(t),* calculated using the linear wave dispersion relationship and z^* is the depth below the surface of the pressure sensor. From H_{sig} and *T* the significant orbital velocity at the bed (u_{sigb}) was estimated as:

$$U_{sigb} = \frac{4\pi h_{SD}\cosh(kh)}{Tcosh[k(z^*+h)]\sinh(kh)}. \quad (2\text{-}3)$$

2.4.3 Sediment flux calculations

Fluxes of suspended sediment were calculated to determine if there is an influx of sediment into the mangrove forest from the intertidal mudflat. Fluxes were calculated as,

$$Q(t) = \int_0^h C(z,t)V(z,t)dz \quad (2\text{-}4)$$

where *c(z,t)* is the SSC and *v(z,t)* is the velocity in the N-S direction, which is normal to the orientation of the mangrove fringe. In case of an offshore directed current (N), the flux (*Q*) will be positive, alternatively negative *Q* corresponds to a flux into the mangrove forest. In order to estimate fluxes, it was necessary to estimate profiles of both N-S velocity and SSC throughout the full water depth. Velocity in the upper water column (above the profile) was taken as uniform and equal to the value at the furthest measurement point from the bed. To estimate near-bed velocities, a simple linear interpolation was made from the value at the lowest measurement extrapolated to zero at the bed, representing no-slip conditions. For SSC we tested four models, fitted based on the two measured values. Model one is a linear interpolation of the two data points and is given by,

$$C(z) = P(1)z + P(2), \quad (2\text{-}5)$$

where the slope *p(1)* and intercept *p(2)* are fitted constants used to calculate concentration over the water column *C(z).*

Model two assumes a constant diffusivity over the water depth:

$$C(z) = C_R \exp\left(\frac{-W_s}{\kappa_o}\, z\right), \tag{2-6}$$

where C_R is a reference concentration, W_s is settling velocity and κ_o is diffusivity. To evaluate *C(z)* from Eqn 2-6, an equation of the form:

$$C(z) = A(1)\exp(-A(2)z), \tag{2-7}$$

was fitted to the SSC values measured at the two heights. The result of the fit yield parameters $A(1)=C_R$, *and* $A(2)=W_s/\kappa_0$.

Model three assumes a linear profile of diffusivity with,

$$C(z) = C_R \left(\frac{z}{z_a}\right)^{-W_s/KU_*}, \tag{2-8}$$

where z_a is a reference height (assumed to be 0.01 m), *K* is the von Kármán constant, 0.4 and U_* is friction velocity. To evaluate *C(z)* from Eqn 2-8, an equation of the form:

$$C(z) = A(1)\left(\frac{z}{z_a}\right)^{-A(2)} \tag{2-9}$$

was fitted to the SSC values measured at the two heights. The result of the fit yield parameters $A(1)=C_R$, *and* $A(2)=W_s/\kappa_0$.

Lastly, model four assumes a parabolic profile of diffusivity of the form:

$$C(z) = C_R \left(\frac{z}{h-z}\ \frac{h-z_a}{z_a}\right)^{-W_s/KU_*}, \tag{2-10}$$

where *h* is water depth. To evaluate *C(z)* from Eqn 2-10, an equation of the form:

$$C(z) = A(1)\left(\frac{z}{h-z}\ \frac{h-z_a}{z_a}\right)^{-A(2)} \tag{2-11}$$

again was fitted to the SSC values measured at the two heights. The result of the fit yield parameters $A(1)=C_R$, *and* $A(2)=W_s/\kappa_0$.

Chapter 3

Results

3.1 Introduction

In this chapter results and observations from the measured data are presented.

3.2 Environmental conditions

A wind rose for the experimental period and for the entire 7-year period that the weather station has been operating (10/11/2010-27/07/2017) are shown in Figures 3.1a and 3.1b, respectively. From Figure 3.1a and 3.1b it is apparent that the winds experienced over the deployment period are typical of the long-term wind climate. During the experiment, wind speeds were variable with a maximum speed of 11.4 m/s and a mean of 4 m/s. The wind directions were from the south-south-west to north. These conditions were similar to the overall trends visible in the 7-year record: the wind direction was predominantly from the south-south-west and north-north-west. Wind speeds varied between 0-14 m/s with a mean of 3.5 m/s.

Time-series of the wind data for the duration of the experiment are shown in Figure 3.2, in addition to water depths, salinity and temperature across all five sites. Maximum water depths decreased from site 1 on the mudflats (1.33 m), to site 5 in the mangrove forest (0.5 m) (Table 3.1). Water temperatures were similar between sites during the night but exhibited some differences in daytime temperature with temperatures decreasing into the forest. This temperature change into the forest is likely to be from the heating of the intertidal mudflats and water column that occurs during the day. Within the mangroves, the substrate is not heated to the same extent, hence temperatures inside the forest are lower. The night-time minimum water temperature was 10.5 ^{o}C (site 1) and the daytime maximum was 24.5 ^{o}C (site 1). Salinity did not vary greatly between each site; however, the innermost site (Site 5) had the highest values in general. Figure 3.3 shows that there were no significant rain events during the experiment, but there was some rain prior to the deployment (5 mm) and a smaller event (4 mm) shortly after retrieval.

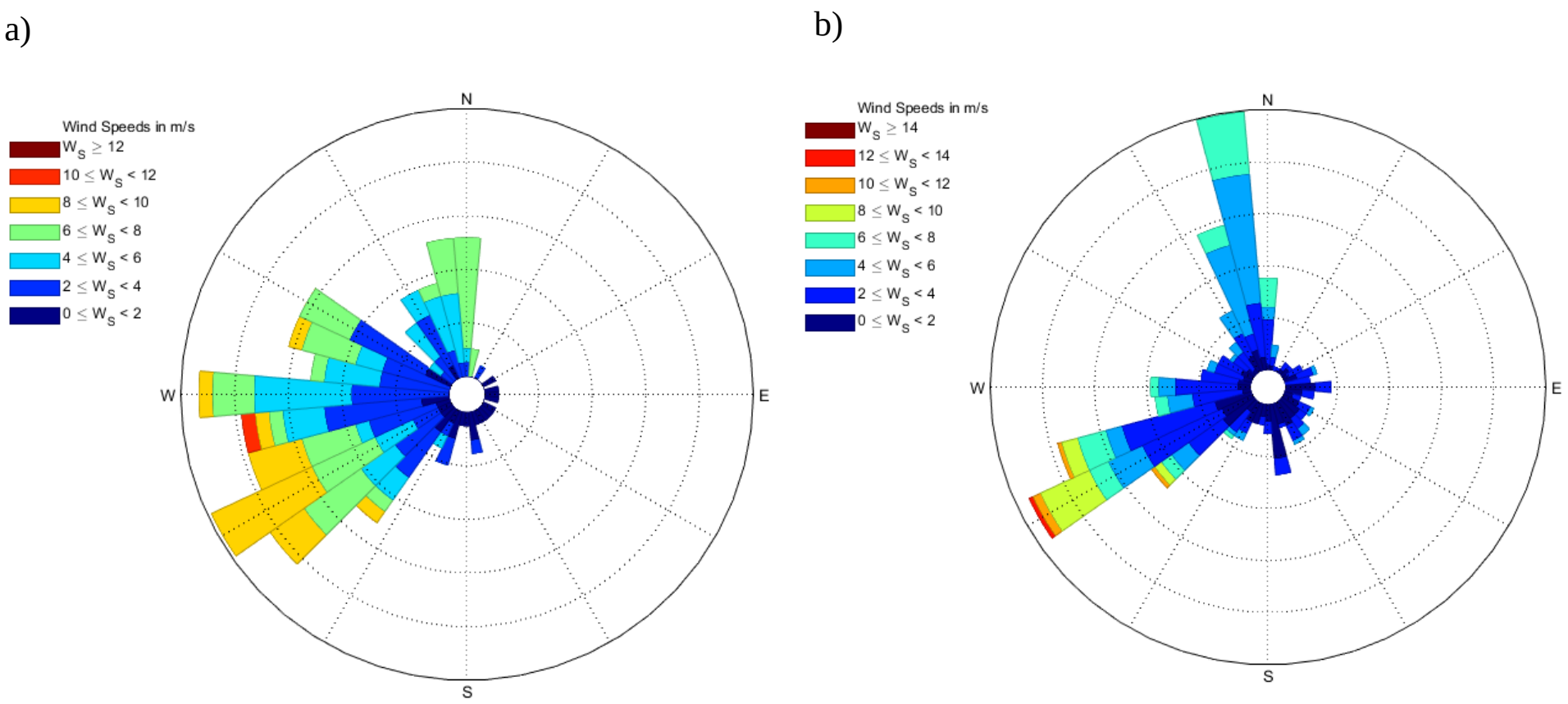

Figure 3.1: Wind rose created using hourly wind data from a NIWA weather station at Firth of Thames (-37.21522, 175.4503) a) during the experimental period, 12/12/2016-19/12/2016, b) over the period: 10/11/2010-27/07/2017. Colours indicate wind speeds, bars indicate direction from and the length of the bars indicates the frequency of occurrence of the wind conditions.

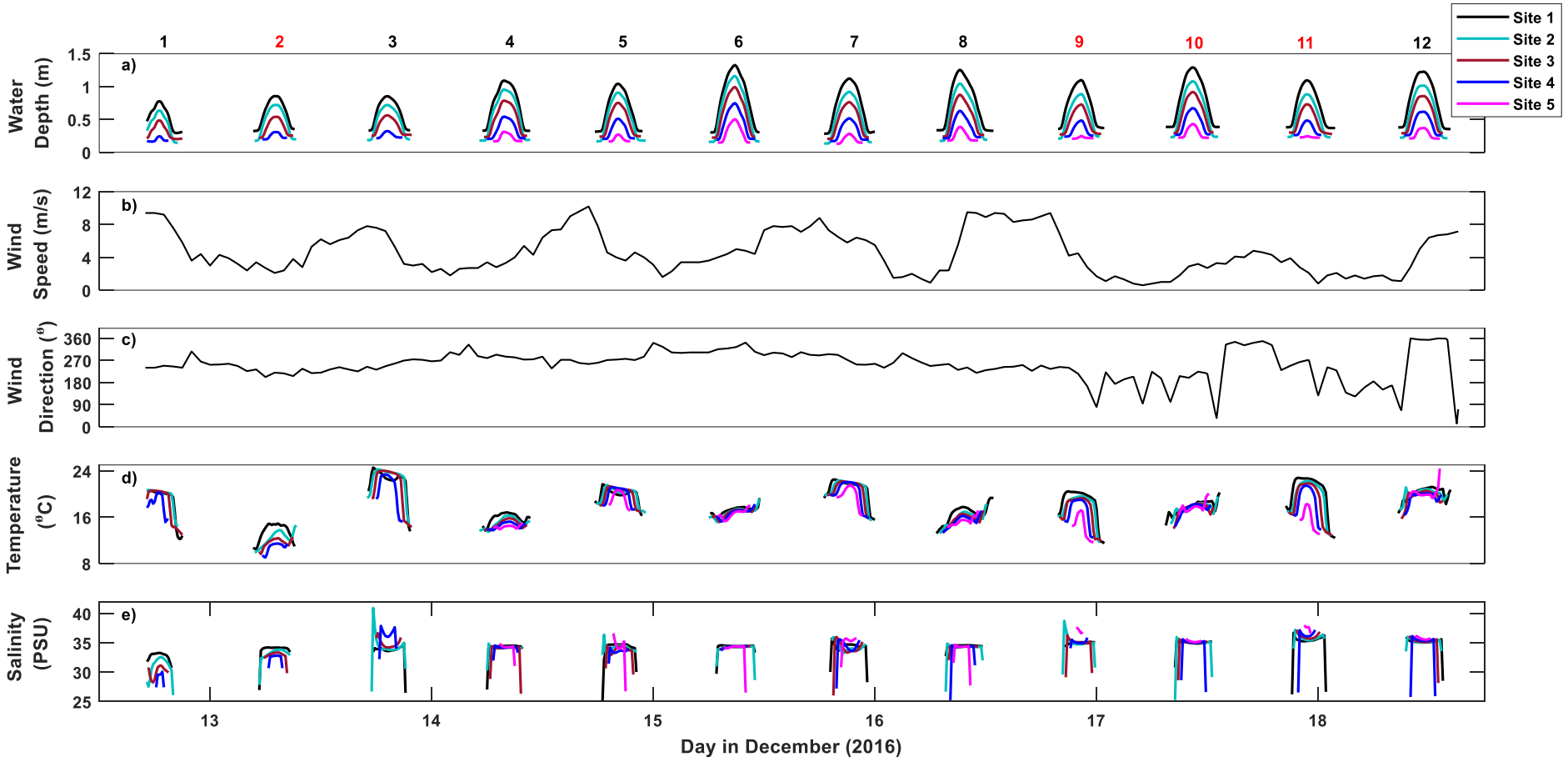

Figure 3.2: Measured conditions at the Firth of Thames study site (12th December 2016 – 19th December 2016). (a) water depths, (b) wind speeds, (c) wind directions (direction from), (d) temperature and (e) salinities. Numbers above refer to tide number, referenced in the text. Red numbers = no wave conditions, black numbers = wave conditions.

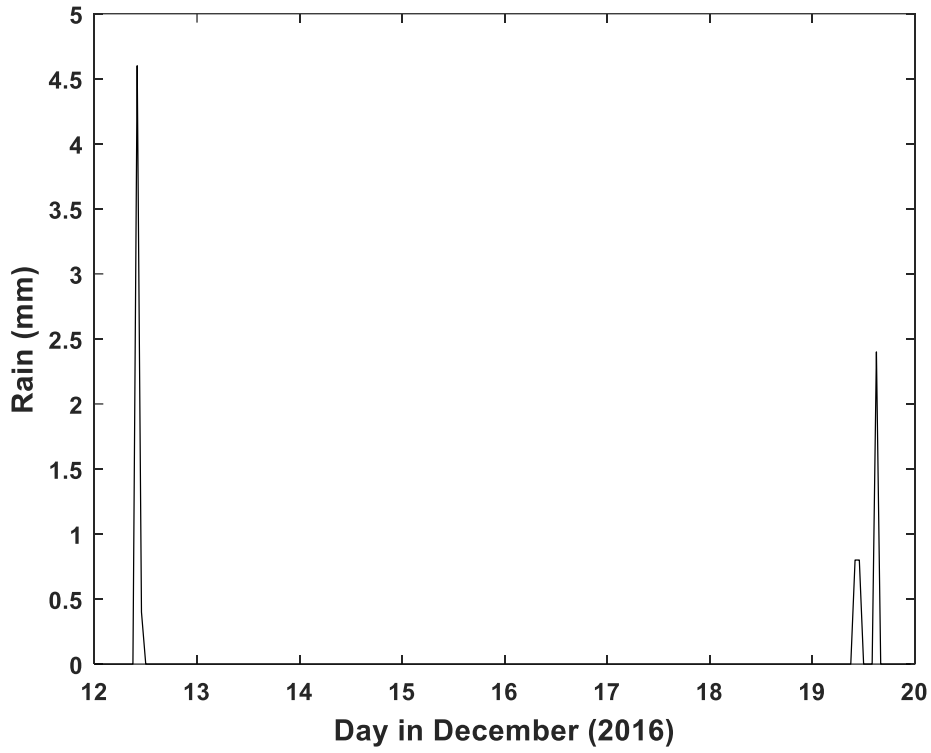

Figure 3.3: Hourly rainfall (mm) from NIWA weather station at Firth of Thames Ews (-37.21522, 175.4503), 10/11/2010-27/07/2017.

3.3 Waves

Table 3.1 shows the maximum and mean values of h, H_s, U_{sigbed} and T_m (s) at each site. h, H_s and U_{sigbed} all decrease into the mangrove forest from the intertidal mud flat. T_m were similar across sites with mean values of around 3 s.

Table 3.1: Maximum and mean wave statistics for each site

Site	h (m)		H_s(m)		U_{sigbed} (m/s)		T_m(s)	
	Max	**Mean**	**Max**	**Mean**	**Max**	**Mean**	**Max**	**Mean**
1	1.33	0.70	0.29	0.09	0.36	0.13	8.87	3.03
2	1.16	0.55	0.23	0.06	0.32	0.10	9.65	3.17
3	0.99	0.48	0.16	0.04	0.21	0.08	9.37	3.24
4	0.75	0.35	0.11	0.02	0.17	0.05	8.99	3.39
5	0.50	0.25	0.05	0.01	0.11	0.03	8.80	3.21

Wave statistics and water depth are plotted against wind speed and direction in Figure 3.4. Several observations can be made from this data. Firstly, H_s and U_{sigbed} are greatest when the wind blows from the west or north. Larger waves would be

expected during a northerly wind owing to the larger fetch (See figure 2.1). In general, times with small H_s correspond to times of slow wind speeds and minimum-fetch aligned wind-directions. However, this relationship did not always occur. For example, waves with a H_s of up to 0.2 m were present during tide 5, despite average winds for the period, with wind speeds slightly greater than experiment mean at 5 m/s and a wind direction from the west, suggesting that during this time waves were not locally generated. As expected, during a southerly wind, H_s and U_{sigbed} are small. H_s and U_{sigbed} are generally greatest either at the beginning of the flood tide or end of ebb tide as opposed to at high tide. However, during northerly winds H_s and U_{sigbed} can remain large throughout the tide. An example of these conditions are tide 6, which corresponds to a period when the wind direction was from the NW. H_s and U_{sigbed} decrease into the forest, whereas T_m values are relatively similar across all sites and do not exhibit a clear trend with distance into the forest.

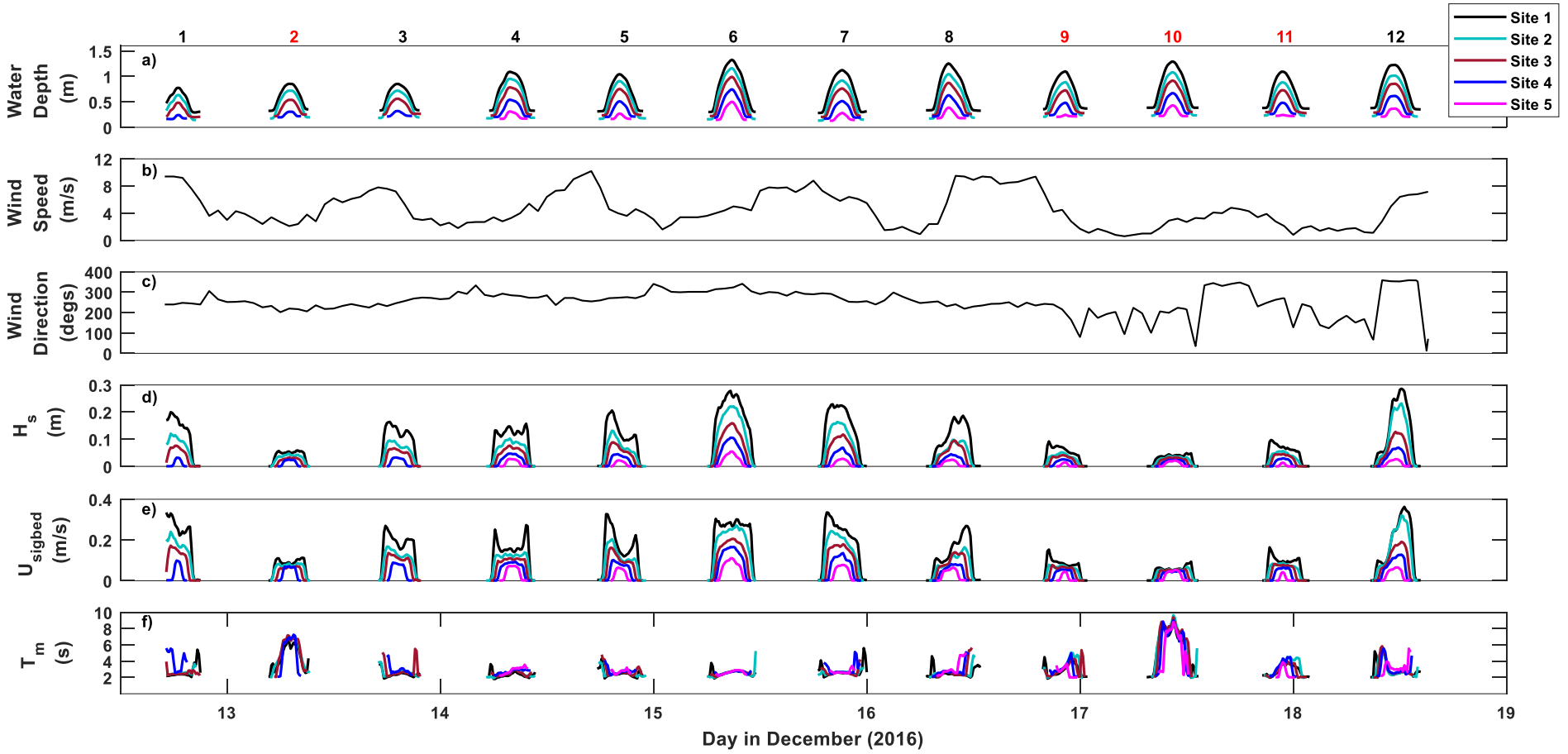

Figure 3.4: Wave statistics from all sites shown with wind conditions (b, c), (a) water depth *h* (m), (d) significant wave height *Hs* (m), (e) significant orbital velocity at the bed, U_{sigbed} (m/s) and (f) mean wave period T_m (s). Numbers above refer to tide number, referenced in the text. Red numbers = no wave conditions, black numbers = wave conditions.

Figure 3.5 shows a wave spectra from a 10-minute period that occurred during a period of large waves. A Hanning window with a 70 % overlap was applied. The spectra has 32 degrees of freedom and a 95 % confidence interval. The main peak of the spectra corresponds to locally generated short-period wind waves of 2.8 seconds. There are also two smaller peaks corresponding to energy at 2-s periods and longer periods of 12.5 s, likely indicating swell wave energy.

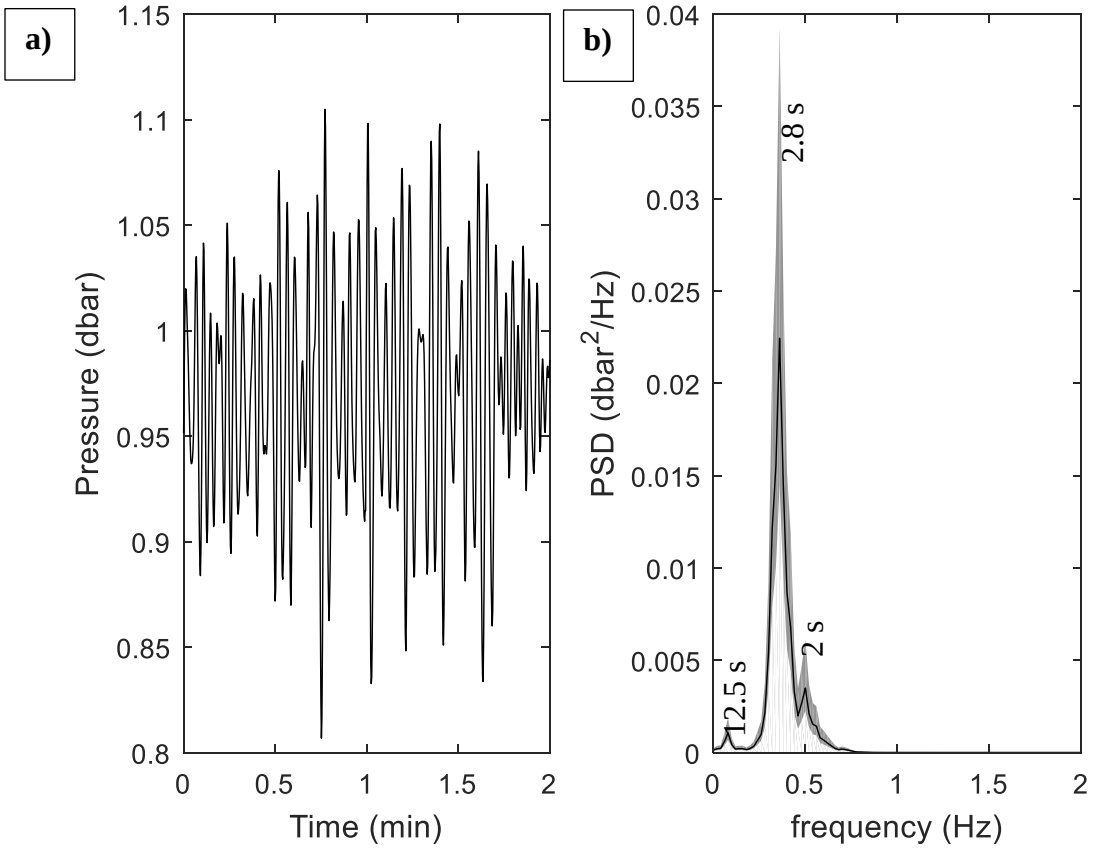

Figure 3.5: Example pressure data from tide 6 (15th December) from site 1. a) shows a short 2-min time series of pressure data. b) is the corresponding wave power spectral density from the full 10-min burst. The grey shading are the 95 % confidence intervals and the spectrum has 32 degrees of freedom.

To observe the effects of waves more clearly in further analyses, tides have been split into two categories, those with greater wave activity defined as Hs > 0.1 m (tides 1, 3-8 and 12) and those with low wave energy (Hs < 0.1 m), at site 1 on the mudflat (see figure 3.4).

3.4 Current velocities

Velocities were measured at each site using Nortek Aquadopps operating in high-resolution pulse to pulse coherent mode. When interpreting these velocities, consideration needs to be made for the fact that the instruments were downward facing and only the lower, approximately 40 cm of the water column was measured, missing what is occurring above that level. Velocities were burst-averaged, and therefore averaged out wave-induced currents. Due to the orientation of the forest, the fringe is essentially E-W oriented (Figure 2.3) so that N-S velocities correspond to off- and onshore flows.

Figure 3.4 shows that the hydrodynamics at the field site are strongly influenced by winds. With this in mind we firstly examine the hydrodynamics at the field site during calm periods, and then secondly during periods of increased winds.

3.4.1 Hydrodynamics during calm periods

During periods of minimal winds (tides 2 and 9-11), which generally corresponded to winds from the south and wind speeds < 3 m/s (Figure 3.4), mean current velocities at site 1 were ~0.049 m/s. Direction of flow was south on the flood tide and north on the ebb tide (at all sites, Figures 3.6-3.10). With southerly winds, the E-W current was directed to the west and there was generally little variation in magnitude and direction (e.g. tide 10). Maximum N-S currents usually occurred at the beginning to mid-flood tide and at the end of the ebb tide. Currents did not reduce monotonically into the forest, but sites in the forest did have smaller velocities than at site 1 on the mudflats (Table 3.2).

3.4.2 Hydrodynamics during windy periods

During periods of higher wind energy (tides 1, 3-8 and 12), with wind speeds >4 m/s and blowing from more westerly and northerly directions (Figure 3.4), mean current velocities were ~0.054 m/s at site 1. As with calm periods, currents did not reduce monotonically into the forest, but sites in the forest did have smaller velocities than at site 1 on the mudflats (Table 3.2). Direction of flow was generally north throughout these higher wave energy tides at site one. At all other sites, currents were south on the flood tide and north on the ebb tide (Figures 3.6-3.10).

Figure 3.6 shows that during times of strong winds, the N-S velocity component can set in a constant offshore direction throughout the entire duration of the tide at site 1 (e.g. tide 1 and 3-5). Tides 6 and 7 are almost entirely in an offshore direction too. At site 1, during westerly winds the E-W current is typically directed towards the east. Whereas for a northerly wind, the E-W current is directed to the west (e.g. tide 6). To verify these seemingly unusual observations, the N-S component of velocities were compared to the N-S component of the velocity measurements collected by the Nortek Vector (Figure 3.11). The magnitude and direction of the velocities agree well, thus providing confidence in the measured velocities from the Aquadopp. Entirely positive N-S components of currents are shown in a tidal stage diagram for a single tide (tide 4) at site 1 (Figure 3.12a) and compared to Figure 3.12b, which shows a tidal stage graph that has a more 'typical' pattern, with flood (southerly) and ebb (northerly) currents, from tide 10 (during calm periods) at site 1. As with calmer periods, maximum N-S currents usually occurred at the beginning to mid-flood tide and at the end of the ebb tide.

At site 2 (Figure 3.7), the E-W currents are typically directed to the east, and have increased magnitude and variability in comparison to times with minimal waves. For example, throughout tide 3, during a period of increased wind speed, there is more variability in the magnitude of the currents, whereas during tide 2, which has minimal waves, the wind velocities were small and the currents showed little variability in speed. All except two of the tides are ebb dominant (moving in the offshore direction). Tide 5 and 6 are only slightly dominant in a southerly direction (approximately 0.01 m/s faster than the northerly directed current). None are entirely northward directed as they are at site 1. The southerly currents tend to be strongest before high tide in the middle of the measured profile, often the currents are near zero at the top of the profile and at the bed on the flood tide. The northward currents tend to be stronger at the end of the ebb tide or after high tide until the end of the ebb, and always strongest at the top of the water column.

At sites 3 (Figure 3.8), 4 (Figure 3.9) and 5 (Figure 3.10) the velocity structure is more 'typical' over all tides, with southward and northward directed currents on the flood and ebb tides, respectively. Currents become increasingly flood dominant (moving in the onshore direction) towards site 5, where all tides are flood dominant. Variability in the flow speeds decreases slightly into the forest, particularly in the

E-W and vertical (z) direction. Peak horizontal flow velocities were largest at site 1, followed by site 4, 5, 3 and the slowest at site 2 (Figure 3.13 and Table 3.2). N-S currents also did not monotonically decrease with distance into the forest, with strongest currents occurring at sites 1, 5, 4, 2 and the slowest velocities are found at site 3.

Table 3.2: Maximum horizontal flow velocities (m/s) for all sites over the period of the experiment

Site	Max (m/s)
1	0.0665
2	0.0110
3	0.0156
4	0.0272
5	0.0213

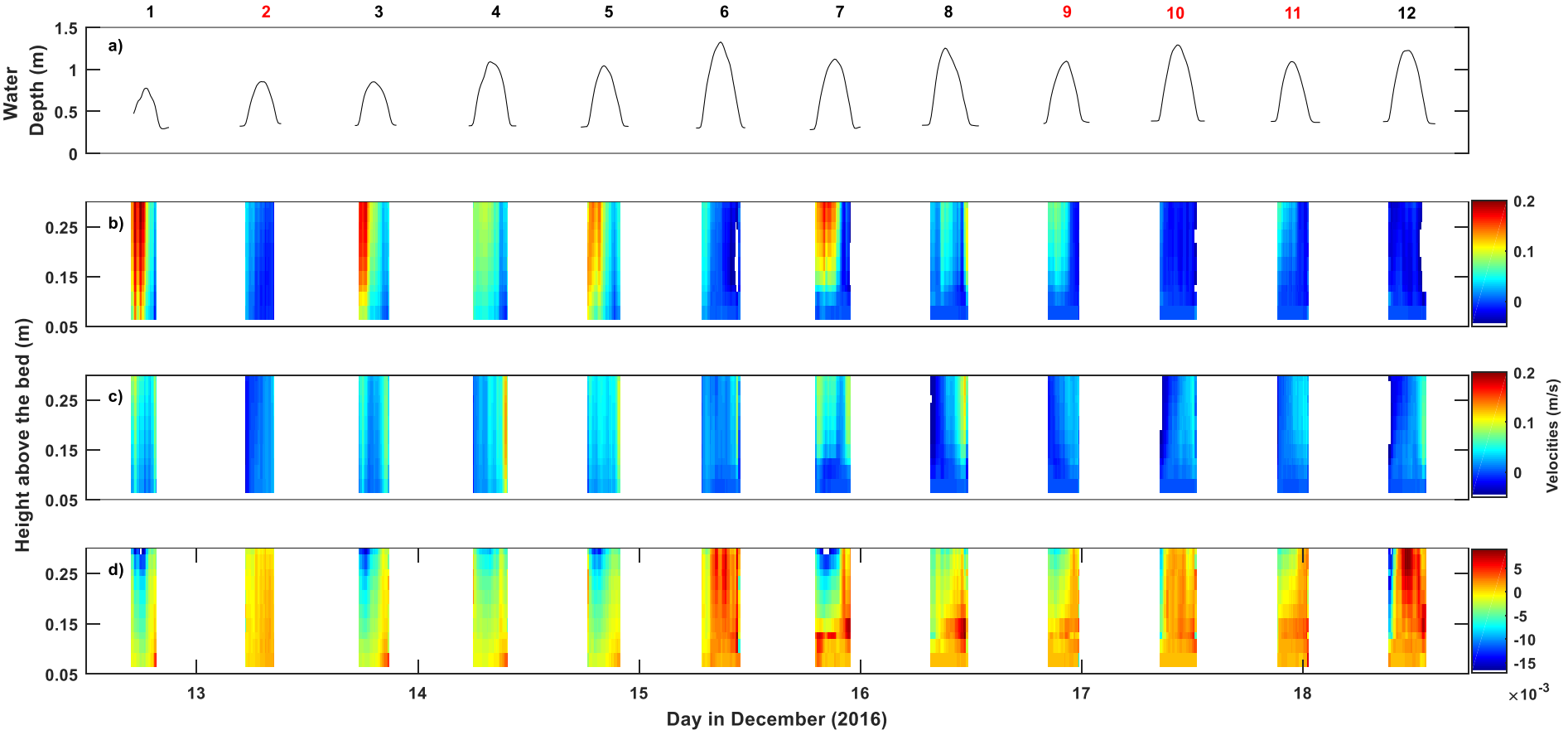

Figure 3.6: Water depths (a) and velocities (m/s) at site 1, Firth of Thames, b) u (E/W) c) v (N/S) d) w-direction (vertical). Numbers above refer to tide number, referenced in the text. Red numbers = no wave conditions, black numbers = wave conditions.

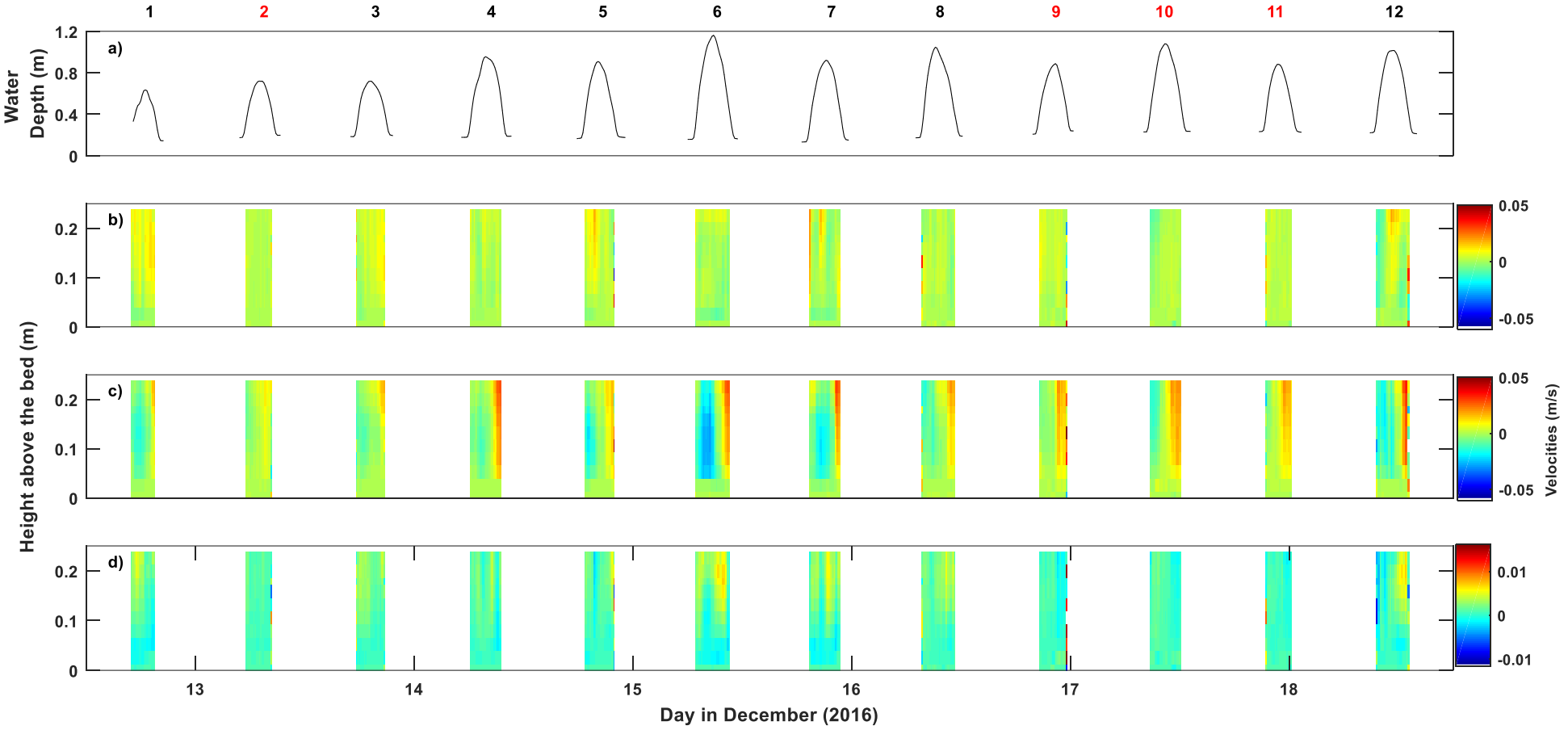

Figure 3.7: Water depths (a) and velocities (m/s) at site 2, Firth of Thames, b) u (E/W) c) v (N/S) d) w-direction (vertical). Numbers above refer to tide number, referenced in the text. Red numbers = no wave conditions, black numbers = wave conditions.

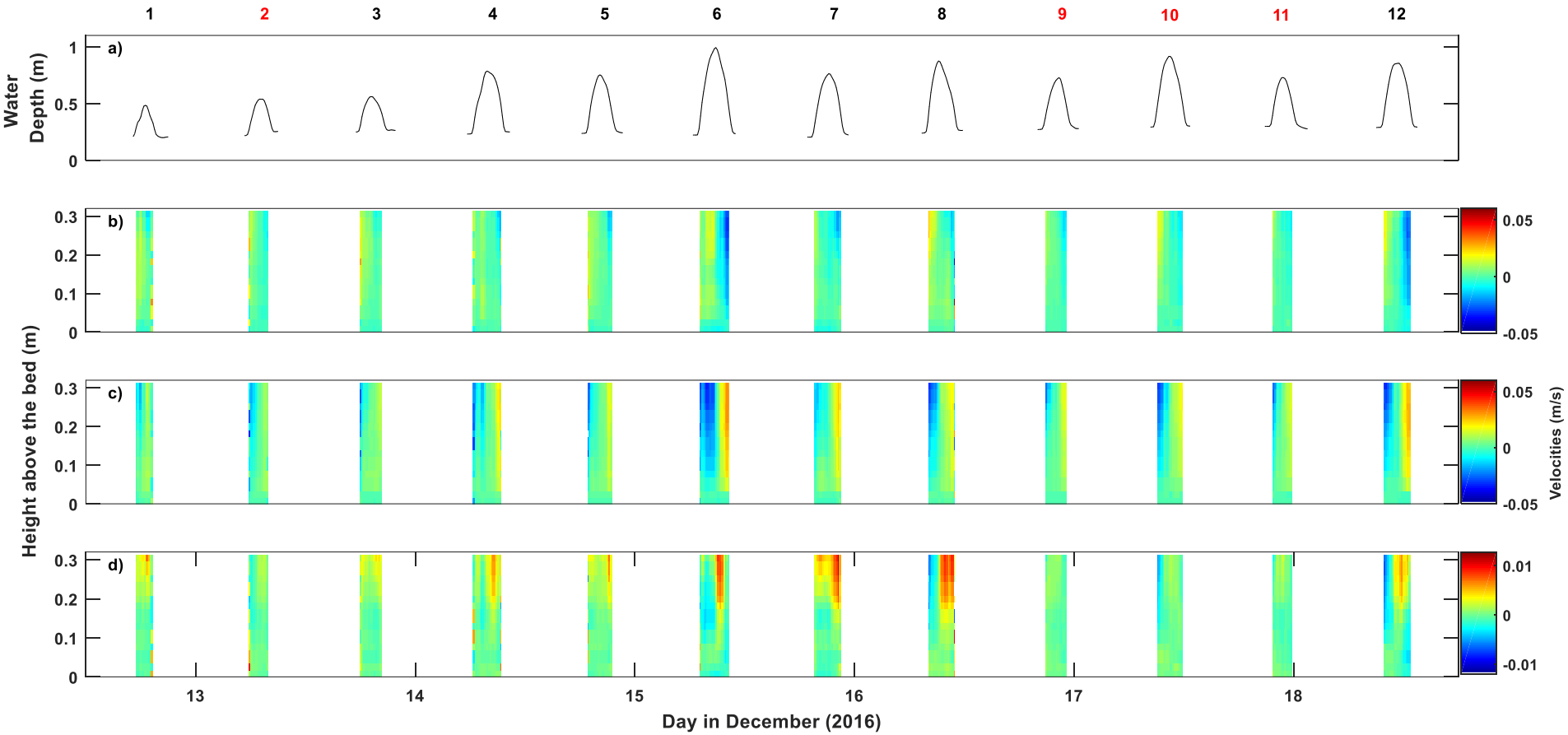

Figure 3.8: Water depths (a) and velocities (m/s) at site 3, Firth of Thames, b) u (E/W) c) v (N/S) d) w-direction (vertical). Numbers above refer to tide number, referenced in the text. Red numbers = no wave conditions, black numbers = wave conditions.

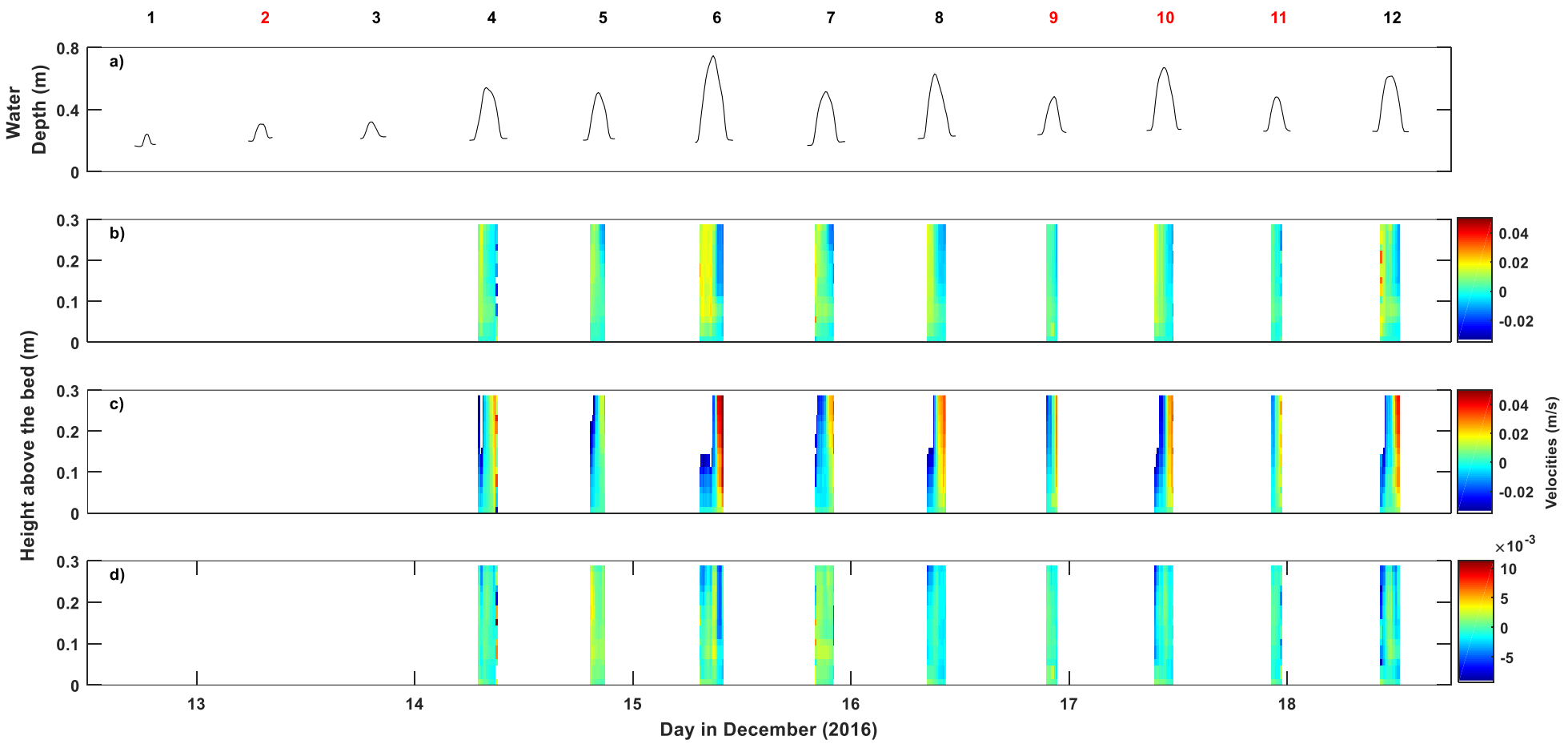

Figure 3.9: Water depths (a) and velocities (m/s) at site 4, Firth of Thames, b) u (E/W) c) v (N/S) d) w-direction (vertical). Numbers above refer to tide number, referenced in the text. Red numbers = no wave conditions, black numbers = wave conditions.

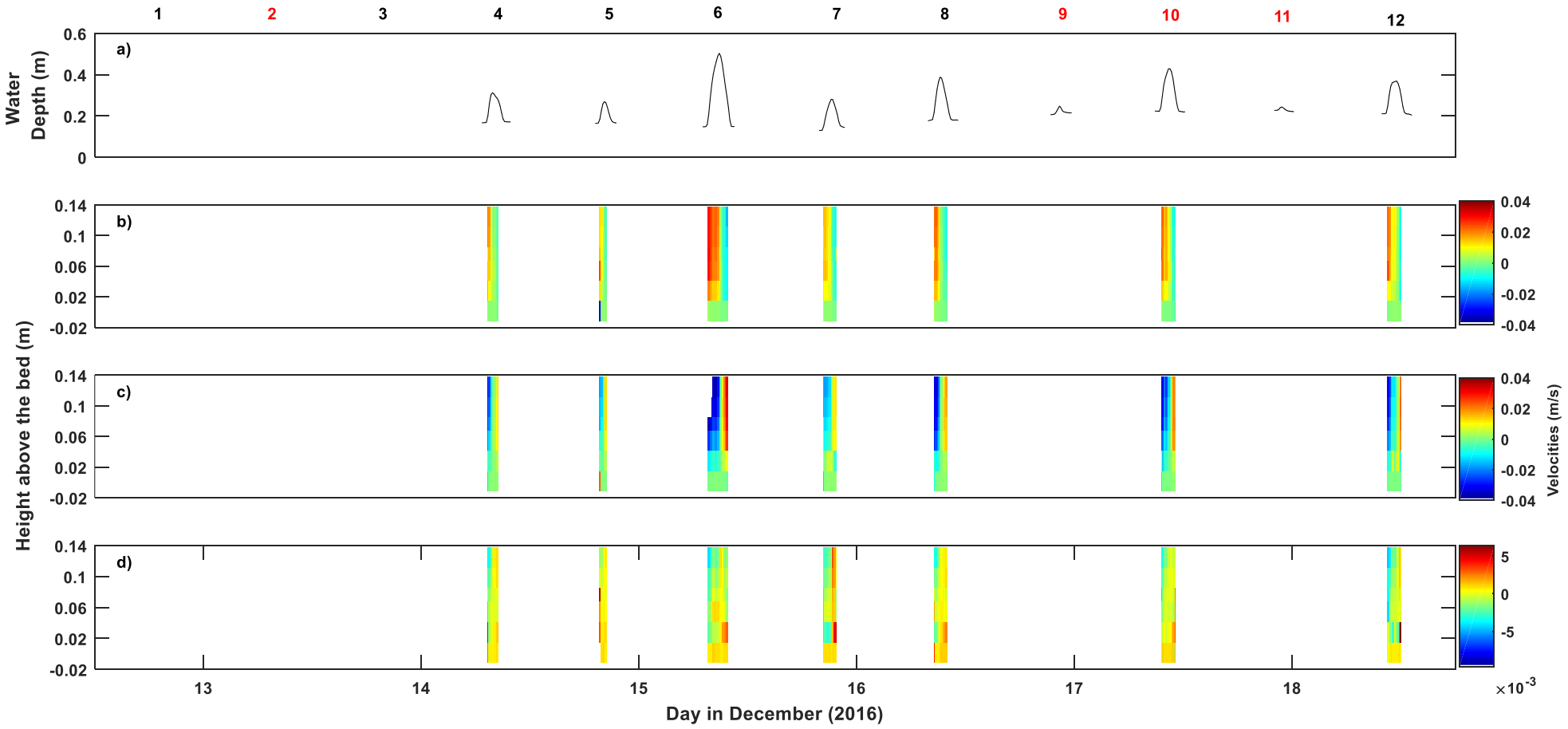

Figure 3.10: Water depths (a) and velocities (m/s) at site 5, Firth of Thames, b) u (E/W) c) v (N/S) d) w-direction (vertical). Numbers above refer to tide number, referenced in the text. Red numbers = no wave conditions, black numbers = wave conditions.

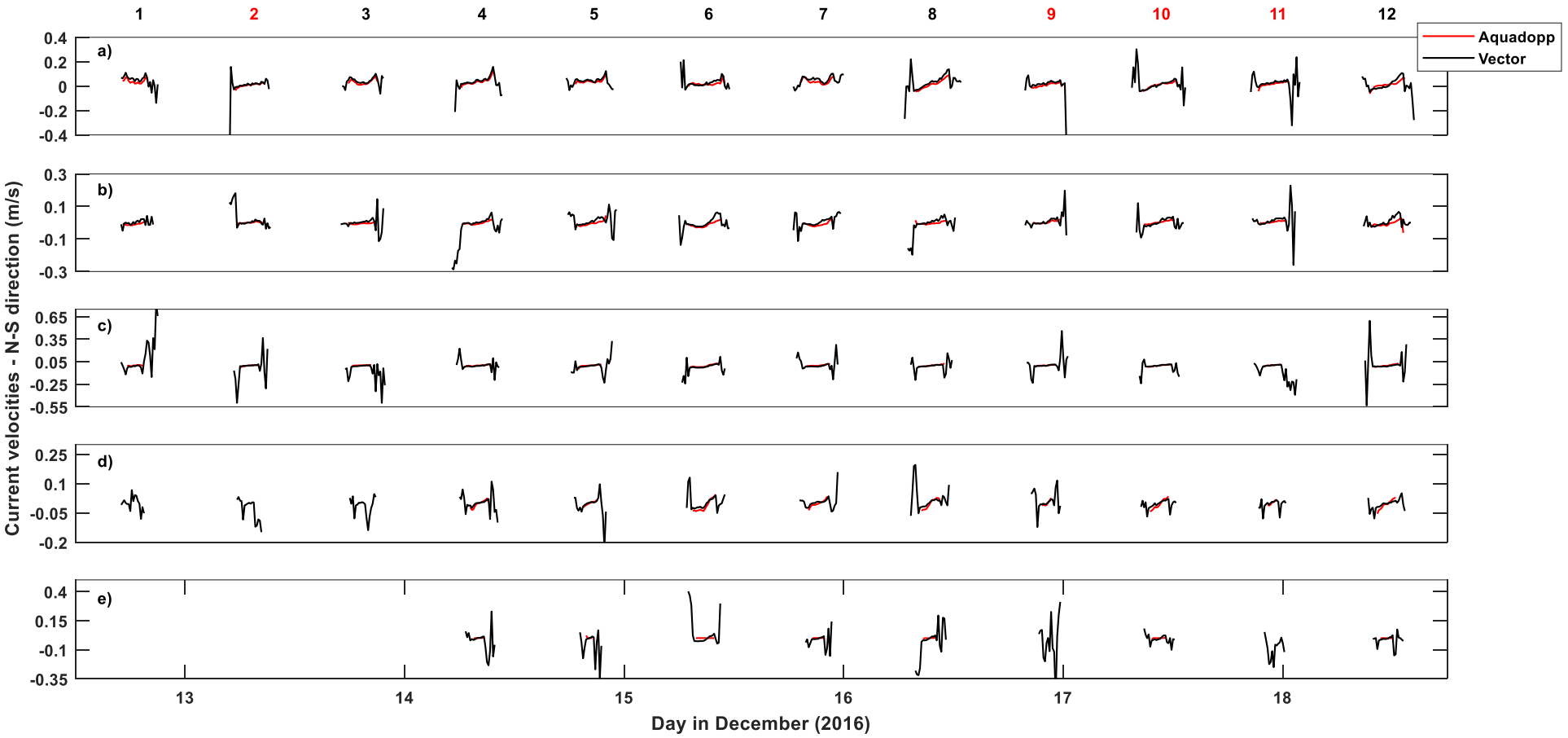

Figure 3.11: Burst-averaged N/S velocities from downward-facing Aquadopps at the point nearest the height above the bed of the Vectors (averaged over profile length, red lines) and Vectors (single point measurements, black lines) velocities (m/s) for sites 1 to 5 (a to e, respectively). Numbers above refer to tide number, referenced in the text. Red numbers = no wave conditions, black numbers = wave conditions.

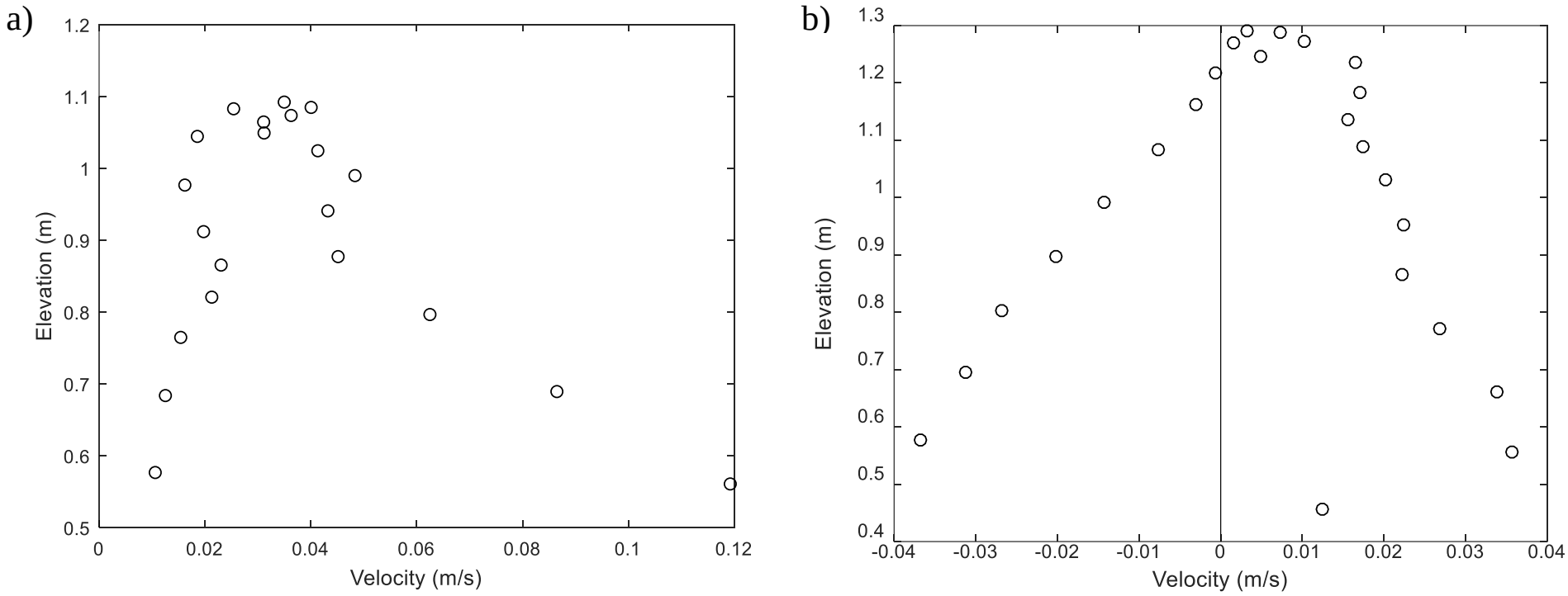

Figure 3.12: Tidal stage graphs showing N/S component of velocities at site 1 for a) tide 4 (waves) and b) tide 10 (no waves). Negative values correspond to flood dominant (southward) velocities and positive values correspond to (northward) or ebb dominant velocities.

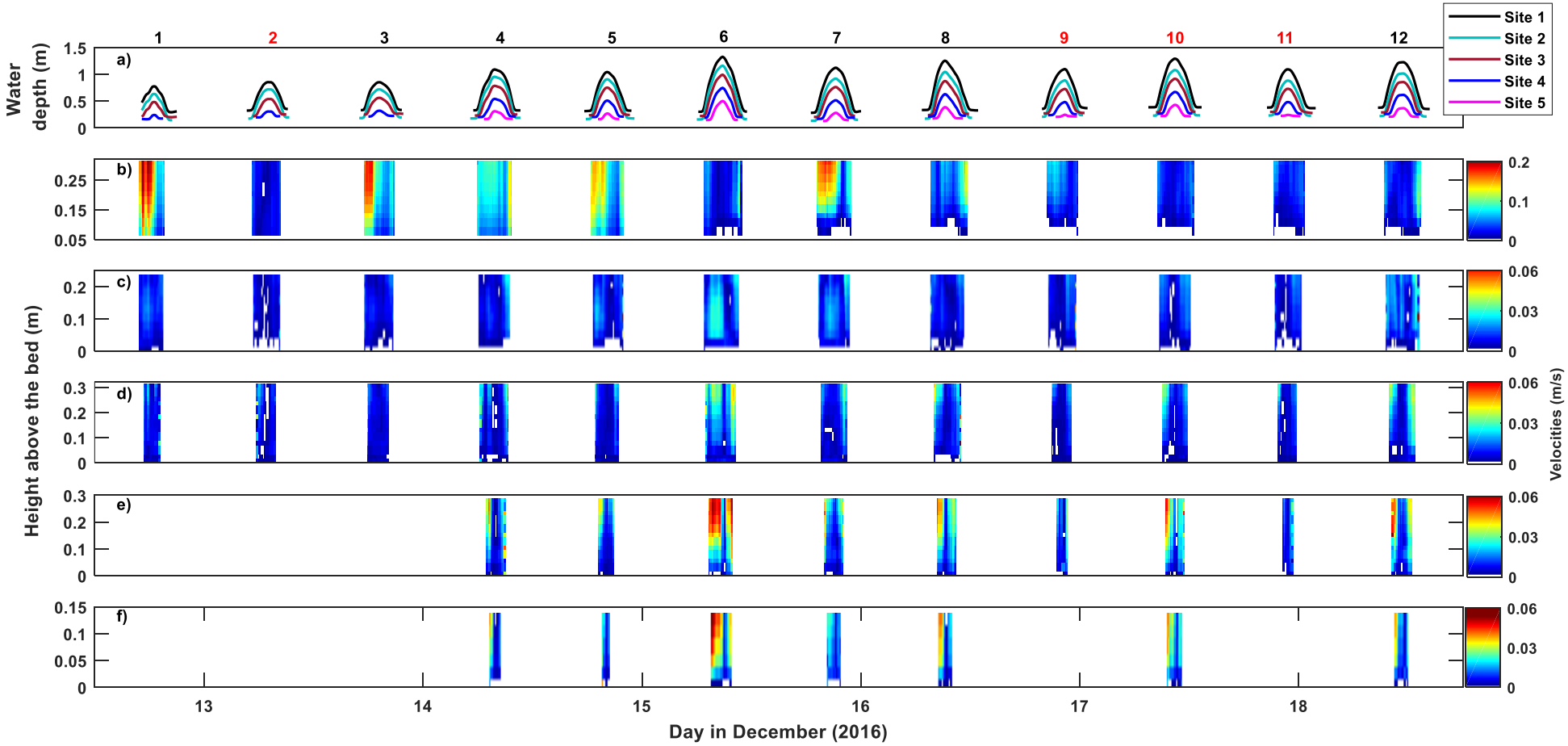

Figure 3.13: Water depths (a) and horizontal flow velocities (m/s) for sites 1 to 5 (b to f, respectively). Note different axes values. Numbers above refer to tide number, referenced in the text. Red numbers = no wave conditions, black numbers = wave conditions.

In summary, velocities over the five sites do not show a monotonic decrease with distance into the forest from the intertidal mudflat into the mangrove forest. Site 1 often had offshore dominant currents with some tides entirely offshore directed throughout. Further into the forest, the currents become increasingly flood dominant, and at site 5, all tides are flood dominant. The tidal flows are strongly modulated by wind-driven processes (i.e. waves) and the pattern of current velocities has important implications for sediment transport.

3.5 Suspended Sediment Concentration

SSC (mg/l) was observed at two heights above the bed in the water column (Table 3.3) and is plotted in Figure 3.14. For most tides, SSC at sites 1 and 2 generally exhibit a u-shaped pattern, indicating that there is more sediment in the water column early in the flood and later in the ebb tides (i.e. at low water depths) than at high-tide. However, this pattern is less pronounced at sites 3-5. In particular, at sites 4 and 5, maximum concentrations are most often observed around high tide. This u-shaped pattern also matches the current velocities (m/s), which were observed to be largest at the beginning of the flood and end of the ebb (Figures 3.6-3.10). SSC being in phase with current speed, possibly indicates resuspension of local sediments. Maximum SSC at site 1 coincided with periods of large H_s and $U_{sigbed,}$ during these times flow is directed offshore.

Table 3.3: Height above the bed of SSC measurements

Site	Upper OBS (m)	Lower OBS (m)
1	0.27	0.03
2	0.26	0.06
3	0.38	0.20
4	0.39	0.14
5	0.23	0.04

Near-bed values of SSC were greater than those measured at ~30 cm above the bed. In general sites 1 and 2 had similar concentrations. Overall site 1 had the greatest SSC near the bed over the course of the experiment with a mean of 1383 mg/l. The maximum SSC recorded at sites 1 and 2 over the entire experiment were 5736 mg/l and 5894 mg/l respectively. For the measurements recorded near the bed, mean SSC values decreased with distance into the forest (i.e. from site 1 to site 5),

whereas ~30 cm above the bed, mean SSC were greatest at site 2, followed by 3 then sites 1, 4 and 5 (Table 3.4).

Table 3.4: Maximum and mean SSC (mg/l) at sites 1-5 over the entire experimental duration.

Site	Max Upper (mg/l)	Max Lower (mg/l)	Mean Upper (mg/l)	Mean Lower (mg/l)
1	1455	5736	229	1383
2	1024	5894	358	999
3	985	2496	330	915
4	944	2772	198	788
5	900	2250	109	821

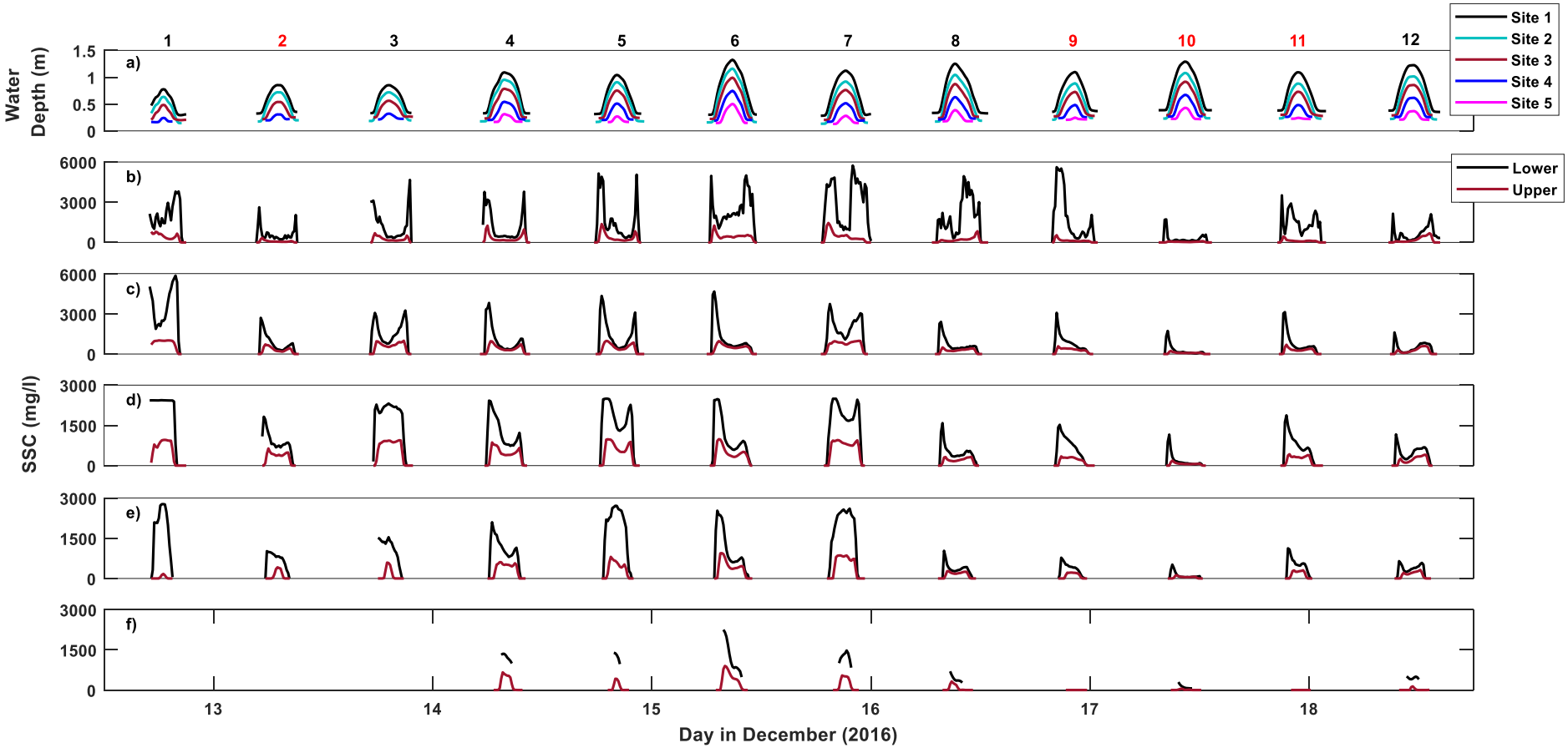

Figure 3.14. (a) Water depths and SSC (mg/l) from all sites (b-f correspond to sites 1 -5). In b-f, near-bed SSC are shown in black, and SSCs higher up in the water column are shown in red. Heights of measurements are given in Table 3.3. Numbers above refer to tide number, referenced in the text. Red numbers = no wave conditions, black numbers = wave conditions.

To observe the effects of waves more clearly on SSC at each site, SSC concentrations were split into the same categories as for the hydrodynamics, with tides with greater wave activity (defined as *Hs*>0.1 m) (tides 1 and 3-8 and 12) and those with low wave energy (H_s <0.1m) at site 1 on the mudflat.

3.5.1 SSC during calm periods

In Figures 3.15-3.19, SSC data from all sites are plotted as a function of time relative to high water and coloured by U_{sigbed}. SSC generally decreased during non-wavy periods, however, there are periods with large SSC but lower wave activity e.g. site 2 (Figure 3.16), however, these periods also don't correspond to times of high currents. In these cases, sediment may be transported into the region rather than locally resuspended.

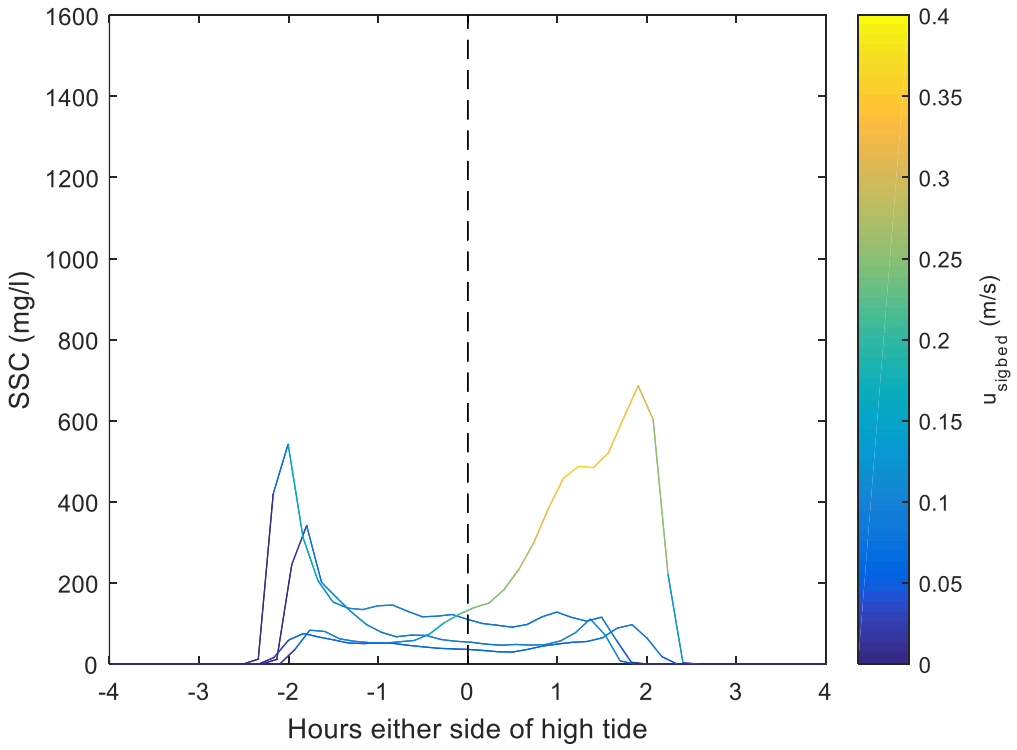

Figure 3.15: SSC (~30 cm above the bed) over days with less wave energy (*Hs* = 0.0445 m at site 1 for tides 2 and 9-11). Lines are coloured by the significant orbital velocities at the bed.

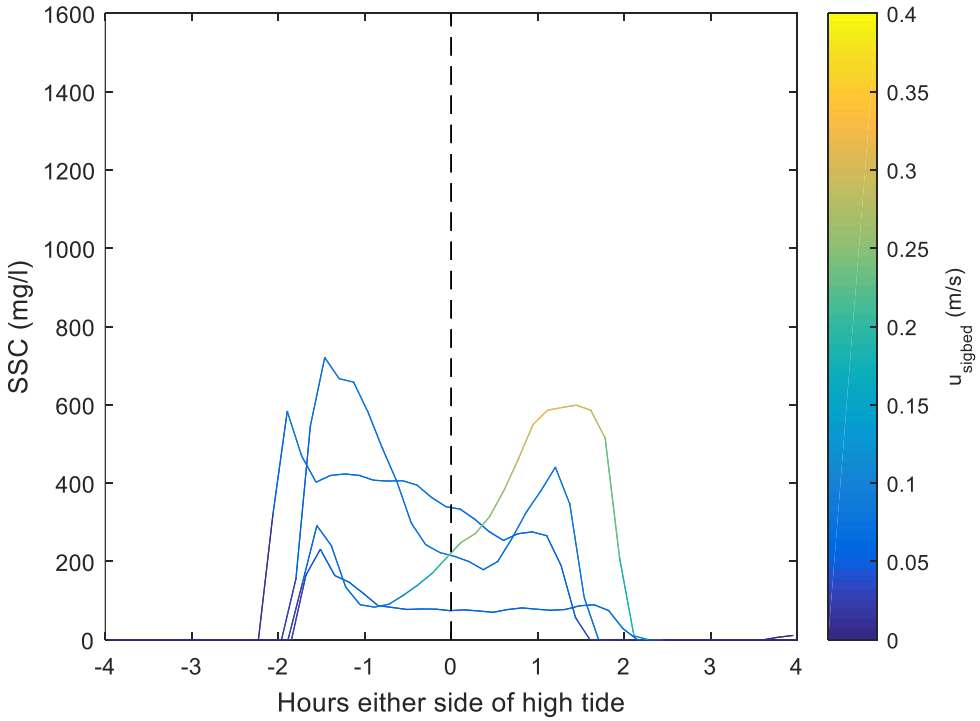

Figure 3.16: SSC (~30 cm above the bed) over days with less wave energy (*Hs* = 0.0243 m at site 2 for tides 2 and 9-11). Lines are coloured by the significant orbital velocities at the bed.

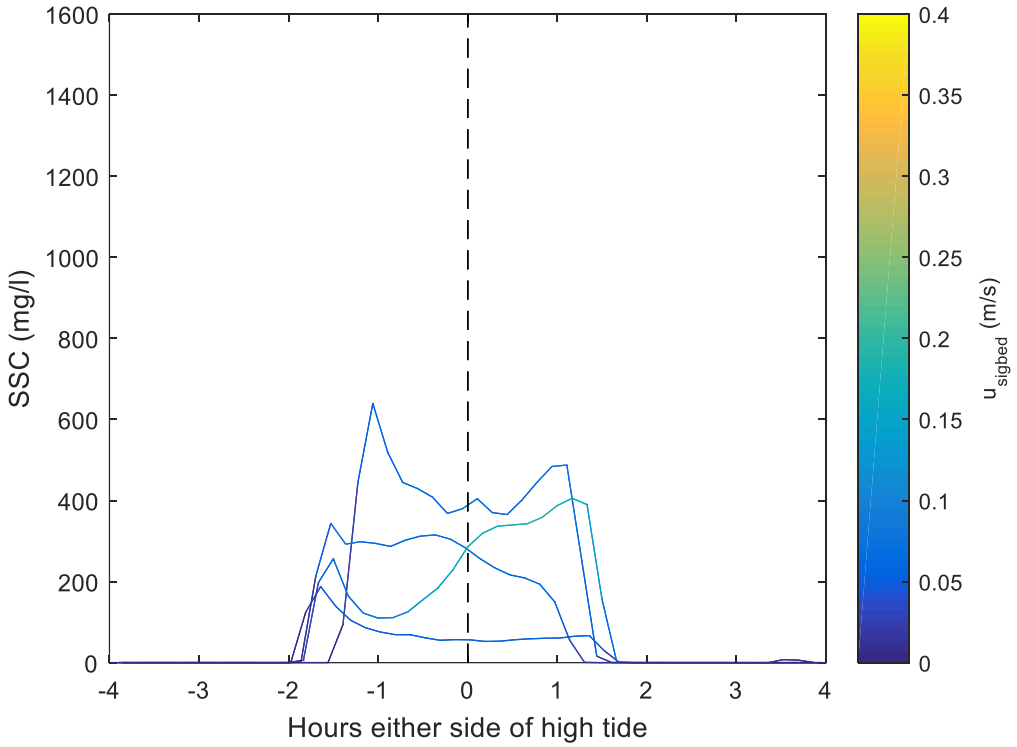

Figure 3.17: SSC (~30 cm above the bed) over days with less wave energy (*Hs* = 0.0226 m at site 3 for tides 2 and 9-11). Lines are coloured by the significant orbital velocities at the bed.

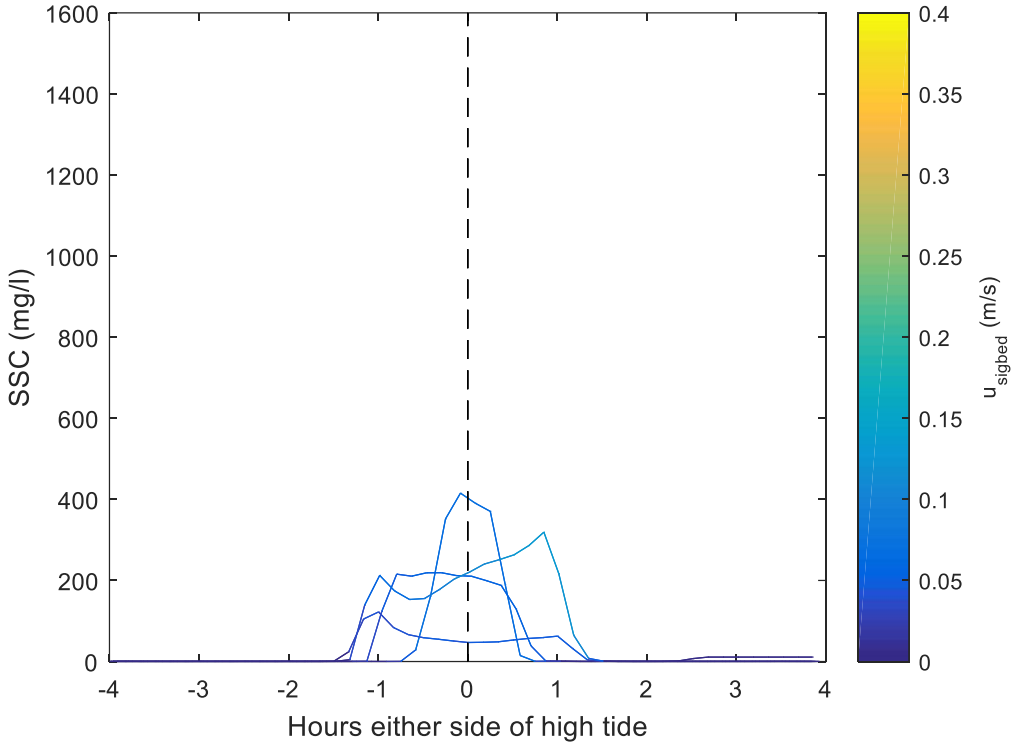

Figure 3.18: SSC (~30 cm above the bed) over days with less wave energy (*Hs* = 0.0159 m at site 4 for tides 2 and 9-11). Lines are coloured by the significant orbital velocities at the bed.

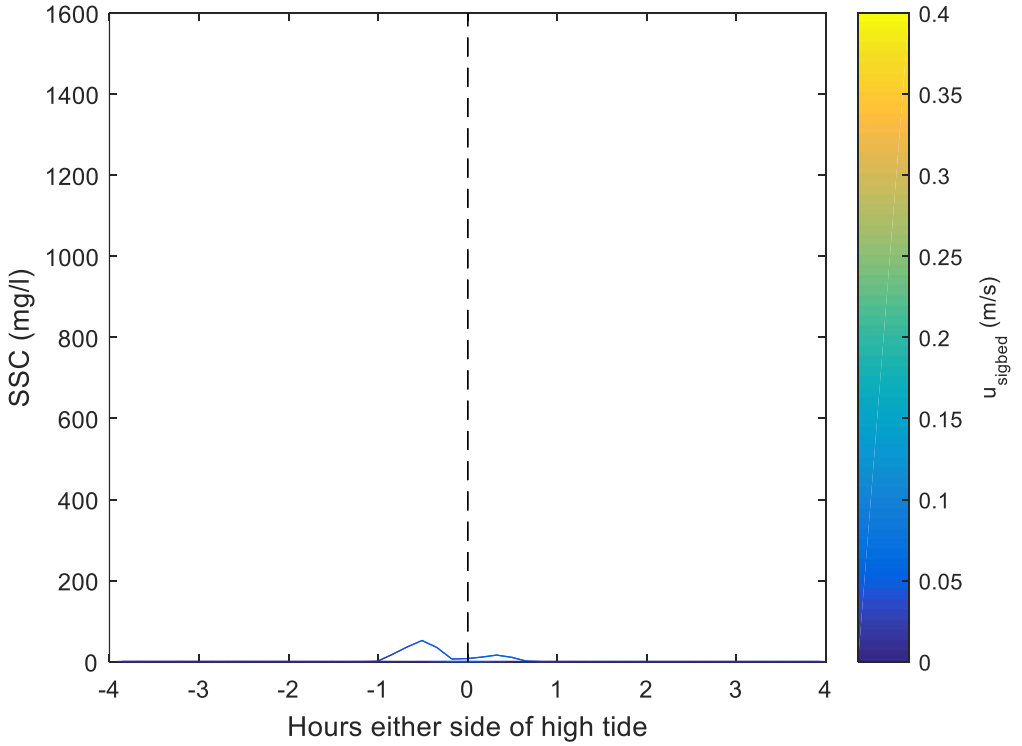

Figure 3.19: SSC (~30 cm above the bed) over days with less wave energy (*Hs* = 0.0079 m at site 5 for tides 2 and 9-11). Lines are coloured by the significant orbital velocities at the bed.

3.5.2 SSC during windy periods

Figures 3.20-3.24, show that overall, SSC were greater during the wavy periods, particularly at site 1 (Figure 3.20). At sites 3-5 during wavy periods (Figures 3.22-3.24), SSC is still relatively high despite small U_{sigbed} indicating advection of sediment as opposed to local resuspension by waves.

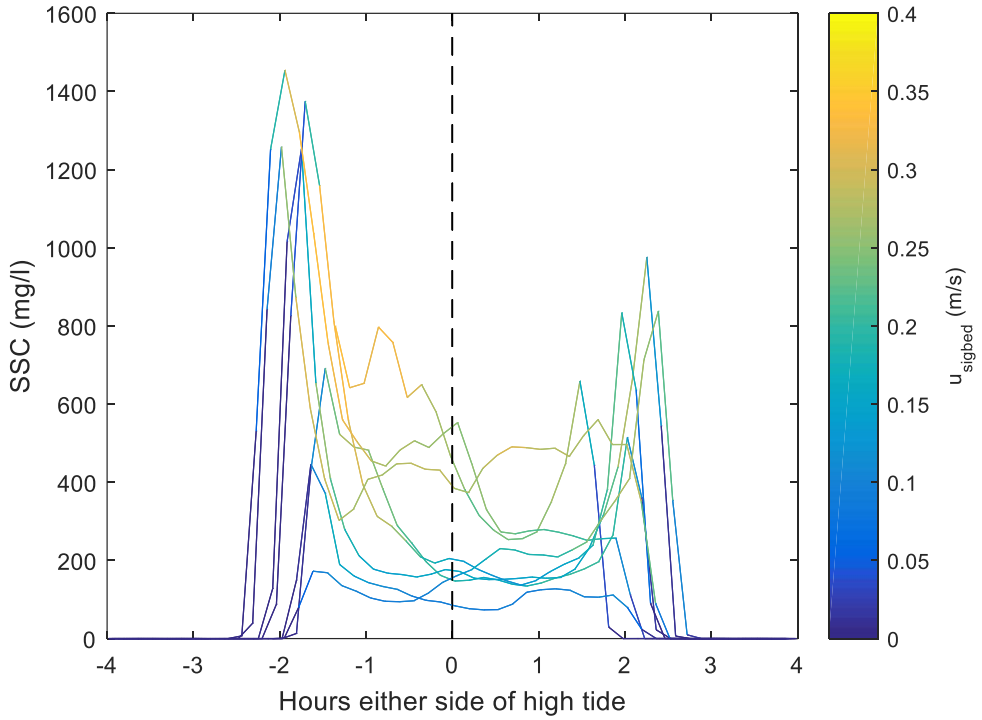

Figure 3.20: SSC (~30 cm above the bed) over days with greater wave energy (mean *Hs* = 0.1139 m at site 1 for tides 1 and 3-8 and 12). Lines are coloured by the significant orbital velocities at the bed.

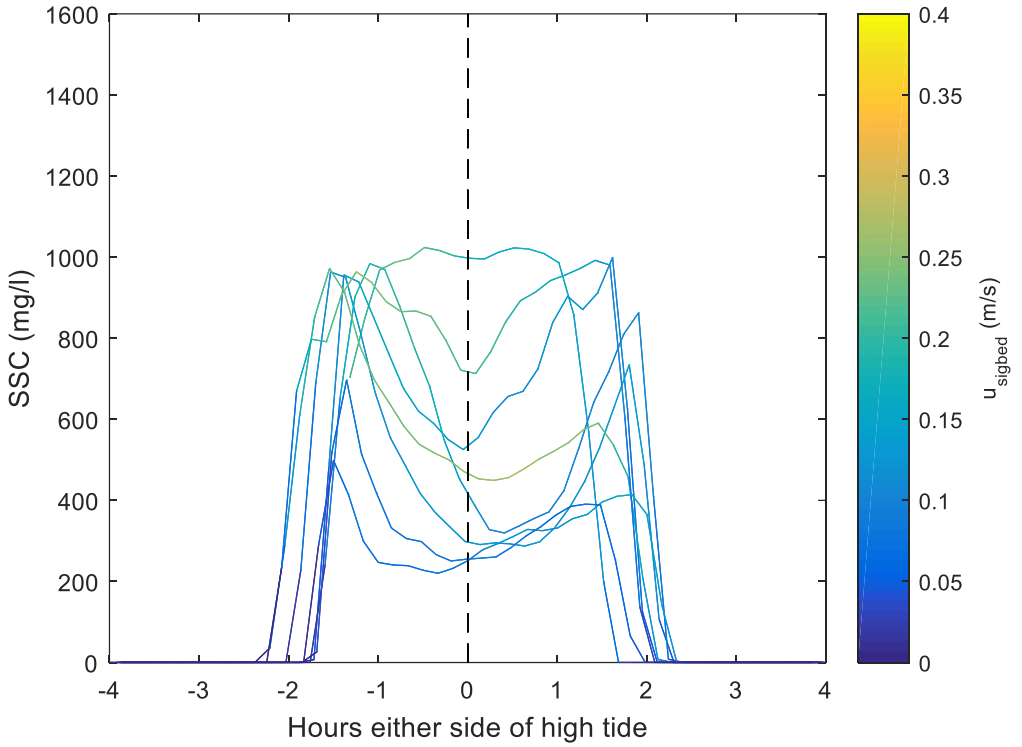

Figure 3.21: SSC (~30 cm above the bed) over days with greater wave energy (*Hs* = 0.0720 m at site 2 for tides 1 and 3-8 and 12). Lines are coloured by the significant orbital velocities at the bed.

.

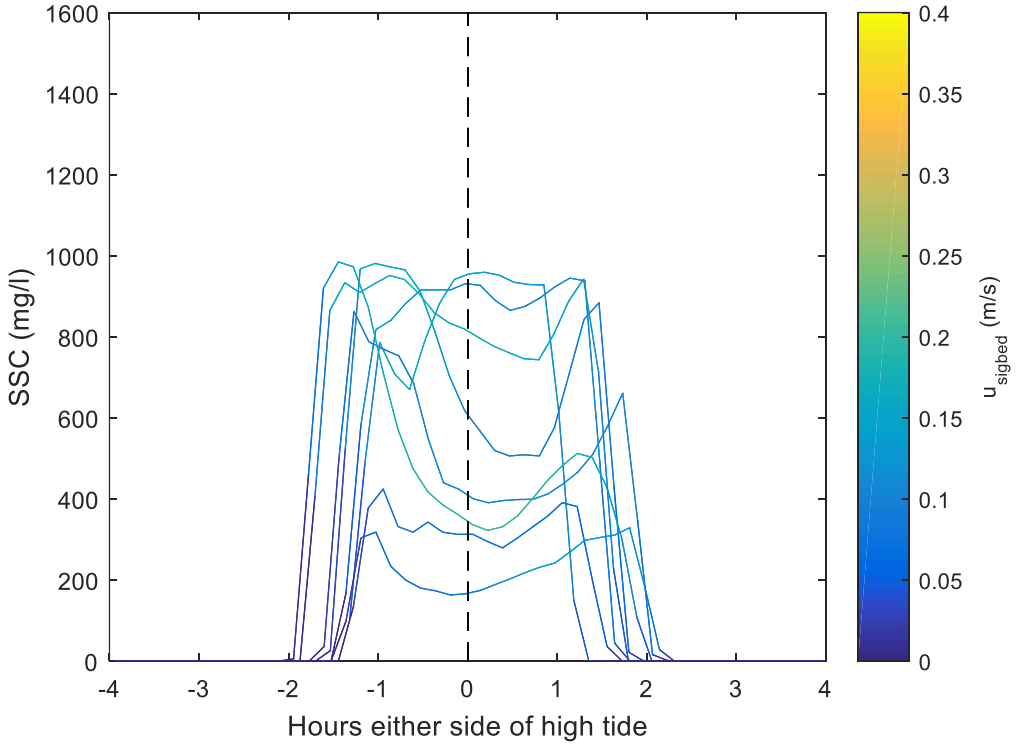

Figure 3.22: SSC (~30 cm above the bed) over days with greater wave energy (*Hs* = 0.0549 m at site 3 for tides 1 and 3-8 and 12). Lines are coloured by the significant orbital velocities at the bed.

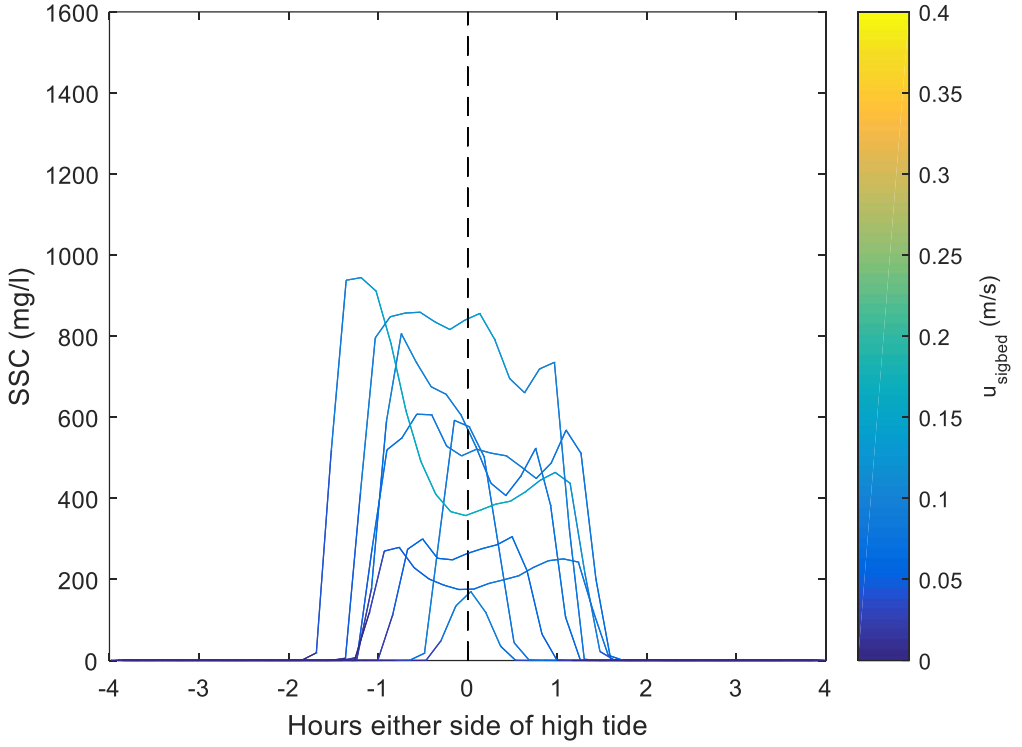

Figure 3.23: SSC (~30 cm above the bed) over days with greater wave energy (*Hs* = 0.0320 m at site 4 for tides 1 and 3-8 and 12). Lines are coloured by the significant orbital velocities at the bed.

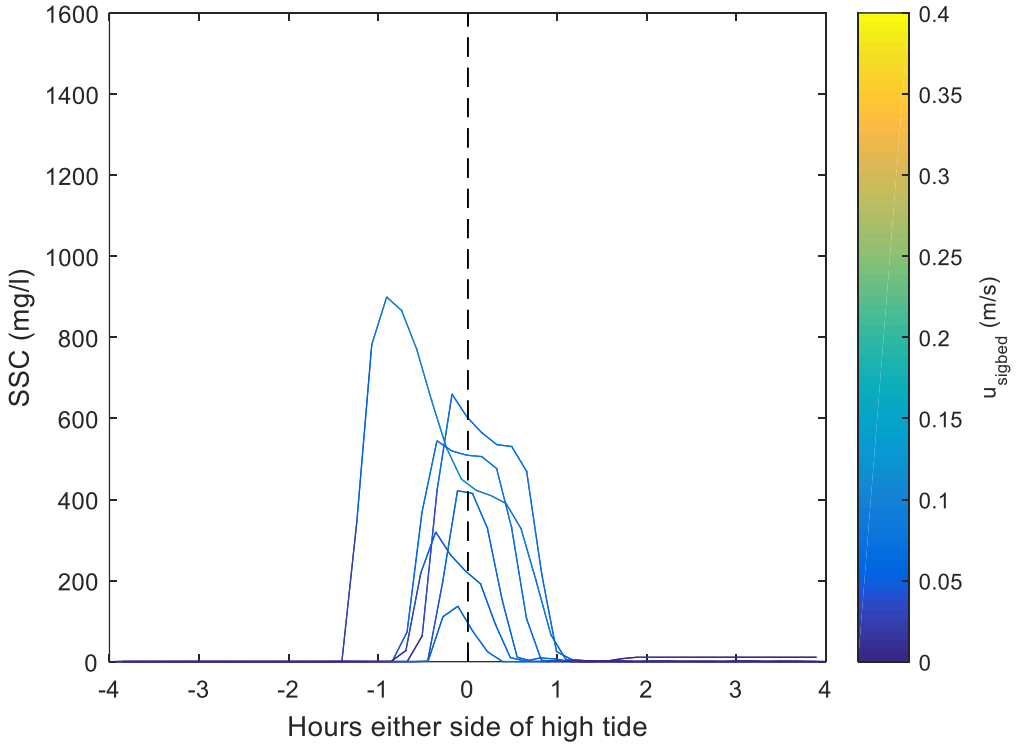

Figure 3.24: SSC (~30 cm above the bed) over days with greater wave energy (*Hs* = 0.0150 m at site 5 for tides 1 and 3-8 and 12). Lines are coloured by the significant orbital velocities at the bed.

3.6 Bed sediment grain size

Bed sediment grain size was analysed to determine if there was a change in particle size from site 1 to site 5. Figure 3.25 shows median grain sizes (d50) and indicates that there were no significant differences across the measurement transect. The maximum d50 was 9.83 µm at site 4 and the minimum, 6.17 µm at site 1. The mean d50 across 2 sets of sub-samples of all sites was 8 µm, which is classed as silt.

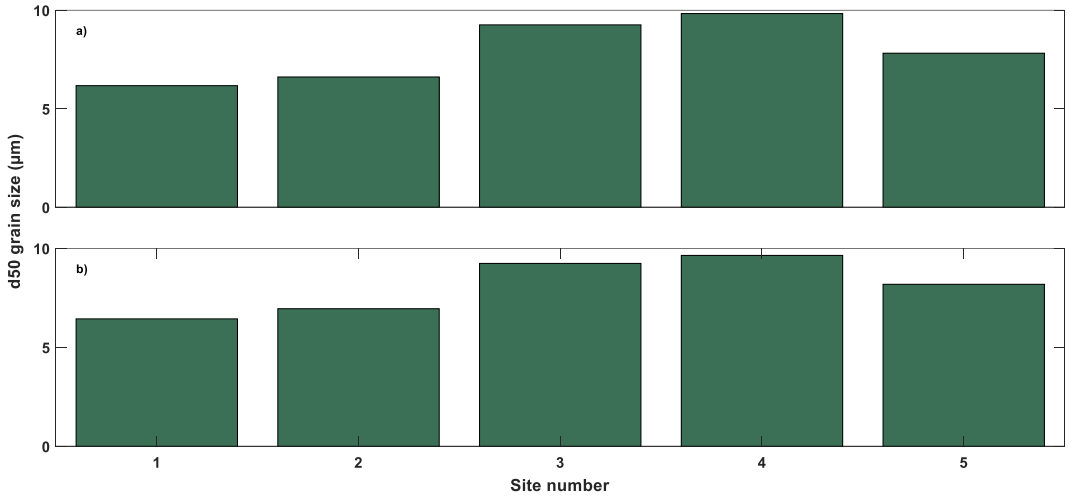

Figure 3.25: d50 (µm) of bed-sediment grain size at each measurement site in the Firth of Thames, a) sub-sample 1, b) sub-sample 2

3.7 Sediment transport

Figures 3.26-3.29 show example velocity, SSC and concentration velocity (v^*C) profiles from site 1 for four bursts during two tides. Figure 3.26 and Figure 3.27 show a high wave case during the flood and ebb phase of the tide (tide 4). Similarly, Figure 3.28 and Figure 3.29 show data measured during a tide characterised as low wave energy (tide 10). Tide 4 was chosen to analyse the model fits (described in section 2.4.3) further because it is one of the tides with N-S currents that were set in a constant offshore direction. Tide 10 was chosen as an example in which the current direction reversed. Figures 3.26-3.29 show that in general, the maximum contributions of SSC to sediment flux occurs within the first 0.1 m of the bed. Although SSC increase toward the bed, the contribution to the sediment flux tends to decrease as a result of a reduction in the flow speed in the near bed region. Conversely, although velocities higher in the water column are faster, concentrations are lower, hence contributions to the flux decreases with height

above the bed. During tide 4 both flood and ebb profiles show positive values of velocity and v^*C, indicating that currents and therefore sediment transport is directed offshore. In contrast, tide 10 shows opposing profiles, with negative values on the flood tide and positive values on the ebb, indicating onshore and offshore movement, respectively. The profiles show that the magnitude of v^*C are different with each model. However, the flux calculations from the different models were compared and they exhibit the same temporal pattern. For the rest of the analysis present in this thesis the constant diffusivity model (Eq. 2-6)) was used.

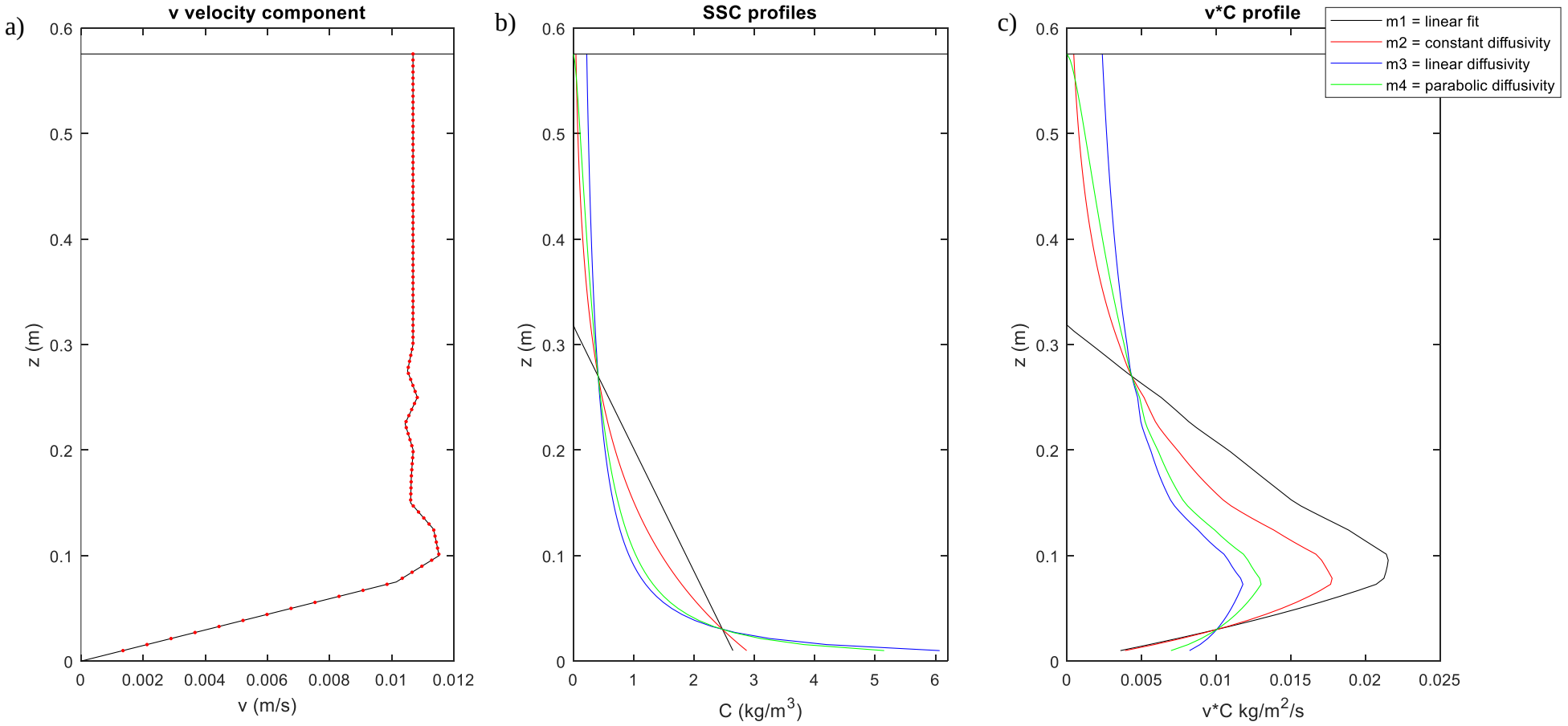

Figure 3.26: Burst-averaged profiles of (a) v velocity, (b) SSC and (c) *v*C* profiles for site 1. Data was taken from mid-flood tide during tide 4 which was characterised by northerly-directed v velocities throughout the tidal cycle. Colours indicate the four models used to fit the SSC data. SSC measurement heights were 0.27 m and 0.03 m (and are shown by the intersection of the four model fits in panel b).

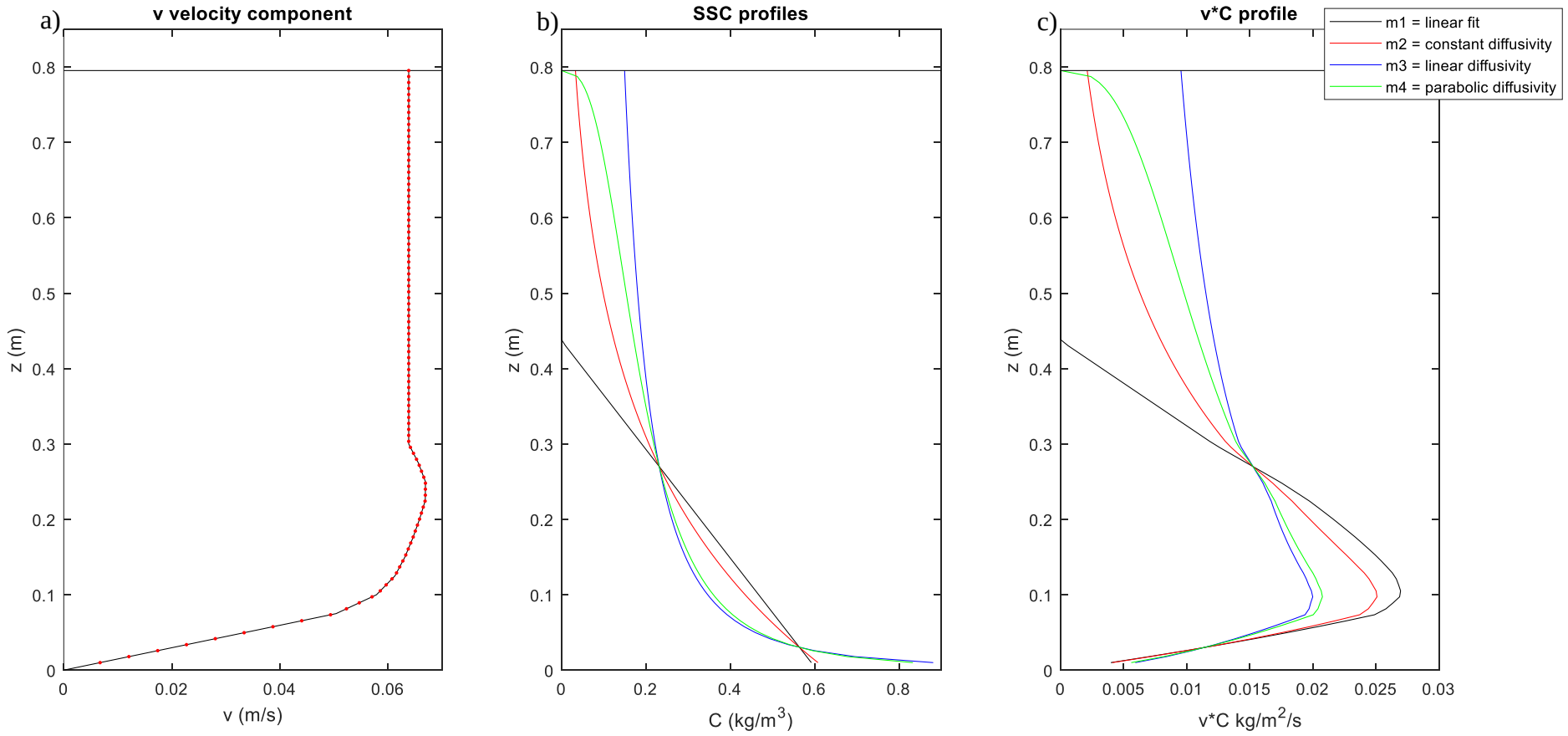

Figure 3.27: Burst-averaged profiles of (a) v velocity, (b) SSC and (c) *v*C* for site 1. Data was taken from mid-ebb tide during tide 4 which was characterised by northerly-directed v velocities throughout the tidal cycle. Colours indicate the four models used to fit the SSC data. SSC measurement heights were 0.27m and 0.03 m (and are shown by the intersection of the four model fits in panel b).

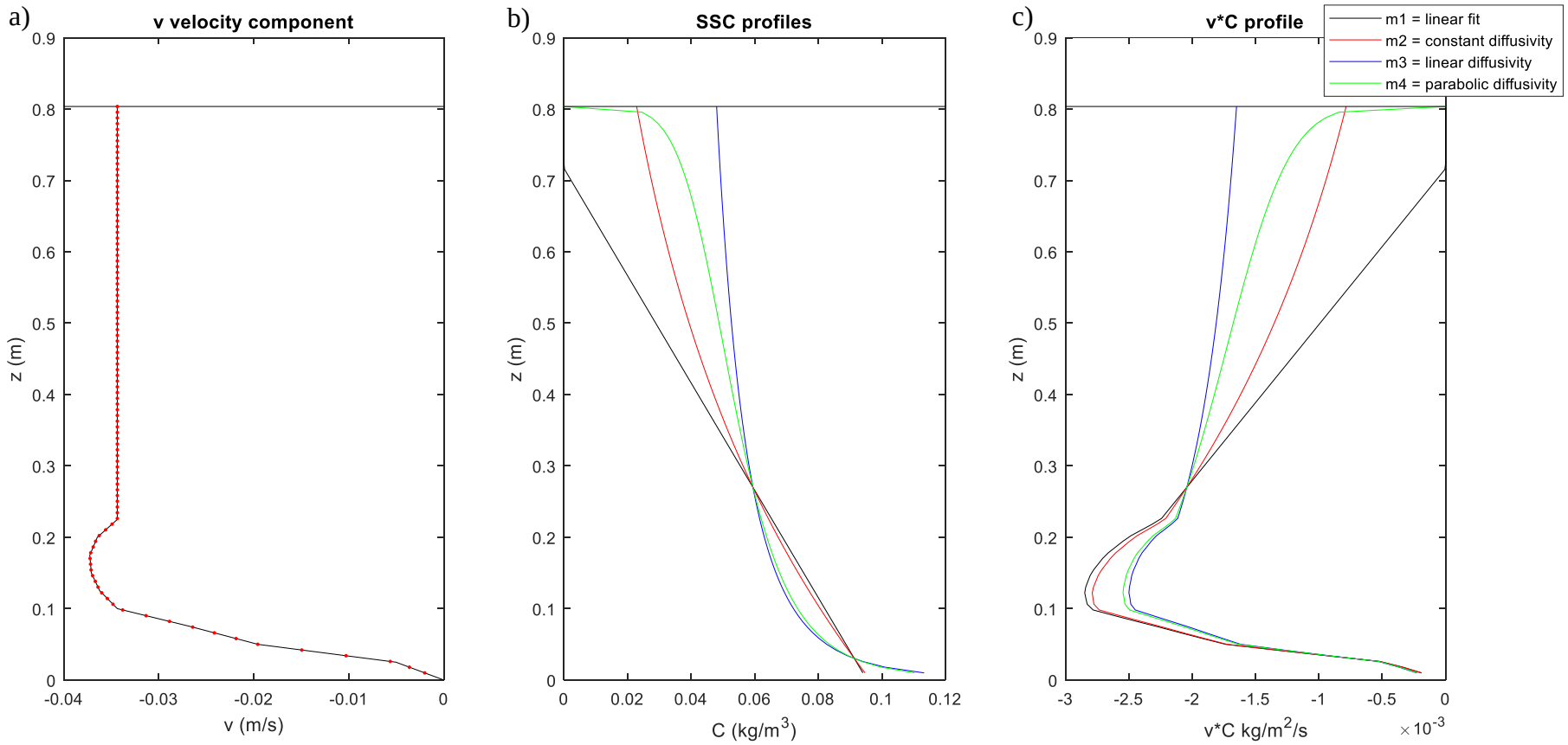

Figure 3.28: Burst-averaged profiles of (a) v velocity, (b) SSC and (c) *v*C* profiles for site 1. Data was taken from mid-flood tide during tide 10 which was characterised by northerly-directed v velocities throughout the tidal cycle. Colours indicate the four models used to fit the SSC data. SSC measurement heights were 0.27 m and 0.03 m (and are shown by the intersection of the four model fits in panel b).

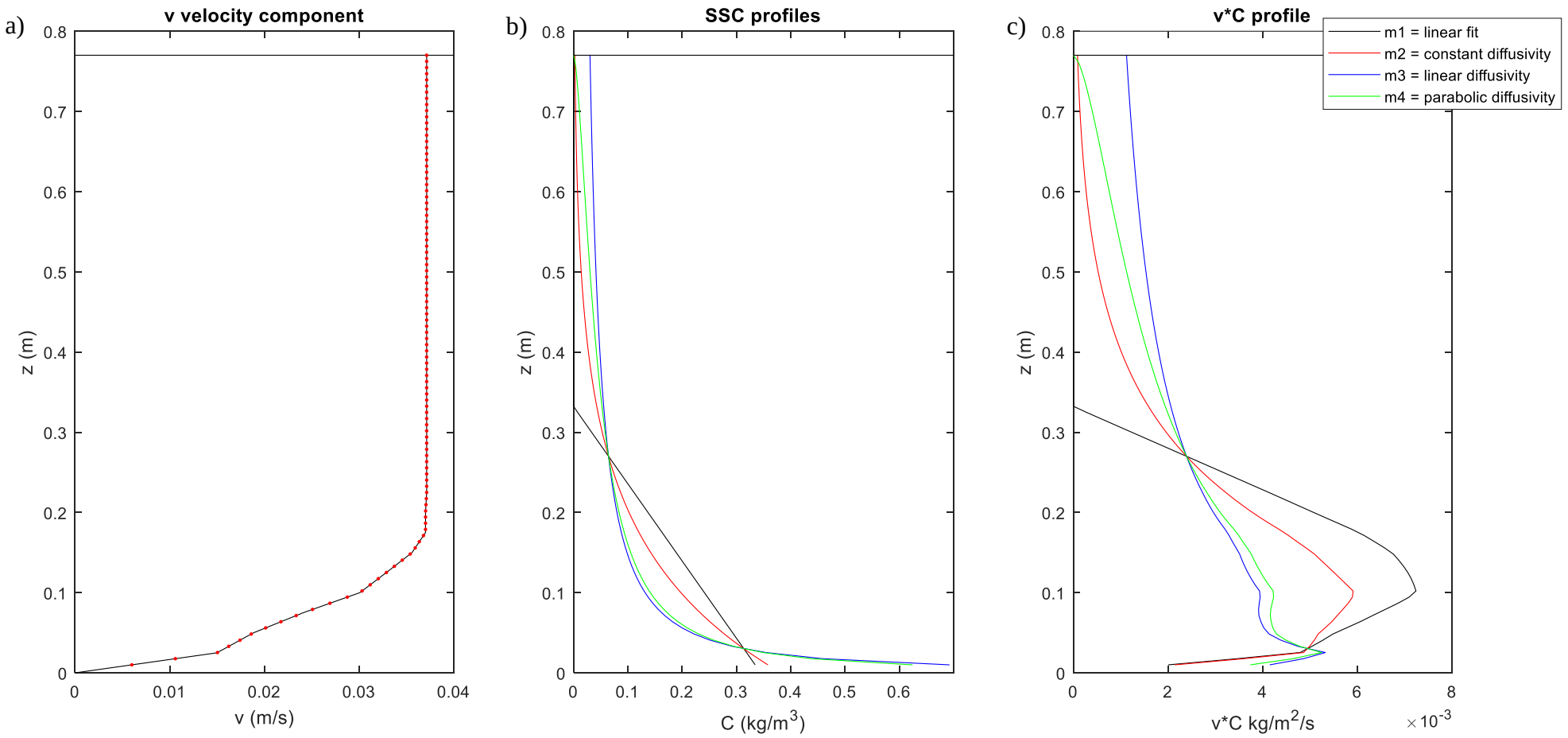

Figure 3.29: Burst-averaged profiles of (a) v velocity, (b) SSC and (c) *v*C* profiles for site 1. Data was taken from mid-ebb tide during tide 10 which was characterised by northerly-directed v velocities throughout the tidal cycle. Colours indicate the four models used to fit the SSC data. SSC measurement heights were 0.27 m and 0.03 m (and are shown by the intersection of the four model fits in panel b).

Differences across sites are easily discerned by considering Figure 3.30, which shows results for all sites combined. During the flood phase of tide 4, the v^*C at site 1 is directed in the opposite direction (offshore) to the other sites at which the v^*C is directed onshore (except for a small portion of the profile near the bed at site 3); whereas during ebb, all sediment transport is directed offshore. For tide 10, all sites have onshore and offshore directed v^*C during the flooding and ebbing tide, respectively. Figure 3.31-3.35 show time-series of depth-averaged N-S current velocities and sediment flux data at each of the five sites. All show that the sediment fluxes are closely related to the current velocities, with larger fluxes for faster flow speeds. Figure 3.31 shows that at site 1, both the current velocities and sediment fluxes are mainly directed offshore for the majority of the time. From site 2 and into the forest (Figures 3.32-3.35), the time-series show onshore and offshore directed sediment fluxes that occur during flood and ebb tides, respectively.

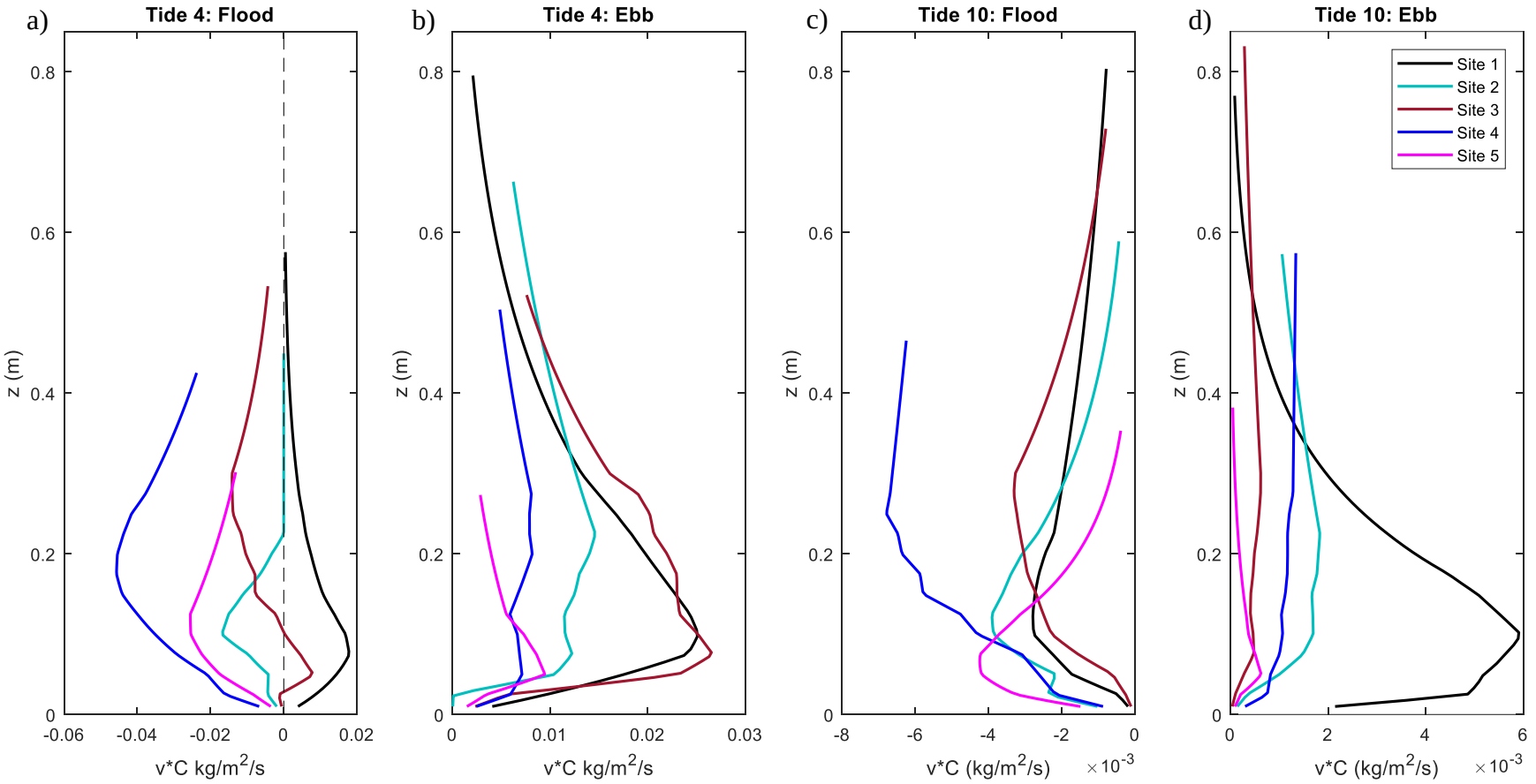

Figure 3.30: *v*C* profiles for all sites at selected times during two different tides: tide 4 characterised by larger wave energy and tide 10 characterised by smaller wave energy. a) Mid-flood of tide 4, b) mid-ebb of tide 4, c) mid-flood of tide 10, d) mid-ebb of tide 10.

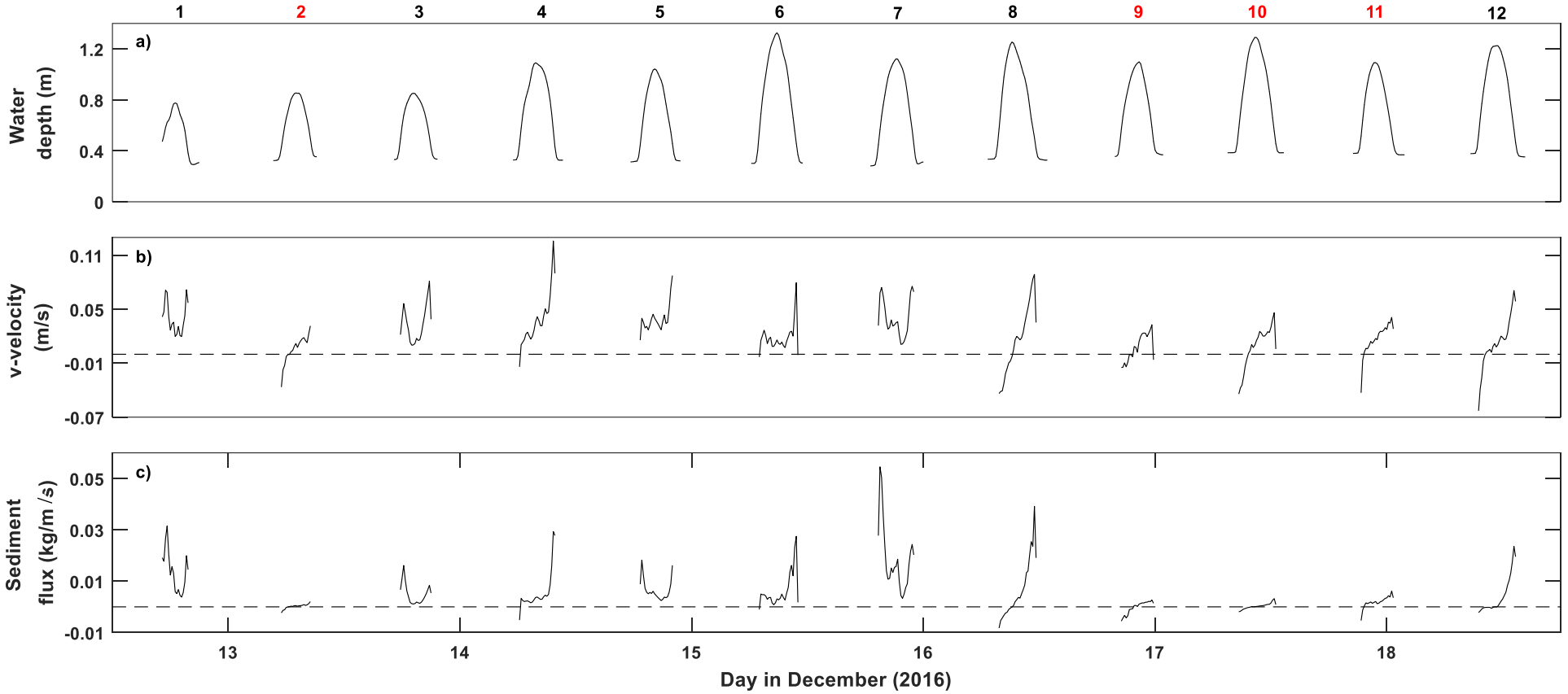

Figure 3.31: Time series of (a) water depths, (b) N-S velocities and (c) sediment fluxes (kg/m/s) at site 1. Dashed lines show 0 values. Numbers above refer to tide number, referenced in the text. Red numbers = no wave conditions, black numbers = wave conditions.

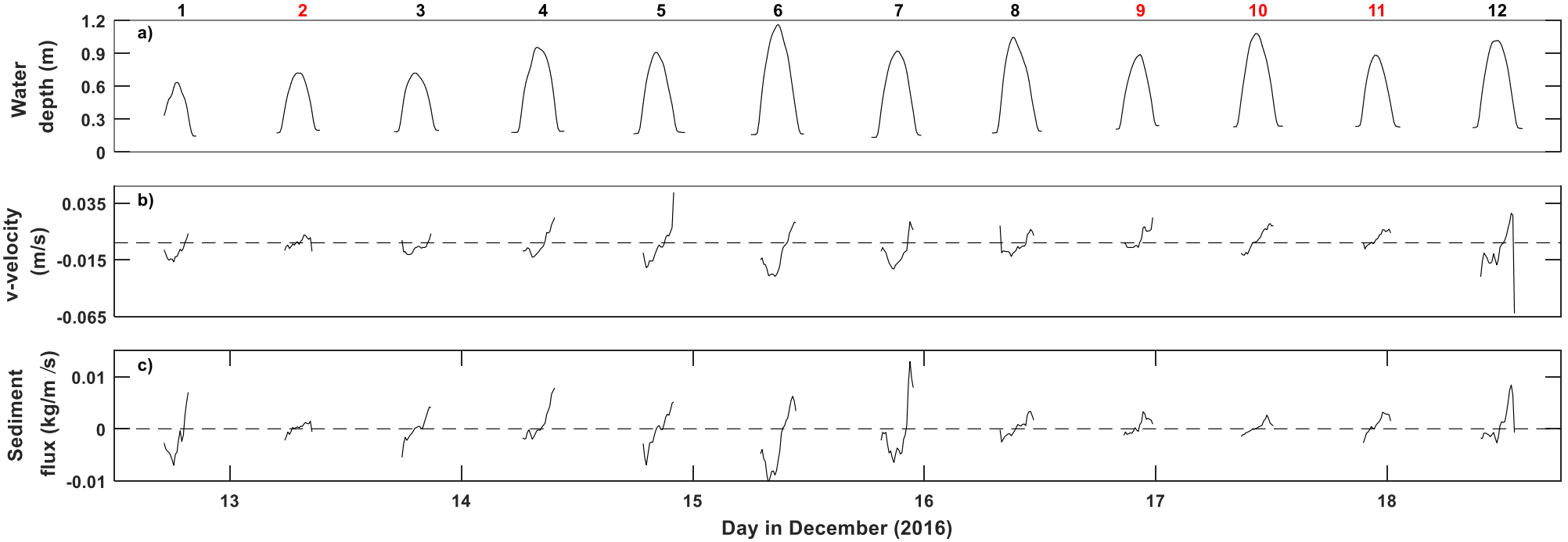

Figure 3.32: Time series of (a) water depths, (b) N-S velocities and (c) sediment fluxes (kg/m/s) at site 2. Dashed lines show 0 values. Numbers above refer to tide number, referenced in the text. Red numbers = no wave conditions, black numbers = wave conditions.

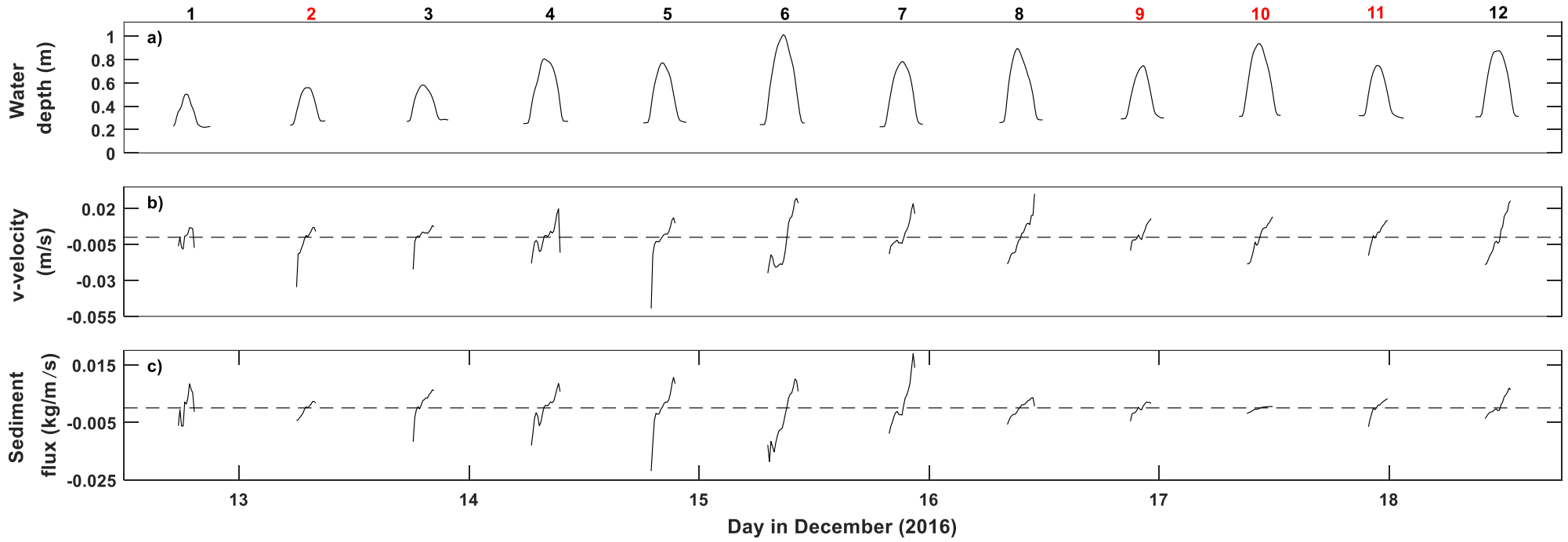

Figure 3.33: Time series of (a) water depths, (b) N-S velocities and (c) sediment fluxes (kg/m/s) at site 3. Dashed lines show 0 values. Numbers above refer to tide number, referenced in the text. Red numbers = no wave conditions, black numbers = wave conditions.

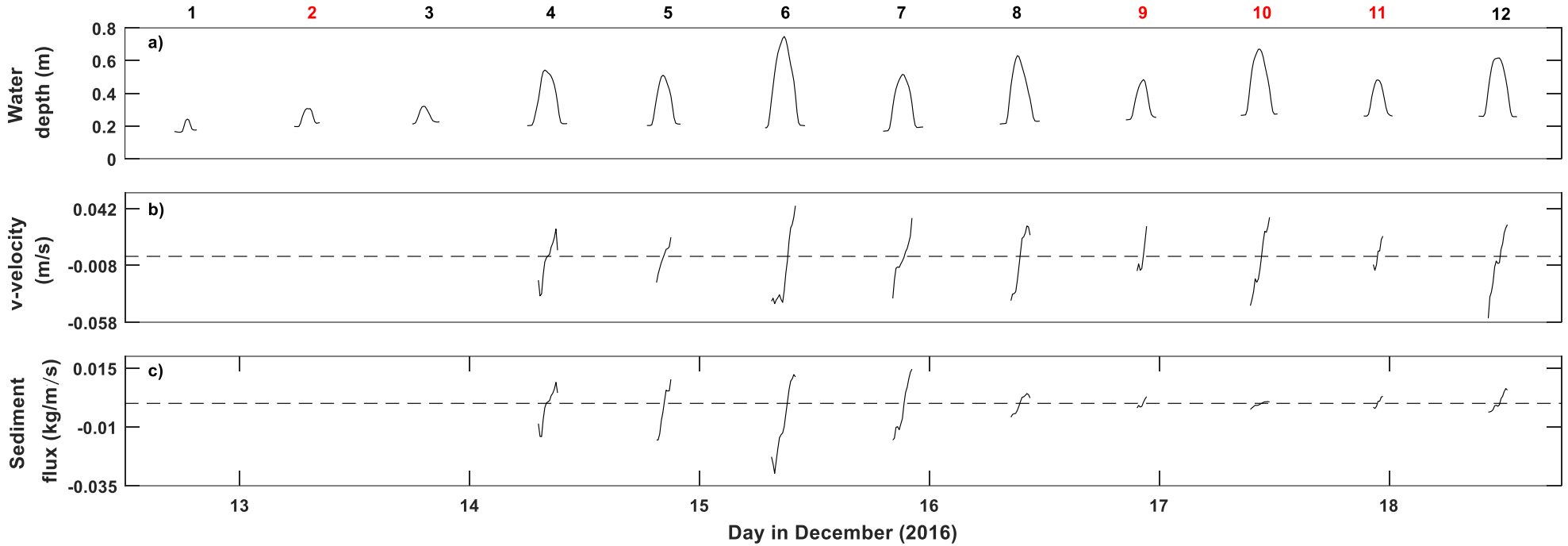

Figure 3.34: Time series of (a) water depths, (b) N-S velocities and (c) sediment fluxes (kg/m/s) at site 4. Dashed lines show 0 values. Numbers above refer to tide number, referenced in the text. Red numbers = no wave conditions, black numbers = wave conditions.

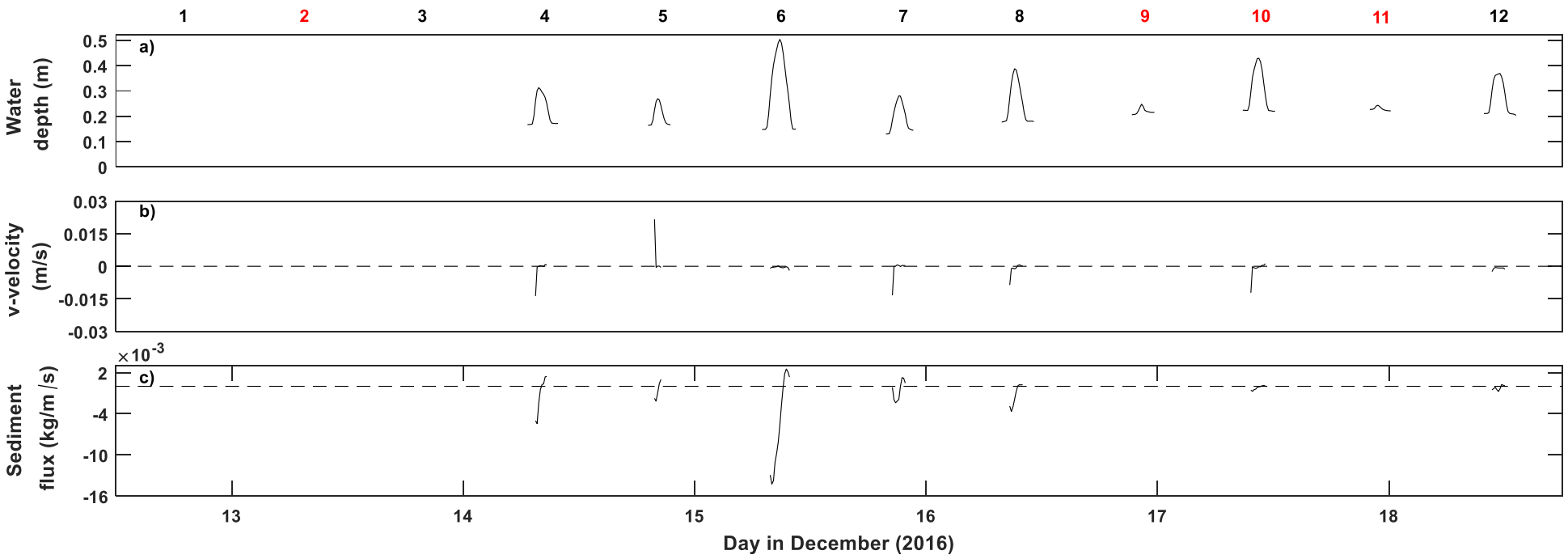

Figure 3.35: Time series of (a) water depths, (b) N-S velocities and (c) sediment fluxes (kg/m/s) at site 5. Dashed lines show 0 values. Numbers above refer to tide number, referenced in the text. Red numbers = no wave conditions, black numbers = wave conditions.

3.8 Flocculation

There are inherent difficulties in acquiring in-situ measurements of particle size in coastal environments: it is hard to deploy instrumentation without disturbing the environment or destroying the flocs, and conditions are often highly variable over both space and time, so finding a single set of camera settings suitable to obtain images over such a range of conditions is often not possible, often like with other optical instruments, the SSC is just too high. In the present experiment, problems arising from disturbing the environment were minimised with the use of a boardwalk. However, variable conditions were hard to control for, therefore, photos were often overexposed or too dark. However, usable images were obtained from sites 1 and 3 over two tides (9 and 11) allowing for preliminary qualitative analysis of flocs to be conducted. Quantity and size of flocs were categorised over each 10-minute burst by visual inspection. Size categories were determined as small, medium and large (Figure 3.36). Each size class was then assigned a number based on the quantity in each burst. Each image was analysed for quantity, with 0 corresponding to none, followed by (1) few ≤10 flocs, (2) some ≤30 flocs and (3) many >30 flocs and the overall value was averaged over the burst. Results of the floc analysis are shown in Figures 3.37 and 3.38. For tide 9, on the mudflat (site 1), larger numbers of flocs were present early in the tide but the majority of flocs were ‘small’. Around high-tide, numbers of all sizes decreased; however, during the ebb phase, the number of flocs appeared relatively consistent across all size classes. Inside the forest, fewer large flocs were identified, with predominantly smaller flocs present on flood tide, but during ebb tide, the number of large flocs increased (as with site 1). At site 1, there was a decrease in the overall number of flocs at high tide during both tide 9 and 11, in comparison to site 3 where floc numbers remained constant throughout most of the tide.

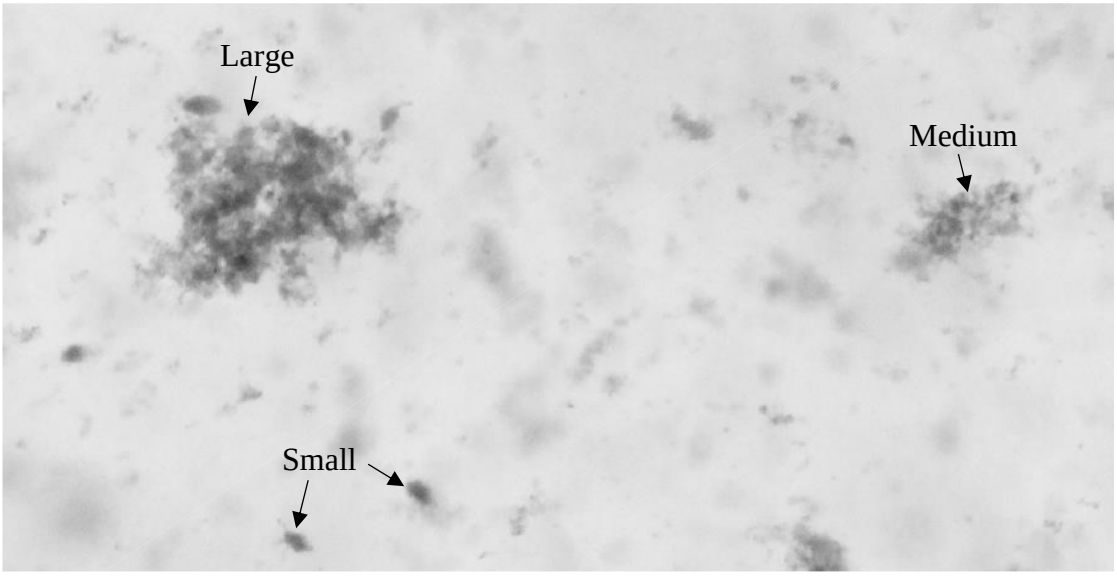

Figure 3.36: Example of qualitative size classes for analysing flocs, based on a visual analysis of two tides (9 and 11) at two different sites (1 and 3). Large = ~350 µm, medium = ~150 µm and small = ~20 µm.

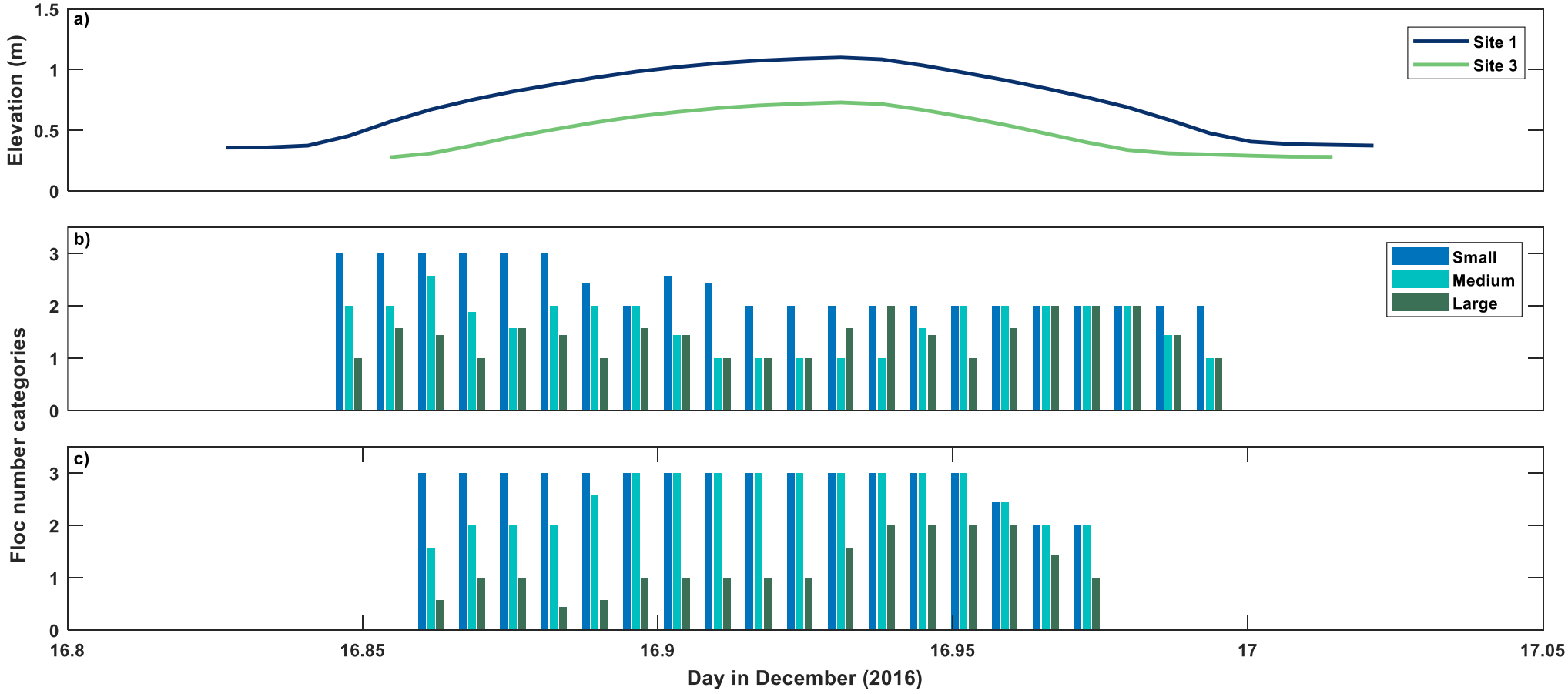

Figure 3.37: Floc analysis using qualitative analysis for tide 9. a) water depths at sites 1 (blue) and 3 (green), b) bar graph showing the number of flocs of each size in each burst at site 1, c) shows the same data for site 3. Y-axis categories correspond to no flocs (0), few (1), some (2), many (3). See text for details.

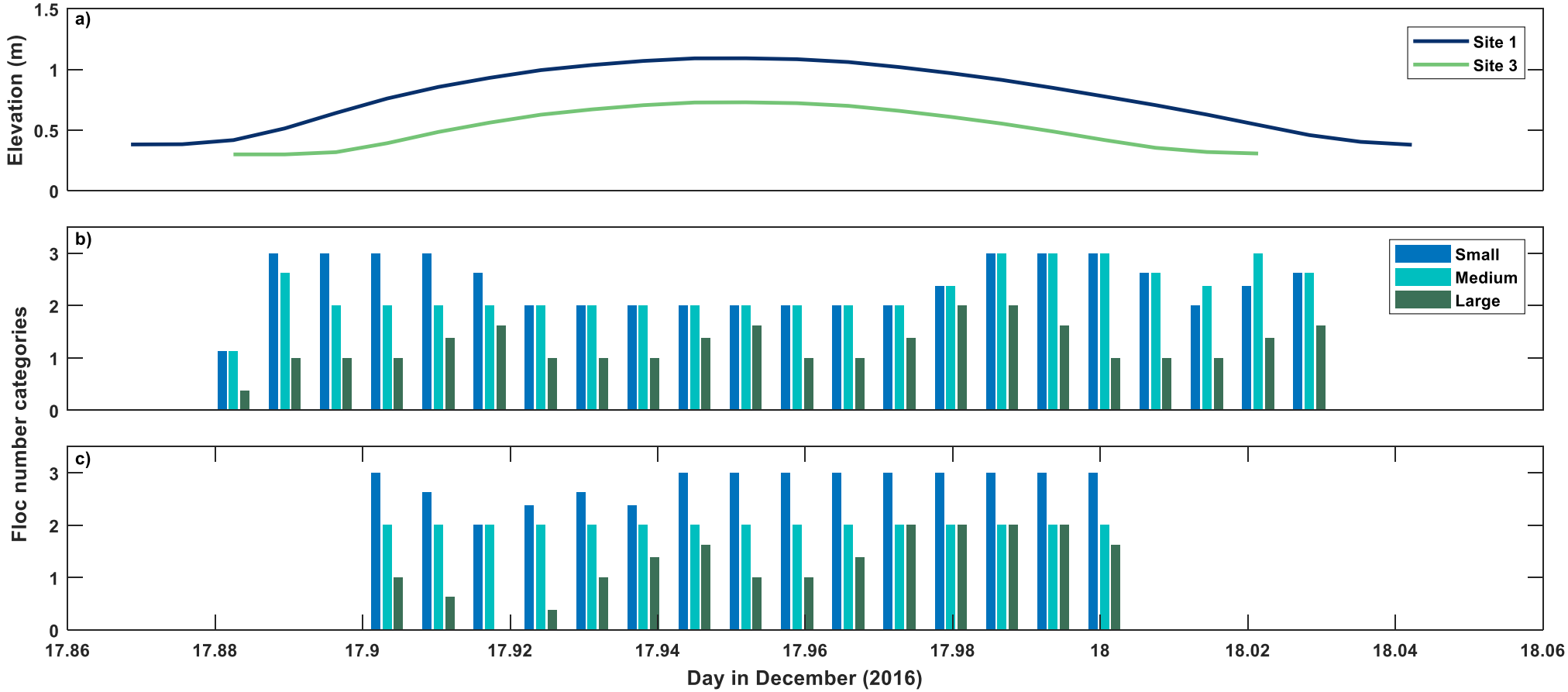

Figure 3.38: Floc analysis using qualitative analysis for tide 11. a) water depths at sites 1 (blue) and 3 (green), b) bar graph showing the number of flocs of each size in each burst at site 1, c) shows the same data for site 3. Y-axis categories correspond to no flocs (0), few (1), some (2), many (3). See text for details.

3.9 Summary

The results indicate that current velocities at site 1 can be entirely offshore-directed throughout some of the tides, and ebb dominant for all the other tides. Winds directed from the north and west are correlated with increased U_{sigbed} and offshore directed currents. The fetch for winds from the west is not very large and would not be expected to cause large waves and therefore the waves during tides that correspond to a westerly wind, are possibly coming from outside of the Firth of Thames. Northerly winds have a large fetch and would be expected to create the largest waves. Associated with the offshore oriented currents, is a significant net flux of sediment in the same direction. Site 1 has a net offshore flux for every tide whereas all the other sites vary as to whether they are onshore or offshore, but tend to mainly be onshore, as summarised per tide in Figure 3.39. Figure 3.40, shows the cumulative flux over the duration of the experiment. All sites, except site 1, have a net onshore flux. The flux at site 1 is much greater than at the other sites at about 849 kg/m over approximately 6 days. Total flux onshore at the other sites were 27.2 kg/m, 2.56 kg/m, 113.3 kg/m and 57.5 kg/m over the 6 days for sites 2-5, respectively. SSC is elevated, particularly near the bed and at sites 1 and 2. There is a gradient in mean SSC in the lower water column from site 1 which has the greatest volume concentration (1383 mg/l) to site 5 with the least (821 mg/l). Flocculation analysis indicates larger flocs occur on the ebb tide and that in general site 1 had a larger number of big flocs than site 3 in the forest.

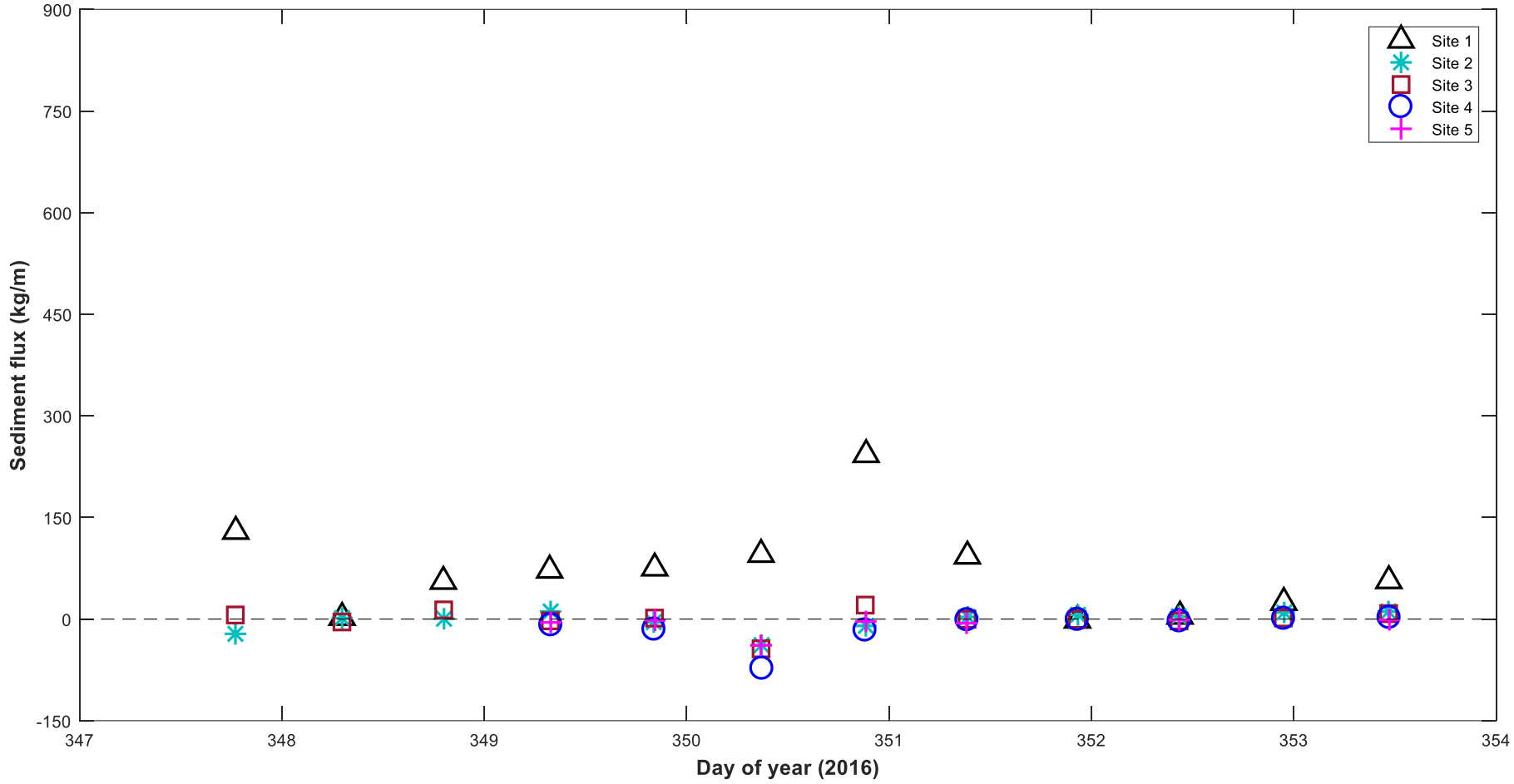

Figure 3.39: Total sediment flux (kg/m^2) for each tide at all sites.

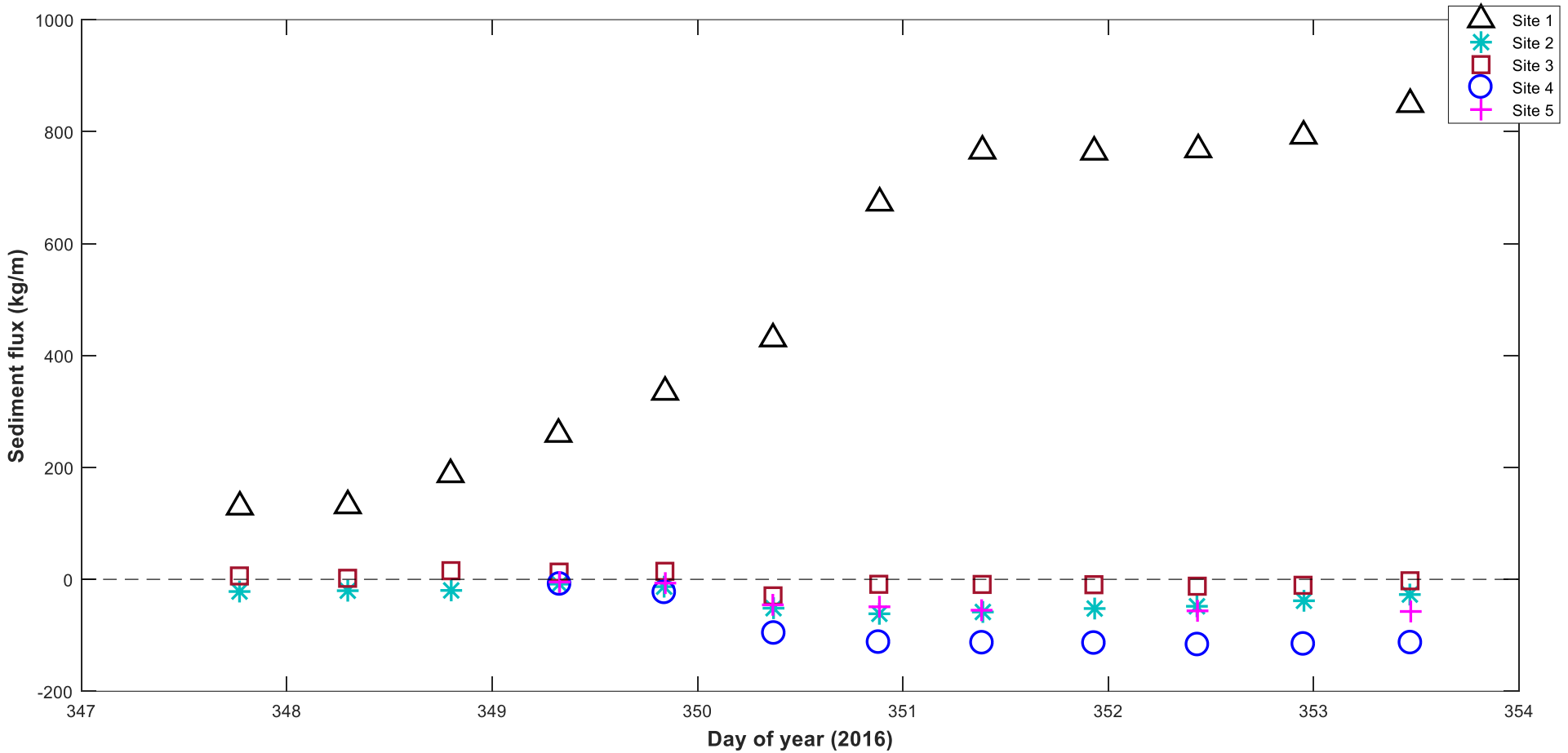

Figure 3.40: Cumulative sediment fluxes (kg/m) over the experiment for all sites

Chapter 4

Discussion

Current velocities were expected to decrease monotonically with distance into the forest while the flood dominance of the currents was expected to become more prominent, as has been observed in other mangrove systems. For example, Bryan *et al.* (2017) observed these effects in a numerical model of two contrasting sites at Cù Lao Dung within the Mekong Delta in Vietnam. While the authors' field observations supported the model, the change to flood dominant currents was not as clear in their field experiment, as in the modelled data. Results show that the current velocities in the Firth of Thames field site, do not decrease monotonically into the forest either for N-S or E-W components of velocity (Figures 3.6-3.10). Horizontal flow speed also shows a non-linear pattern, with slowest flow speeds observed at sites 2 and 3 (Figure 3.13), corresponding to the front of the fringe (site 2) and just inside the main forest (site 3) (Figure 2.2). Strong drag forces act in the fringe area to significantly slow the flow. A rotation of the currents occur, with the E-W component of the current diminishing slightly into the forest, so that flow direction is turning toward being fringe-perpendicular. However, the currents do not reach a completely N-S direction and are closer to being NE-SW oriented. Similar changes in flow direction, to fringe-perpendicular in the forest, were also observed in the Mekong Delta mangroves by Mullarney *et al.* (2017b) and in a creek-incised mangrove system in Thailand by Horstman *et al.* (2013). Increases in flow speeds at sites 4 and 5 may be due to the local heterogeneity of the vegetation and presence of runnels causing flow steering. Flood dominance occurs in many intertidal systems whether vegetated or not, because of a lag in maximum ebb and flood currents creating an asymmetry that results in the upper reaches always being flood dominant (Bryan *et al.*, 2017; Hunt *et al.*, 2016). The southern Firth of Thames system does become flood dominant into the forest, but on the intertidal flat just outside of the forest at site 1, the flows are strongly ebb-dominant in the lower portion of the water column as measured in the present experiment.

Site 1 was observed to have atypical velocity profiles which may have significant consequences for sediment transport (Figure 3.30). Several of the tides measured, had an offshore-directed current throughout the entire duration of the tide over the

the measured profile length. This pattern of offshore currents, is likely associated with a larger scale circulation system in the Firth of Thames, created by winds in the region. In general, periods of higher wave activity correspond to north-westerly winds as the fetch is large in these cases. However, not all tides that had entirely offshore currents were associated with a north-westerly wind, these currents sometimes occurred when the wind was westerly or even slightly south-westerly (for example, tide 3 at site 1). The Firth of Thames has an open entrance and so it is possible that the field site was subjected to wave processes occurring in the Hauraki Gulf as the Firth is an embayment of the Hauraki Gulf, a semi-enclosed coastal sea, which is exposed to ocean waves (Figure 4.1) (Black *et al.*, 2000).

Figure 4.1: The Firth of Thames situated in the Hauraki Gulf, New Zealand. From Google Maps (2017)

Black *et al.* (2000) undertook 3D modelling of the Hauraki Gulf, including the Southern Firth of Thames and they concluded that interactions between the tides, winds and the morphology of the Hauraki Gulf are the main controls on the circulation patterns observed. Given the topography of the area, it is possible that waves may be refracting around headlands or islands. In modelling the Firth of Thames using a north-westerly oriented wind, Black *et al.* (2000) found that wind-driven currents can be in the opposite direction to the wind as they are deflected by topographical features such as islands. The authors also noted that depth-averaged currents can be directed up-wind in the central Firth of Thames, in response to an adverse wind-induced pressure gradient along the Firth (Figure 4.2). Therefore, it

is possible that similar processes are acting at the field site to cause a current that is opposite to the wind direction, (although the wind in the modelled scenario was forced at 15 m/s was a little stronger than the maximum wind recorded during the field experiment of approximately 12 m/s).

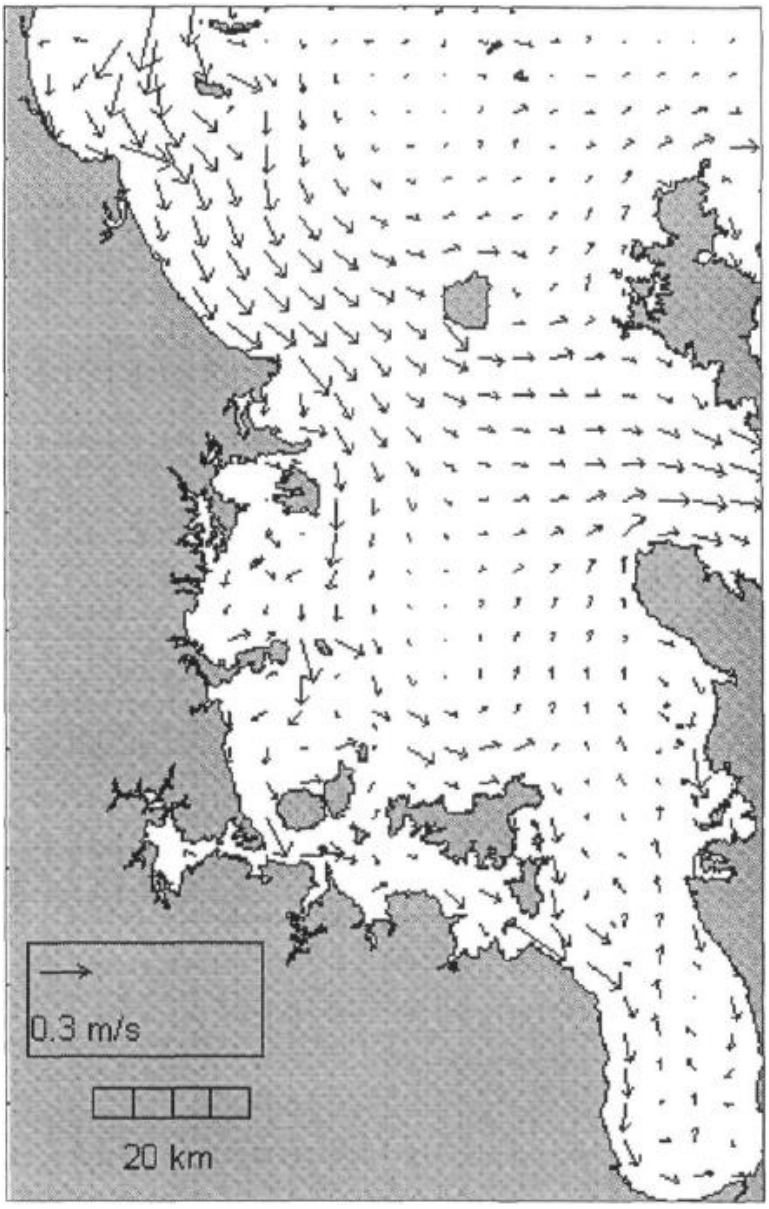

Figure 4.2: Model results for depth-averaged near steady state velocities from the Firth of Thames, New Zealand, for a north-west wind of 15 m/s. From Black *et al.* (2000).

Green *et al.* (1997) studied the interactions of currents and waves at different scales in the Manukau Harbour, New Zealand, to determine how these processes control estuarine sediment dynamics. They concluded that on the intertidal flat, waves control turbidity, and that changes in fetch and small variations in the strength of the wind caused changes in the height of waves over the tidal cycle. Ability of the orbital motions to reach the bed was controlled mainly by local water depth

associated with the variation of the tides, which is reflected in the u-shaped SSC pattern observed in the Firth of Thames. The breaker index is relatively large at site 1 compared to other sites, so orbital velocities can penetrate to the bed. The presence of vegetation at the bed may also reduce wave orbital motions at the other sites.

The ability of the waves to penetrate to the bed and the presence of offshore oriented currents at site 1 has significant implications for sediment transport. SSC (mg/l) was plotted against U_{sigbed} (m/s) (Figures 3.15-24) to determine if there was a correlation between the presence of waves and SSC values. During 'wavy' tides at site 1 (Figure 3.20), SSC is greatest on the flood tide and is associated with large significant orbital velocities at the bed. U_{sigbed} then diminishes towards high tide. SSC decreases an hour into the flood tide despite U_{sigbed} remaining high. Numerous variables including breaker ratio, water depth and wind direction were plotted against SSC (see appendix) to determine a possible cause for high U_{sigbed} with low SSC but no satisfactory answer was identified.

At site 1 during times with low wave energy (Figure 3.15), SSC is less than that observed during times of wave action. Sites 1 to 3 generally show a classical u-shape of SSC over the tidal cycle for both low wave energy and high wave energy tides (Figure 3.14), indicating larger shear stresses during periods of faster current velocities. From sites 4 to 5 the shape of the SSC plots changes from u-shaped to more n-shaped with a slight skew toward SSC being larger on the flood for most tides, which aligns with the tidal currents being flood dominant in the forest. SSC decreases toward site 5, especially during non-wavy tides. U_{sigbed} is highest at site 1 but the waves attenuate into the forest and so U_{sigbed} is very small at site 5 and the fact that SSC is highest near high tide when shear stresses are smaller indicates that advection into the forest is the primary mechanism for sediment transport into the back of the forest. Similar processes were observed by Bassoullet *et al.* (2000), in a study of sediment transport over the Brouage intertidal mudflat within the Baie de Marennes-Olerona (France). Bassoullet *et al.* (2000) took continuous measurements of turbidity, waves, tidal currents, changes in bed elevation, and additional sediment cores were collected to analyse sediment characteristics. Two conclusions were reached by this study, firstly that under wave-dominant conditions, resuspension due to waves could be significant. Secondly, that tidal

forcing controls the distribution of the sediment, particularly when spring tides occur in calm periods. Overall, the authors found wave conditions resulted in a net offshore movement of sediment, as is seen at site 1 in the Firth of Thames, whereas tidally dominant currents, caused a net onshore flux. When SSC is elevated during non-wavy conditions, for example the flooding tide at site 2 (Figure 3.16), either fast tidal currents are causing local erosion or sediment is being brought in from elsewhere. As the fastest tidal currents do not occur at times of low wave energy and high SSC, the latter is probably true.

The offshore wave-induced currents at site 1 result in a large net flux of sediment offshore (Figure 3.40). It is noted that although the ADCPs only measured the lower water column, OBS measurements indicated that above the height of the ADCP profile, SSC were small, so the estimated contributions to the flux from the upper part of the water column are likely to be much smaller or negligible. In total, approximately 850 kg/m was removed offshore over the duration of the experiment. All other sites had a net onshore flux of sediment with the largest onshore flux being from site 4 with 113.3 kg/m moving into the forest. These sediment fluxes at each site are summarised in a conceptual diagram (Figure 4.3).

If the sediment were removed locally, we would expect there to be areas of scour between sites 1 and 2 and between sites 3 and 4 with deposition everywhere else (Figure 4.3). There was some evidence for scour on the intertidal flat around site one in the form of runnels (Figure 4.4). Evidence of scour around pneumatophores is visible at site 2 in the fringe and just seaward of site 2 (Figure 4.5), which may also be contributing to the sediment flux measured at site 1. Further into the forest at sites 3, 4 and 5, despite denser pneumatophores, no obvious signs of scour is present (Figure 4.6). A study by Norris *et al.* (2017), in the Mekong Delta, Vietnam showed a similar pattern of scour at the fringe around pneumatophores and none in the mangrove forest. The authors suggest that elevated turbulence within the fringe may influence the scour around pneumatophores. In the situation described by Norris *et al.* (2017), highest dissipation rates are associated with the densest vegetation and largest wave energy at the fringe. The distribution of pneumatophores from the study by Norris *et al.* (2017), contrasts with the present results from the Firth of Thames where the pneumatophores are more densely packed in the forest than they are at the fringe (Figure 4.6). At the fringe region,

the interaction of the relatively fast flows (wave and tidal) with vegetation results in scour, whereas further into the forest, flows are less energetic and less turbulent (Mullarney *et al.*, 2017b) and there is minimal scour (Figure 4.3). If scour is occurring between sites 1 and 2, it would be expected that the bottom profile will steepen (see inset in Figure 4.3). Our observations are therefore consistent with the mechanisms explored by Bryan *et al.* (2017), who found that in muddy, vegetated intertidal environments with a dense forest fringe, as at the Firth of Thames, a convex profile develops. The development of a convex profile occurs when there is an elevation change where current velocities alter at the vegetation boundary (noting that in the Firth of Thames, peak horizontal flow velocities at site 1 are 0.0665 m/s, in contrast to 0.0110 m/s at site 2).

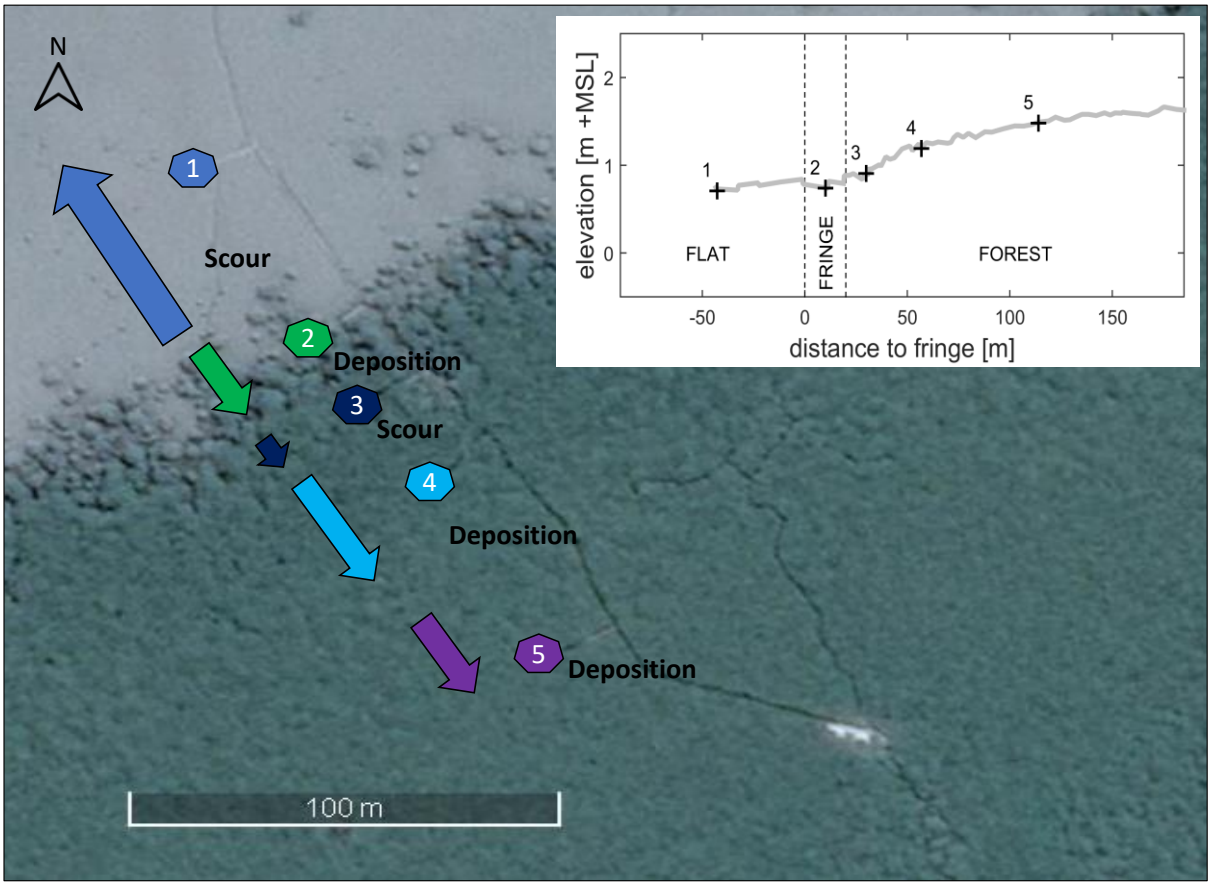

Figure 4.3: Conceptual diagram showing sediment fluxes in and out of the mangrove forest. Arrows indicate sediment direction and the size of the arrow is indicative of the comparative amount of sediment moving in or out at each site, although arrows are not to scale. Potential areas of scour and deposition are labelled. Inset - Mudflat and mangrove elevation (m + MSL). Elevation profile data provided by Dr Erik Horstman (University of Waikato).

The quantity of sediment that is moving offshore is substantial and it is possible that the drainage channels and pneumatophore scour in the vicinity of the fringe do

not supply all of this sediment. Alternatively, or in addition to local erosion, sediment may be being advected into the area near site 1 by E-W currents and then moved away by the waves. Swales *et al.* (2007) write that the prevailing wind from the southwest sets up an anticlockwise circulation in the Firth of Thames, whereas when winds are persistently from the north and east, there will be a clockwise circulation cell. During the experiment, the predominant wind direction was from the south-west and west (Figure 3.1a), which means that the larger-scale circulation was likely in an anti-clockwise direction, which may have advected sediment that that was discharged from the Waitakaruru River. Of the three rivers entering the Firth, the Waitakaruru is the smallest and probably provides the smallest sediment input. Therefore, when winds come from the north, it might be anticipated that the clockwise circulation combined with the sediment input from the two larger rivers east of the field site (the Waihou and the Piako rivers), could result in even more sediment transported to site 1. Haughey *et al.* (2017) speculated that there may be two opposing circulation systems in the Firth of Thames, one on the eastern side and another on the western side (controlled by the bathymetry). The model by Black *et al.* (2000) (Figure 4.2), is forced with a N-W wind, which results in currents travelling southward down the left and right edges of the Firth and being moved offshore up the centre of the Firth. Further work would be required to identify and confirm the presence of one or multiple circulation systems, which may be transporting sediment around the Firth, depending on the dominant wind direction.

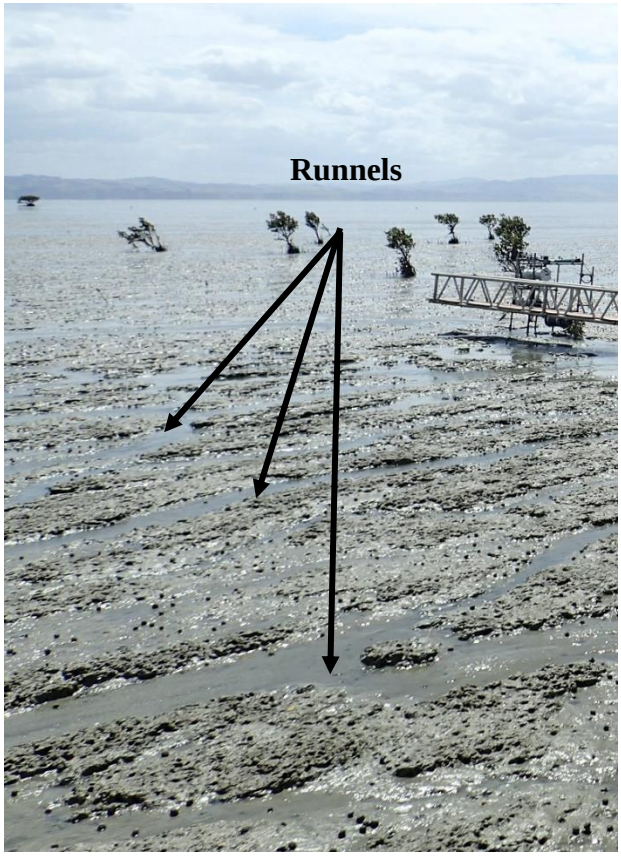

Figure 4.4: Photograph of runnels behind site 1, Firth of Thames, New Zealand

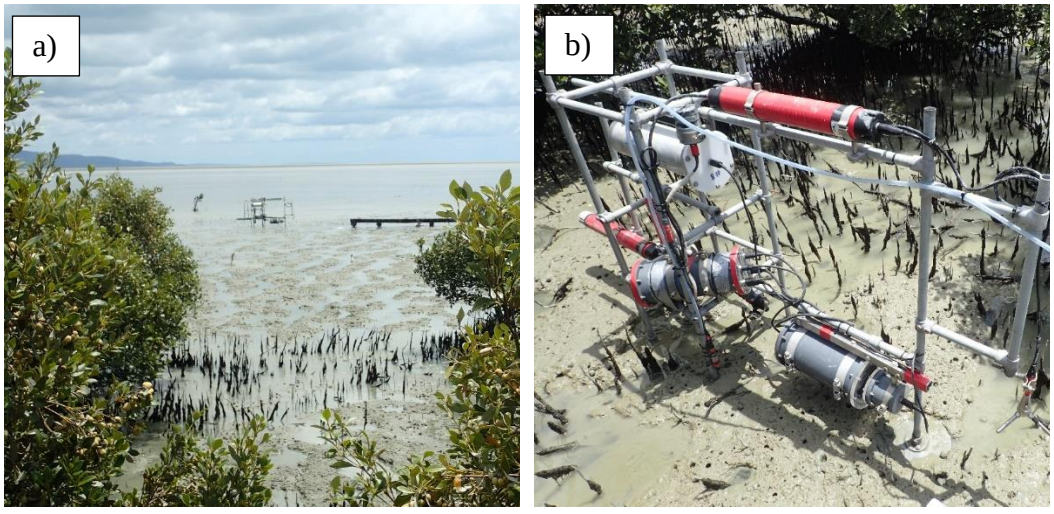

Figure 4.5: a) Scour around pneumatophores seaward of site 2 and b) Site 2 equipment deployment, showing scour around pneumatophores.

Figure 4.6: Site 3 instrument deployment, showing dense pneumatophores and no scour. Water in the photograph is in a runnel. Firth of Thames, New Zealand.

The Firth of Thames mudflat is accreting and the mangrove forest is advancing (Horstman *et al.*, 2017a; Swales *et al.*, 2007; Swales *et al.*, 2015). The fringe area is accreting by an average of 34 mm/yr^{-1} (Swales, 2015) and the forest has advanced noticeably just in the past decade (Figure 4.7). This accretion is at odds with the large offshore flux observed at site 1 in this study, which implies that there would be some scour between sites 1 on the intertidal flat, and site 2 at the beginning of the fringe (Figure 4.3). Alternatively, these results are not inconsistent with sediment being transported to site 1 via a circulation system and then being advected offshore by wave action. It is possible that in calm periods when waves are diminished and tidal currents are relatively more significant, that accretion is able to occur and that these tidal current dominant periods are more common than wave dominant ones. For the long-term wind-data, the wind blows from between the west and north, 31.7% of the time, during which average wind speeds were 4.3 m/s. During the experiment, winds from the same direction (NW), occurred 42.4% of the time with an average wind speed of 4.6 m/s. Despite the scour just offshore

of the forest, the results imply deposition just landward of the fringe region (Figure 4.3). These conclusions are in line with numerical modelling results from Bryan *et al.* (2017), who predicted slowing of N-S currents and deposition at the fringe of a mangrove forest in the Mekong Delta. The results also imply scour or advection between site 3 and 4 (Figure 4.3), as estimated sediment fluxes at site 4 (c.111.3 kg/m/6 days directed into the forest) were much larger than at site 3 (c.2.56 kg/m/6 days, also landward directed). Neither site 3 nor site 4 had large scour patches but there were runnels observed in both areas which may contribute to sediment transport. Sediment may be advected in from elsewhere in the forest because the current does not become entirely N-S oriented in the forest area.

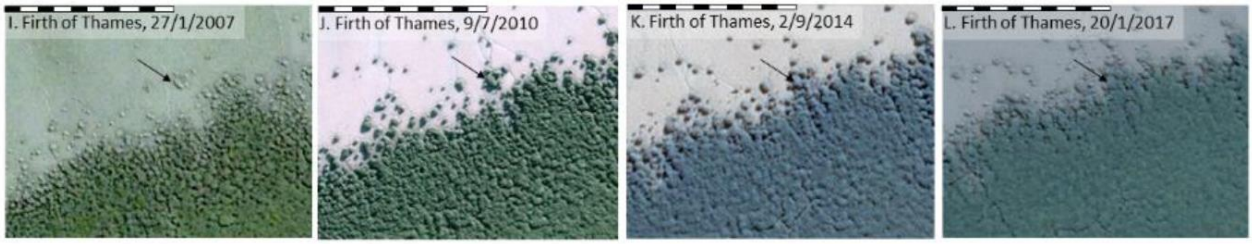

Figure 4.7: Advancement of the mangrove forest in the Firth of Thames, New Zealand from 2007-2017. Arrow indicates the same location and shows an advance in the forest area. The scale represents 100 m and north is upwards. From Horstman *et al.* (2017a).

Measured SSC values are large, particularly in the near bed region (Table 3.4), with the highest concentration observed being approximately 6 g/l. SSC values measured in the Firth of Thames are high in comparison to other mangrove forests, for example, a study of the mangroves at Cù Lao Dung, Vietnam by Fricke *et al.* (2017), showed a mean of 0.92 g/l during March 2015 and a maximum over all measurement periods of <2 g/l.

Flocculation affects particle size and density which in turn influences a particles settling velocities, which has a large influence on sediment transport, (Fennessy *et al.*, 1994). At the Firth of Thames site, there appeared to be both temporal and spatial differences in floc sizes based on preliminary qualitative data analysis. Patterns in floc size over two tides (9 and 11) were similar between tides which were characterised by similar (wave/tidal) conditions. However, floc sizes differed between sites (Figure 3.38 and 3.39). The largest flocs occurred on the mid-ebb tide which coincided with low SSC relative to other times in the tides. The

occurrence of larger flocs during the ebb tide when SSC are diminished, indicates that turbulent shear is at a level that promoted flocculation as opposed to disaggregation which occurs at high shear velocities (Fugate & Friedrichs, 2003). At high tide, the number of flocs at site 1 diminishes, possibly because turbulence is too low to cause the particle collisions, which promote floc formation (Fugate & Friedrichs, 2003) or the large flocs are settling out of suspension during these quiescent times. Additionally, a greater number of large-sized flocs were observed at site 1 than were observed at the same tides at site 3, possibly because increased turbulence caused by shear at the length scale of the vegetation causes the flocs at site 3 to disaggregate (Nepf, 2012), alternatively turbulence is not sufficient to cause collisions. Site 3 shows less variation in floc numbers and floc size than site 1, with floc numbers remaining relatively high throughout most of the tide. Differences in the sediment dynamics at sites 1 and 3 is also evident in Figure 3.14, which shows greater variability in SSC concentrations at site 1 during both tides in comparison to site 3, which remained fairly similar in terms of floc size and concentration throughout the tides (Figures 3.38-39).

4.1 Summary of findings

Mangroves offer many ecological and physical benefits to an area. Of particular relevance to issues surrounding our changing climate, is the physical role these forests play in helping to reduce wave energy as it interacts with the vegetation. There is some evidence, though mainly observational, that mangroves in Indonesia helped to protect the coastline, during the catastrophic tsunami on 26th December 2004 (Alongi, 2008). While in New Zealand, mangroves are advancing and developing, they are in decline in many other countries where they have been removed for reasons such as expanding aquaculture (Stokes *et al.*, 2016). Growing recognition of the importance of mangrove habitats both biologically and physically has led to the desire to restore mangroves, primarily for coastal protection (Spalding *et al.*, 2014). This drive to restore the mangrove forests in the world is in contrast to the situation in New Zealand, with removal of forests being a primary management strategy (Horstman *et al.*, 2017a). However, it is necessary to understand the hydrodynamics and sediment inputs and transport pathways into an area before any removal takes place, as management should be site specific (Stokes

& Harris, 2015). This thesis has aimed to contribute to the body of knowledge on hydrodynamics and sediment transport in the Firth of Thames mangroves.
The major findings of the thesis are:

1. The hydrodynamic conditions at the experimental location are significantly influenced by wind. Winds set up circulation patterns in the Firth of Thames, which are variable depending on the wind direction and speed and interactions with the local topography.
2. Contrary to the proposed hypothesis that there would be continuous flux of sediment into the mangrove forest, the results presented here show that the picture is a little more complicated. At site 1 over the 6-day period there was a net sediment flux of 850 kg/m in the offshore direction, which is away from the forest. At the remaining sites, there is a net sediment flux of 201 kg/m in total (all sites combined) in the onshore direction.
3. Point 2 is at odds with other studies which suggests that the mangrove system is accreting. From this it is hypothesised that during periods of reduced wave energy conditions, the net flux of sediment is onshore and these calmer periods occur often enough that accretion dominates over erosion.
4. Flow rotation appears to occur in the mangrove forest, becoming orientated toward perpendicular to the shoreline in the forest, as opposed to a dominant E-W orientation on the mudflat.
5. Minimal scour is observed near site 1 on the mudflats. From this it is hypothesised that sediment is being advected into the area of site 1 by the E-W component of the currents and strong wave activity removes it offshore. The circulation system set-up by the winds, is probably the mechanism of transporting sediment into the region. The main sediment sources are the Waihou and Piako Rivers or the smaller Waitakaruru River, depending on the direction of circulation, clockwise or anti-clockwise.
6. SSC was hypothesised to decrease into the forest. SSC decreases between sites 1 on the mudflat and site 2 at the fringe. Levels within the forest are similar at each site with a slight decrease towards site 5.
7. Near-bed SSC were much greater than at the upper measurement height (~20 cm above the bed).

8. The final hypothesis was that flocculation would increase in the fringe area before decreasing further into the forest. It was not possible to determine from the data collected, whether flocculation increased at the fringe, but larger flocs were less apparent further into the forest at site 3 then they were at site 1. The presence of many smaller flocs at site 3 does indicate that flocculation processes were still occurring in the forest and will have consequences for settling velocities.

4.2 Further work

Questions were raised during the analysis of the data that could not be answered without further research. Qualitative analysis of floc images gave some preliminary insight into the distribution of flocs and floc sizes; however, further quantitative analysis is required to provide floc size distributions. These distributions could be compared with other hydrodynamic variables such as turbulence intensity. This work is currently underway and may shed light on the controls on the flocculation processes. A more comprehensive array in the E-W direction may shed further light on the advective processes in the fringe region, in particular under different large-scale circulation patterns which arise from variable wind speeds and directions. Additionally, it would be valuable to extend the array/measurement locations further in the offshore direction to determine the eventual fate of the sediment transported offshore from site 1. As the water depths increase and the effect of waves becomes less important near the bed, it is reasonable to assume that this sediment is deposited further offshore. Continuous bed-level monitoring along with hydrodynamic data collection along the transect from the mudflat into mangrove forest, would provide long-term information on how the bed is responding to different conditions. Investigating flow rotation further will give more detailed information on how sediment is being transported between the mudflat and forest and how sediment is moving parallel to the shoreline. Two points of measurement were taken to obtain SSC. Near-bed SSC were much greater than at the upper measurement height (~20 cm above the bed). Typically, SSC is measured at just one point, which may result in inaccurate sediment flux calculations. Increased vertical resolution in both SSC and currents might help better resolve sediment fluxes in the future.

References

Alongi, D. M. (2008). Mangrove forests: Resilience, protection from tsunamis, and responses to global climate change. *Estuarine, Coastal and Shelf Science, 76*(1), 1-13. https://doi.org/10.1016/j.ecss.2007.08.024.

Balke, T., Bouma, T., Herman, P., Horstman, E., Sudtongkong, C., & Webb, E. (2013). Cross-shore gradients of physical disturbance in mangroves: implications for seedling establishment. *Biogeosciences, 10*(8), 5411-5419. https://doi.org/10.5194/bg-10-5411-2013.

Bassoullet, P., Le Hir, P., Gouleau, D., & Robert, S. (2000). Sediment transport over an intertidal mudflat: Field investigations and estimation of fluxes within the Baie de Marennes-Oleron; (France). *Continental Shelf Research, 20*(12-13), 1635-1653. https://doi.org/10.1016/S0278-4343(00)00041-8.

Black, K. P., Bell, R. G., Oldman, J. W., Carter, G. S., & Hume, T. M. (2000). Features of 3-dimensional barotropic and baroclinic circulation in the Hauraki Gulf, New Zealand. *New Zealand Journal of Marine and Freshwater Research, 34*(1), 1-28. http://dx.doi.org/10.1080/00288330.2000.9516912.

Bryan, K. R., Nardin, W., Mullarney, J. C., & Fagherazzi, S. (2017). The role of cross-shore tidal dynamics in controlling intertidal sediment exchange in mangroves in Cù Lao Dung, Vietnam. *Continental Shelf Research*, https://doi.org/10.1016/j.csr.2017.06.014.

Dyer, K. R., & Manning, A. J. (1999). Observation of the size, settling velocity and effective density of flocs, and their fractal dimensions. *Journal of Sea Research, 41*(1–2), 87-95. https://doi.org/10.1016/S1385-1101(98)00036-7.

Eisma, D. (1986). Flocculation and de-flocculation of suspended matter in estuaries. *Netherlands Journal of Sea Research, 20*(2), 183-199. https://doi.org/10.1016/0077-7579(86)90041-4.

Feller, I. C., Lovelock, C. E., Berger, U., McKee, K. L., Joye, S. B., & Ball, M. C. (2010). Biocomplexity in Mangrove Ecosystems. *Annual Review of Marine Science, 2*, 395-417. https://doi.org/10.1146/annurev.marine.010908.163809.

Fennessy, M. J., Dyer, K. R., & Huntley, D. A. (1994). Size and settling velocity distributions of flocs in the Tamar estuary during a tidal cycle. *Netherland Journal of Aquatic Ecology, 28*(3-4), 275-282. https://doi.org/10.1007/BF02334195.

Fricke, A. T., Nittrouer, C. A., Ogston, A. S., & Vo-Luong, H. P. (2017). Asymmetric progradation of a coastal mangrove forest controlled by combined fluvial and marine influence, Cù Lao Dung, Vietnam. *in press in Continental Shelf Research*. https://doi.org/10.1016/j.csr.2017.07.012.

Fugate, D. C., & Friedrichs, C. T. (2003). Controls on suspended aggregate size in partially mixed estuaries. *Estuarine, Coastal and Shelf Science, 58*(2), 389-404. https://doi.org/10.1016/S0272-7714(03)00107-0.

Furukawa, K., & Wolanski, E. (1996). Sedimentation in Mangrove Forests. *Mangroves and Salt Marshes, 1*(1), 3-10. https://doi.org/10.1023/A:1025973426404.

Furukawa, K., Wolanski, E., & Mueller, H. (1997). Currents and Sediment Transport in Mangrove Forests. *Estuarine, Coastal and Shelf Science, 44*(3), 301-310. https://doi.org/10.1006/ecss.1996.0120.

Gilbert, F., Aller, R. C., & Hulth, S. (2003). The influence of macrofaunal burrow spacing and diffusive scaling on sedimentary nitrification and denitrification: An experimental simulation and model approach. *Journal of Marine Research, 61*(1), 101-125. https://doi.org/10.1357/002224003321586426.

Green, M. O., Black, K. P., & Amos, C. L. (1997). Control of estuarine sediment dynamics by interactions between currents and waves at several scales. *Marine Geology, 144*(1), 97-116. https://doi.org/10.1016/S0025-3227(97)00065-0.

Green, M. O., & Coco, G. (2007). Sediment transport on an estuarine intertidal flat: Measurements and conceptual model of waves, rainfall and exchanges with a tidal creek. *Estuarine, Coastal and Shelf Science, 72*(4), 553-569. https://doi.org/10.1016/j.ecss.2006.11.006.

Harty, C. (2009). Mangrove planning and management in New Zealand and South East Australia: A reflection on approaches. *Ocean and Coastal Management, 52*(5), 278-286. https://doi.org/10.1016/j.ocecoaman.2009.03.001.

Haughey, R. R., Bryan, K., & Horstman, E. (Compiler) (2017). *Modelling the hydrodynamics within the mangrove tidal flats in the Firth of Thames*, thesis, University of Waikato.

Horstman, E. M., Dohmen-Janssen, C. M., Bouma, T. J., & Hulscher, S. J. M. H. (2015). Tidal-scale flow routing and sedimentation in mangrove forests: Combining field data and numerical modelling. *Geomorphology, 228*, 244-262. https://doi.org/10.1016/j.geomorph.2014.08.011.

Horstman, E. M., Dohmen-Janssen, C. M., & Hulscher, S. J. M. H. (2013). Flow routing in mangrove forests: A field study in Trang province, Thailand. *Continental Shelf Research, 71*, 52-67. https://doi.org/10.1016/j.csr.2013.10.002.

Horstman, E. M., Dohmen-Janssen, C. M., Narra, P. M. F., van Den Berg, N. J. F., Siemerink, M., & Hulscher, S. J. M. H. (2014). Wave attenuation in mangroves: A quantitative approach to field observations. *Coastal Engineering, 94*, 47-62. https://doi.org/10.1016/j.coastaleng.2014.08.005.

Horstman, E. M., Lundquist, C. J., Bryan, K. R., Bulmer, R. H., Mullarney, J. C., & Stokes, D. J. (2017a). The dynamics of expanding mangroves in New Zealand. In C. Makowski & C. W. Finkl (Eds.), *Threats to Mangrove Forests: Hazards, Vulnerability, and Management.* Springer International Publishing AG, in press.

Horstman, E. M., Mullarney, J. C., Bryan, K. R., & Sandwell, D. R. (2017b). *Deposition gradients across mangrove fringes*. Presented at the Coastal Dynamics 2017.

Hunt, S., Bryan, K. R., Mullarney, J. C., & Pritchard, M. (2016). Observations of asymmetry in contrasting wave and tidally dominated environments within a mesotidal basin: implications for estuarine morphological evolution. *Earth Surface Processes and Landforms, 41*(15), 2207-2222. https://doi.org/10.1002/esp.3985.

Kathiresan, K., & Bingham, B. L. (2001). Biology of mangroves and mangrove Ecosystems. *Advances in Marine Biology, 40*, 81-251. http://dx.doi.org/10.1016/S0065-2881(01)40003-4.

Lovelock, C., Feller, I., Ellis, J., Schwarz, A., Hancock, N., Nichols, P., & Sorrell, B. (2007). Mangrove growth in New Zealand estuaries: the role of nutrient enrichment at sites with contrasting rates of sedimentation. *Oecologia, 153*(3), 633-641. http://dx.doi.org/10.1007/s00442-007-0750-y.

MacDonald, I. T. (2009). *Flocculation of Fine Sediment in Turbulent Flows.* thesis, University of Auckland.

Mazda, Y., Wolanski, E., King, B., Sase, A., Ohtsuka, D., & Magi, M. (1995). Drag force due to the vegetation in mangrove swamps. *Mangroves and Salt Marshes, 1*, 193-199. https://doi.org/10.1023/A:1009949411068.

Morrisey, D. J. (2007). *The New Zealand mangrove: review of the current state of knowledge*. Auckland, N.Z. : Auckland Regional Council.

Morrison, M. A., Lowe, M. L., Parsons, D. M., Usmar, N. R., & McLeod, I. M. (Compiler) (2009). *A review of land-based effects on coastal fisheries and supporting biodiversity in New Zealand*.

Mullarney, J. C., & Henderson, S. M. (2017a). Flows Within Marine Vegetation Canopies. In p. in, V. Panchang & J. Kaihatu (Eds.), *Advances in Coastal Hydraulics*. World Scientific Publishing Ltd.

Mullarney, J. C., Henderson, S. M., Reyns, J. A. H., Norris, B. K., & Bryan, K. R. (2017b). Spatially varying drag within a wave-exposed mangrove forest and on the adjacent tidal flat. *in press in Continental Shelf Research*, https://doi.org/10.1016/j.csr.2017.06.19.

Nepf, H. M. (2012). Flow and Transport in Regions with Aquatic Vegetation. *Annual Review of Fluid Mechanics, 44*(1), 123-142. https://doi.org/10.1146/annurev-fluid-120710-101048.

Nepf, H. M., & Vivoni, E. R. (2000). Flow structure in depth-limited, vegetated flow. *Journal of Geophysical Research: Oceans, 105*(C12), 28547-28557. https://doi.org/10.1029/2000JC900145.

Norris, B. K., Mullarney, J. C., Bryan, K. R., & Henderson, S. M. (2017). The effect of pneumatophore density on turbulence: A field study in a Sonneratia-dominated mangrove forest, Vietnam. *in press in Continental Shelf Research*. https://doi.org/10.1016/j.csr.2017.06.002.

Reef, R., Feller, I. C., & Lovelock, C. E. (2010). Nutrition of mangroves. *Tree Physiology, 30*(9), 1148-1160. https://doi.org/10.1093/treephys/tpq048.

Rodil, I. F., Lohrer, A. M., Chiaroni, L. D., Hewitt, J. E., & Thrush, S. F. (2011). Disturbance of sandflats by thin terrigenous sediment deposits: consequences for primary production and nutrient cycling. *Ecological Applications, 21*(2), 416-426. https://doi.org/10.1890/09-1845.1.

Spalding, M. D., Ruffo, S., Lacambra, C., Meliane, I., Hale, L. Z., Shepard, C. C., & Beck, M. W. (2014). The role of ecosystems in coastal protection: Adapting to climate change and coastal hazards. *Ocean and Coastal Management, 90*, 50-57. https://doi.org/10.1016/j.ocecoaman.2013.09.007.

Stokes, D., Healy, T., & Cooke, P. (2010). Expansion Dynamics of Monospecific, Temperate Mangroves and Sedimentation in Two Embayments of a Barrier-Enclosed Lagoon, Tauranga Harbour, New Zealand. *Journal of Coastal Research, 26*(1), 113-122. https://doi.org/10.2112/08-1043.1.

Stokes, D. J., Bulmer, R. H., & Lundquist, C. J. (2016). Addressing the mismatch between restoration objectives and monitoring needs to support mangrove management. *Ocean and Coastal Management, 134*, 69-78. https://doi.org/10.1016/j.ocecoaman.2016.09.024.

Stokes, D. J., & Harris, R. J. (2015). Sediment properties and surface erodibility following a large-scale mangrove (Avicennia marina) removal. *Continental Shelf Research, 107*, 1-10. https://doi.org/10.1016/j.csr.2015.07.011.

Struve, J., Falconer, R. A., & Wu, Y. (2003). Influence of model mangrove trees on the hydrodynamics in a flume. *Estuarine, Coastal and Shelf Science, 58*(1), 163-171. https://doi.org/10.1016/S0272-7714(03)00072-6.

Swales, A., Bell, R. G., Ovenden, R., Hart, C., Horrocks, M., Hermanspahn, N., & Smith, R. K. (2007). *Mangrove-habitat expansion in the southern Firth of Thames: sedimentation processes and coastal-hazards mitigation*. Hamilton [N.Z.]: Environment Waikato.

Swales, A., Bentley, S. J., & Lovelock, C. E. (2015). Mangrove‐forest evolution in a sediment‐rich estuarine system: opportunists or agents of geomorphic change? *Earth Surface Processes and Landforms, 40*(12), 1672-1687. https://doi.org/10.1002/esp.3759.

Tang, M., & Kristensen, E. (2007). Impact of microphytobenthos and macroinfauna on temporal variation of benthic metabolism in shallow coastal sediments. *Journal of Experimental Marine Biology and Ecology, 349*(1), 99-112. https://doi.org/10.1016/j.jembe.2007.05.011.

Temmerman, S., Bouma, T. J., Govers, G., Wang, Z. B., De Vries, M. B., & Herman, P. M. J. (2005). Impact of vegetation on flow routing and sedimentation patterns: Three-dimensional modeling for a tidal marsh. *Journal of Geophysical Research-Earth Surface, 110*(F4), 1-18 . https://doi.org/10.1029/2005jf000301.

Thrush, S. F., Hewitt, J. E., Cummings, V. J., Ellis, J. I., Hatton, C., Lohrer, A., & Norkko, A. (2004). Muddy Waters: Elevating Sediment Input to Coastal and Estuarine Habitats. *Frontiers in Ecology and the Environment, 2*(6), 299-306. https://doi.org/10.1890/1540-9295(2004)002[0299:MWESIT]2.0.CO;2.

Victor, S., Golbuu, Y., Wolanski, E., & Richmond, R. (2004). Fine sediment trapping in two mangrove-fringed estuaries exposed to contrasting land-use intensity, Palau, Micronesia. *Wetlands Ecology and Management, 12*(4), 277-283. https://doi.org/10.1007/s11273-005-8319-1.

Vo-Luong, P., & Massel, S. (2008). Energy dissipation in non-uniform mangrove forests of arbitrary depth. *Journal of Marine Systems, 74*(1), 603-622. https://doi.org/10.1016/j.jmarsys.2008.05.004.

Wolanski, E. (1995). Transport of sediment in mangrove swamps. *Hydrobiologia, 295*(1), 31-42. https://doi.org/10.1007/bf00029108.

Woodin, S. A., Wethey, D. S., Hewitt, J. E., & Thrush, S. F. (2012). Small scale terrestrial clay deposits on intertidal sandflats: Behavioral changes and productivity reduction. *Journal of Experimental Marine Biology and Ecology, 413*, 184-191. https://doi.org/10.1016/j.jembe.2011.12.010.

Wu, Y., Falconer, R. A., & Struve, J. (2001). Mathematical modelling of tidal currents in mangrove forests. *Environmental Modelling & Software, 16*(1), 19-29. http://dx.doi.org/10.1016/S1364-8152(00)00059-1.

Yang, J., Gao, J., Cheung, A., Liu, B., Schwendenmann, L., & Costello, M. J. (2013). Vegetation and sediment characteristics in an expanding mangrove forest in New Zealand. *Estuarine, Coastal and Shelf Science, 134*, 11-18. http://dx.doi.org/10.1016/j.ecss.2013.09.017.

Appendix

SSC plotted against other variables

SSC from Site 1 (under wavy conditions) was plotted against several variables to try and determine why SSC diminishes but u_{sigbed} remains high (Figures A1-A4).

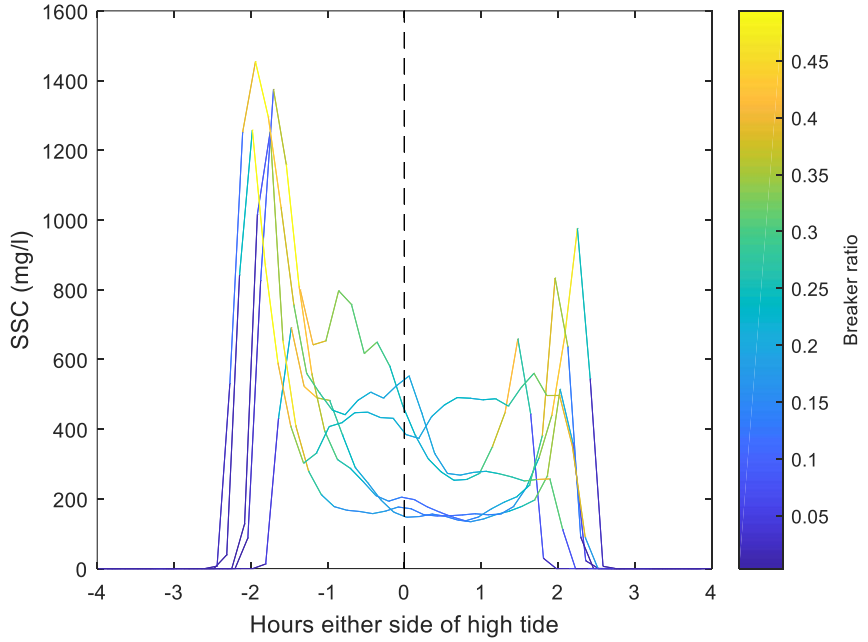

Figure A.1: SSC (~30 cm above the bed) over days with greater wave energy (mean *Hs* = 0.1139 m at site 1 for tides 1 and 3-8 and 12). Lines are coloured by the breaker ratio.

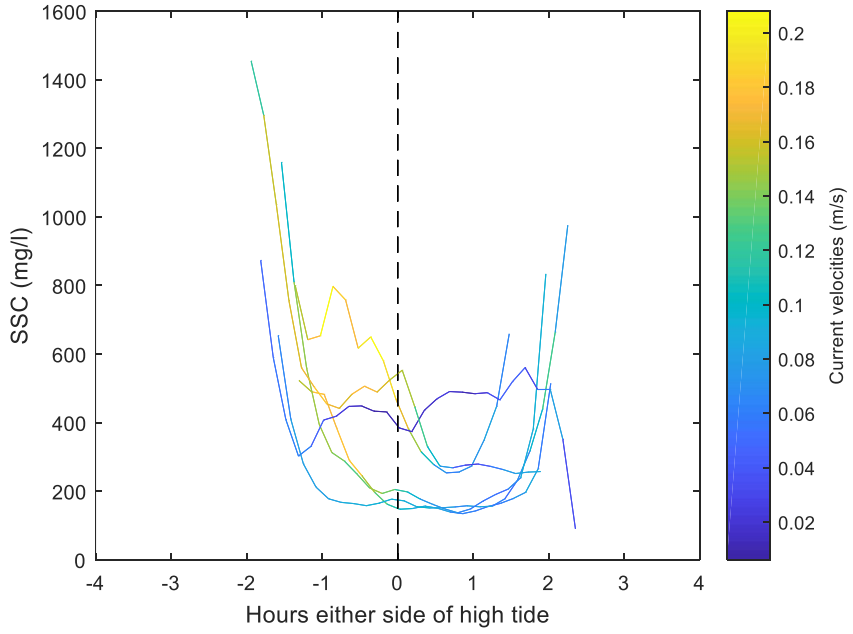

Figure A.2: SSC (~30 cm above the bed) over days with greater wave energy (mean *Hs* = 0.1139 m at site 1 for tides 1 and 3-8 and 12). Lines are coloured by current velocities (m/s).

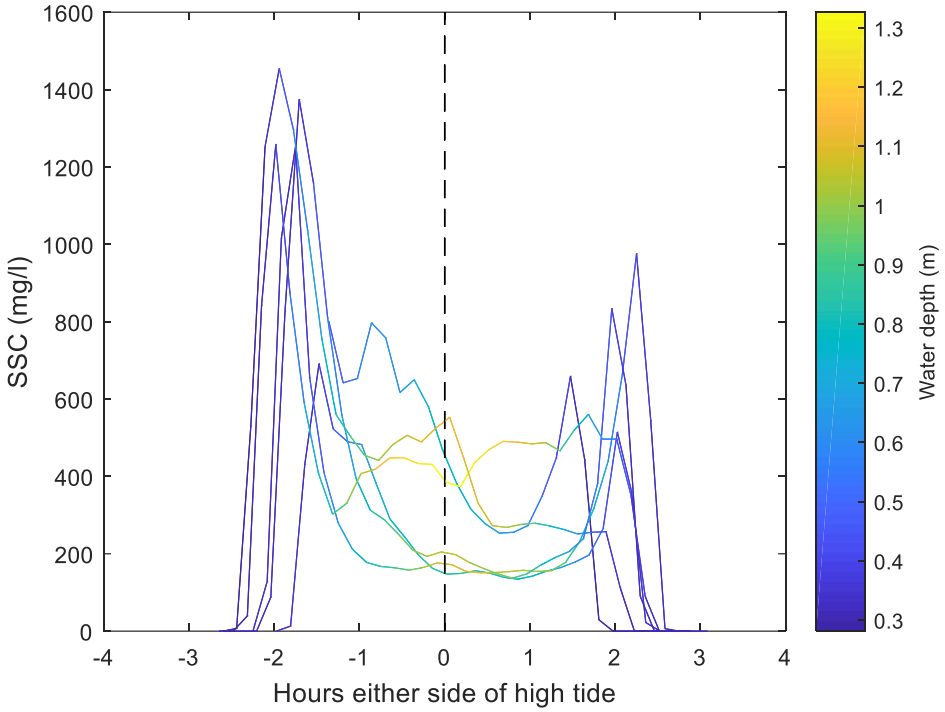

Figure A.3: SSC (~30 cm above the bed) over days with greater wave energy (mean *Hs* = 0.1139 m at site 1 for tides 1 and 3-8 and 12). Lines are coloured by Water depth (m).

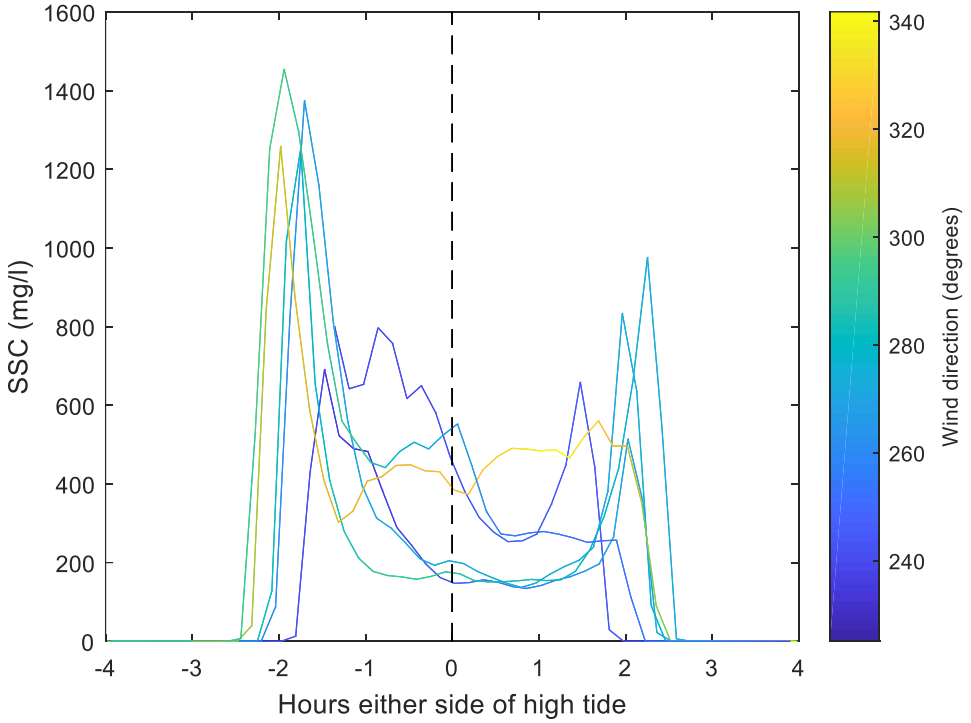

Figure A.4: SSC (~30 cm above the bed) over days with greater wave energy (mean *Hs* = 0.1139 m at site 1 for tides 1 and 3-8 and 12). Lines are coloured by wind direction (degrees).